INSBN ALLOYAND INSB NANOWIRE GROWN BY METAL-ORGANIC CHEMICAL VAPOR DEPOSITION

JIN YUNJIANG

SCHOOL OF ELECTRICAL & ELECTRONICS ENGINEERING

2014

INSBN ALLOYAND INSB NANOWIRE GROWN BY METAL-ORGANIC CHEMICAL VAPOR DEPOSITION

JIN YUNJIANG

SCHOOL OF ELECTRICAL & ELECTRONICS ENGINEERING

A THESIS SUBMITTED TO THE NANYANG TECHNOLOGICAL UNIVERISTY IN FULFILLMENT OF THE REQUIREMENT FOR THE DEGREE OF DOCTOR PHILOSOPHY

2014

STATEMENT OF ORIGNALITY

I hereby certify that the content of this thesis is the result of work done by me and has not been submitted for a higher degree to any other University of Institution.

1 May 2014

Signature of candidate

Date

ACKNOWLEDGEMENTS

First and foremost, I would like to express my deep gratitude to my supervisor, Associate Professor Zhang Daohua, for offering me the opportunity to pursue my higher degree in this interesting filed. I deeply appreciate all his constant supervision, encouragement and support throughout the course of this research work. He has been paying great effort to teach me all along and enlighten me with sparkling research idea, whenever it was during group meetings, or manuscript reviewing. His insight and timely suggestion in this project helped me greatly during the research. His kindness, gentleness, and conscientious attitude make him not only a good learning example of mine in research but also in life.

I would like to express deep appreciation to my second supervisor, Associate Professor Tang Xiaohong, for his guidance, invaluable advice and helpful discussion during my work. His vision, depth and breadth of knowledge in research inspired me to explore the world. Actually, this project would never be completed without his support and help.

With attachment to the Institute of Material and Research and Engineering, I also was quite fortunate to have Dr. Teng Jinghua as my cosupervisor. Each time to IMRE, I always could get valuable comments and advice from Dr.Teng, and he also has provided much help for some important measurement and characterization made in IMRE.

Many thanks are expressed to Prof. Li Jinhua, Prof. Zhang baolin, Dr. Yin Zhongyou, Ms. Chen Xizi, Ms. Wang Yan, for their much help in experimental measurements and valuable discussion in my research work.

Many thanks to Dr. Yan Changchun, Dr. Zhang Xuejin, Mr. Li Dongdong, Mr. Xu Zhengji, Dr. Ke Chang, Dr. Bian Haijiao, Mr. Wang ye, Mr. Wang Yueke, Ms. Wang Jun, Mr. Li Yicen, and it is them who make my life in Nanophotonics lab so meaningful and joyful.

I would also thank all the lab technicians in Characterization lab, Photonics lab, Nanophotonics lab and Nanofabrication lab. Special thanks are due for Mr. Fauzi, Ms. Seet, Ms. Porche, Ms. Dabby, Mr. Chia who have provided much help and convenience in my work.

I would like to express my gratitude to my parents, for raising me up, giving me their unconditional love and all the best things. I also thank my wife Ms. Peng liping for her love and support. She is the reason for my burning desire to finish my Ph.D.

TABLE OF CONTENTS

ACKNOWLEDGEMENTS i

ABSTRACT vi

LIST OF FIGURE vii

LIST OF TABLES xv

CHAPTER 1. INTRODUCTION 1

1.1 Motivation 1

1.2 Objectives 6

1.3 Major contributions 8

1.4 Organization of this report 9

CHAPTER 2. BACKGROUND 11

2.1 III-V semiconductor materials 11

2.2 Physical properties of InSb 14

2.3 Utilization of InSb in infrared area 15

2.3.1 InSb for middle wavelength infrared region 15

2.3.2 Materials for long wavelength infrared region 17

2.3.3 InSbN for long wavelength application 21

2.4 Basics for one dimensional InSb 24

2.4.1 Nanoscience and nanotechnology 24

2.4.2 Nanowire growth mechanism and techniques 25

2.4.3 Physics for nanowire growth 30

2.4.4 Preparation of InSb nanowires 32

2.4.5 Properties and application of InSb nanowire 37

2.5 Experimental setup and methods 43

2.5.1 Metal-organic chemical vapor deposition 43

2.5.2 Characterization methods 45

CHAPTER 3. EPITAXIAL GROWTH OF HIGH QUALITY INSB AND $INSB_{1-x}N_x$ ALLOYS BY MOCVD 49

3.1 Introduction....49

3.2 InSb epilayers on InSb substrate....49

3.2.1 Experiment....49

3.2.2 Characterization....52

3.2.3 Antisite defect Sb_{In}....59

3.3 $InSb_{1-x}N_x$ alloys on InSb substrate....62

3.3.1 Growth details....63

3.3.2 Characterizations and measurements....64

3.3.3 Behavior of nitrogen in the epilayers....70

3.4 Summary....74

CHAPTER 4. $INSB_{1-x}N_x$ ALLOYS on GAAS AND GASB SUBSTRATES....76

4.1 Introduction....76

4.2 InSbN alloys on GaAs substrate....77

4.2.1 Growth and annealing treatment....77

4.2.2 Optical property....78

4.3 InSbN alloys on GaSb substrate....83

4.4 Summary....90

CHAPTER 5.GROWTH AND CHARACTERIZATION OF INSB NANOWIRES ON INSB SUBSTRATE....91

5.1 InSb nanowires on InSb (100)....91

5.2 InSb nanowires on InSb (111) B....97

5.2.1 Growth and characterization....98

5.2.2 Growth mechanism....103

5.3 Self-nucleation of InSb nanowires....107

5.3.1 Based on indium droplet....107

5.3.2 Based on antimony droplet....113

5.4 Summary....118

CHAPTER 6. GROWTH OF INSB NANOWIRES ON GAAS AND SI SUBSTRATES 120
6.1 InSb nanowires on GaAs (111) B 120
6.1.1 Growth and characterization 120
6.1.2 Mechanism and discussion 125
6.2 InSb nanowires on Si 128
6.2.1 Growth and characterization 128
6.2.2 Mechanism 129
6.3 Summary 135
CHAPTER. 7 CONCLUSIONS 137
7. 1 Conclusions 137
7. 2 Recommendations 139
AUTHOR’S PUBLICATIONS 141
BIBLIOGRAPHY 143

ABSTRACT

InSb is a very special binary III-V semiconductor with important applications in infrared detectors, optoelectronics and magnetic field sensors. Attracted by the promising applications for long wavelength infrared range by incorporating a small amount of nitrogen, InSbN alloys were grown by Metal-organic chemical vapor deposition (MOCVD) and characterized with various techniques.

The first part of this project deals with growth and characterization of the $InSb_{1-x}N_x$ alloys, aiming to reduce the band gap of the alloy. InSb epitaxial layers on InSb substrate were firstly prepared by MOCVD and then the InSbN alloys. Their structural, electrical and optical properties were characterized. It is demonstrated that InSbN alloys can be prepared by MOCVD technique and the concentration of nitrogen in the alloys varies with the growth conditions, including growth temperature and N/(N+Sb) ratio. The effect of GaAs and GaSb substrates on InSbN alloys has also been investigated. The N incorporation, band gap reduction and N distribution of InSbN alloys on the two substrates have been studied carefully.

The second part primarily focuses on the growth and characterization of InSb naowires. InSb nanowires were grown on both (100) and (111) InSb substrates under different conditions. Uniform vertical nanowires with high density were obtained on InSb (111) substrate and the growth mechanism was investigated. In addition, despite the large lattice mismatch, InSb nanowires were also successfully realized on GaAs and Si substrates and the growth mechanism was also discussed in detail.

LIST OF FIGURE

Figure 1.1 Two transmission window in atmosphere, one is mid wavelength infrared (MWIR) between 3-5 μm, the other is far wavelength infrared (FWIR) between 8-14 μm.

Figure 2.1 III-V development milestones.

Figure 2.2 Wireless frequency spectrum showing RF semiconductor technologies and applications.

Figure 2.3 Spectral detectivity of InSb detector.

Figure 2.4 Optical band gap of $InSb_{1-x}Bi_x$ as a function of composition.

Figure 2.5 The dependence of energy band gap of $InAs_xSb_{1-x}$ on the composition.

Figure 2.6 The Lattice constant, energy gaps for certain ternaries such as InAsN, GaAsN, InPN, etc.

Figure 2.7 The E_C and E_V band edges and N level of $InSb_{1-x}N_x$ at 300 K as a function of x.

Figure 2.8 Diagram of the process of the VLS mechanism.

Figure 2.9 Phase diagram of Au-Si alloy.

Figure 2. 10 Schematic diagram of the LIL-patterning and CBE process.

Figure 2.11 SEM micrographs of ordered InSb nanowire arrays grown on InAs (111) B with at 360 °C. Inset picture shows top view images of the corresponding sample.

Figure 2.12 SEM image of InSb nanowires prepared by AAM.

Figure 2.13 SEM of a bundle of aligned nanowires released from AAM with 200nm pores, (b) SEM of a bundle of nanowires after they are removed from the template with 30 nm pores.

Figure 2.14 SEM illustrations of InAs/InSb (a), InP/InSb (b) and GaAs/InSb (c) nanowires.

Figure 2.15 Relation of the diameters of InSb nanowire with the bandgap.

Figure 2.16 The temperature dependence of the thermoelectric power (a) and the differential conductance (b) of a bundle of InSb nanowires.

Figure 2.17 Typical set of electric currents vs. magnetic field curves measured at different voltages.

Figure 2.18 Rashba coefficients of InSb nanowires as functions of external electric field of at fixed radius of 8 nm (a) and 24 nm (b), respectively.

Figure 2.19 (a) The schematic diagram of MOCVD system and (b) the photograph of the system under the growth process.

Figure 2.20 Schematic diagram of the growth process in the MOCVD reactor.

Figure 2.21 Schematic diagram of the PL system.

Figure 3.1 AFM images of the sample S1, S2 and S3.

Figure 3.2 XRD spectra of samples: S1, S2, S3, InSb substrate. InSb substrate was measured for comparison.

Figure 3.3 PL spectrum of InSb substrate at various temperatures. The peak positions shifts to longer wavelength with increasing temperature as indicated by the black allows. (b) The fitting curve by Vanshni equation.

Figure 3.4 PL spectra of samples S1, S2 and S3 measured at 10 K.

Figure 3.5 (a), (b), (c) indicate the PL spectra of S1, S2 and S3 measured at various temperatures, respectively. The main emission peak has a blue shift first and then a red shift with enhancing the temperature as indicated by the arrows. (d) Summarized band energy values from 10 to 300 K of the samples.

Figure 3.6 Temperature dependence of mobility (a) and surface carrier concentration (b) the data of InSb substrate was included as reference.

Figure 3.7 Formation energy of the native point defects in bulk InSb as a function of the Fermi level under In rich and Sb rich conditions.

Figure 3.8 PL spectra of the samples dependent on V/III ratio at 490 ^{o}C, measured at 10 K.

Figure 3.9 SEM photographs of (a) R1160, (b) R1166, (c) R1176 and (d) R1178 surface.

Figure 3.10 (a) XRD spectra of the films grown at different temperature with same (N+Sb)/N and N/(Sb+N) ratios.

Figure 3.11 Growth temperature dependence of N content in $InSb_{1-x}N_x$ epilayer.

Figure 3.12 XRD results (004) of the InSbN alloys at different N/(N+Sb) ratio, R1166 (0.93), R1176 (0.95) and R1178 (0.88), at a fixed growth temperature of 505 °C.

Figure 3.13 PL spectra of alloys with (a) different growth temperature and (b) different N/(N+Sb) ratios, respectively.

Figure 3.14 Band gap energy changes with the growth temperature.

Figure 3.15 PL spectra of the sample R1166 at a wide temperature range from 10 K to 296 K.

Figure 3.16 XPS spectra of the alloy grown at 505 °C with N/(Sb+N) ratio of 0.93, referring to the sample R1166.

Figure 3.17 Lattice strains $\Delta a/a_0$ of InSb caused by different N point defects with the densities of N content.

Figure 4.1 Spectra of XRD obtained from (004) diffraction of annealed and unannealed $InSb_{1-x}N_x$ samples.

Figure 4.2 PL spectra of the alloys with and without annealing treatment measured at 10 K.

Figure 4.3 PL spectra of the sample annealed at 450 °C for 3, 5 and 10 mins, respectively.

Figure 4.4 Temperature dependence of PL spectra of the alloy annealed at 450°C.

Figure 4.5 XPS spectra in N1s of InSbN alloy, (a) before annealing and (b) after annealing at 450°C.

Figure 4.6 XRD (004) 2θ /ω scans of samples annealed at different temperatures.

Figure 4.7 XPS spectra in N1s of InSbN alloys after annealing at (a) 440 ^{o}C and (b) 450°C.

Figure 4.8 PL spectra of the alloys annealed at 440 ^{o}C, 450°C and 460 ^{o}C measured at 10 K.

Figure 4.9 Temperature dependence of PL spectra of the alloy annealed at 450°C.

Figure 4.10 PL spectra of the alloys grown with N/(Sb+N) ratios of 0.85 and 0.9, respectively, measured at 10 K.

Figure 4.11 XPS spectra in N1s of the InSbN alloy grown with the N/(Sb+N) ratio of 0.9.

Figure 5.1 InSb nanorods grown at diffrerent temperatures on InSb (100) substrate with a fixed V/III ratio of 60.

Figure 5.2 InSb nanorods grown at diffrerent V/III ratios on InSb (100) substrate at a fixed temperature of 390 ^{o}C.

Figure 5.3 EDX analysis performed in the top region of InSb. (a) The SEM image of the probing area, and (b) the corresponding EDX spectrum.

Figure 5.4 SEM images (45° angle view) of InSb nanowires epitaxially grown on InSb (111) B substrate, from 380 ^{o}C to 430 ^{o}C, with a V/III ratio of 50

and growth time of 30 mins, respectively. Dependence of morphologies on temperature is clearly observed.

Figure 5.5 InSb nanowire diameter and growth rate as a function of temperature from 380 ^{o}C to 430 ^{o}C.

Figure 5.6 XRD spectra of InSb nanowires grown at 400 ^{o}C. InSb substrate was measured for reference.

Figure 5.7 From (a) to (d), 45° angle view SEM micrographs of InSb nanowire morphology evolves with input V/III ratio from 30 to 60 at a fixed temperature of 400 ^{o}C. (e) Quantitative relation between growth rate, diameter and V/III ratio.

Figure 5.8 EDX analysis at the top area of InSb nanowire. (a) Image of the probing area, and (b) the corresponding EDX spectrum.

Figure 5.9 EDX Line scan of a single InSb nanowire. The inset curve indicates the indium and antimony varies along the InSb nanowire.

Figure 5.10 Schematic illustration of the growth process of a InSb nanowire. (a) and (b) An Au nanoparticle absorbs In and Sb atoms from the vapor and forms an alloy droplet, the alloy droplet is preferably absorbing indium than antimony at this stage; (c) the intake of antimony to the alloy speeds up and InSb nanowire starts growing; (d) the content of nanowire gradually reaches 50: 50 (In: Sb) at% ratio to the end of growth.

Figure 5.11 Phase diagram of the $AuIn_2$-InSb system.

Figure 5.12 45° angle view SEM images of InSb nanowire dependent on growth temperature from 390 ^{o}C to 410 ^{o}C with a fixed V/III ratio of 45.

Figure 5.13 45° angle view SEM images of InSb nanowire dependent on V/III ratio from temperature from 30 to 60, with a fixed V/III ratio of 400.

Figure 5.14 (a) SEM photograph of the EDX analysis at different point areas along a InSb nanowire. (b), (c) and (d) The EDX spectrum to the relative point areas.

Figure 5.15 The binary phase diagram of the In-Sb system.

Figure 5.16 Top view SEM photograph of InSb nanowires synthesized at different temperatures.

Figure 5.17 (a) SEM photograph of selected area EDX measurement on the sample grown at 425 ^{o}C. (b) The corresponding EDX spectrum.

Figure 5.18 (a) SEM photograph of the EDX line scan of a single InSb nanowire, and (b) the curve of antimony and indium content along the nanowire.

Figure 5.19 The binary phase diagram of the Au-Sb system.

Figure 6.1 45° angle view SEM images of InSb nanowire dependent on growth temperature from 390 ^{o}C to 420 ^{o}C with a fixed V/III ratio of 45.

Figure 6.2 XRD spectra of InSb nanowires grown at 410 ^{o}C. GaAs substrate was measured for reference.

Figure 6.3 InSb nanowire diameter and growth rate as a function of temperature from 390 ^{o}C to 420 ^{o}C.

Figure 6.4 SEM images of samples prepared with different V/III input ratios at a fixed temperature of 410 ^{o}C.

Figure 6.5 High resolution transmission electronic microscopy image of the head tip of a single InSb nanowire

Figure 6.6 (a) SEM photograph of selected area EDX measurement on the sample grown for 3 mins at 410 ^{o}C, and with a V/III ratio of 40. (b) EDX spectrum of the sample.

Figure 6.7 SEM images of the dependence of samples grown at 400 ^{o}C, 410 ^{o}C and 420 ^{o}C on Si substrate.

Figure 6.8 Top view SEM picture of InSb nanowires at a higher magnification

Figure 6.9 Schematic illustration of the growth process of a DM InSb nanowire on Si substrate. (a) an Au nanoparticle absorbs In and Sb atoms from the vapor and forms an alloy droplet, then the reaction between In and Sb initiates the growth of InSb nanowire, (b) a disturbance induced decrease of In and Sb concentration near the alloy droplet reduces the size of the droplet and results in a decrease of the nanowire diameter; (c) a small size alloy droplet absorbs fewer atoms from the vapor, which induces the increase of the In and Sb concentration near the alloy droplet and finally results in the increase of the droplet size and nanowire diameter; (d) the size-resumed alloy droplet draws more atoms from the vapor, which reduces the In and Sb concentration and the nanowire diameter again; and (e) continuation of the steps depicted in steps c and d forms a InSb DM nanowire.

Figure 6.10 Illustration of force balances at the triple-phase boundary.

LIST OF TABLES

Table 2.1 Physical parameters of InSb.

Table 2.2 Band structure parameters for InSb.

Table 3.1 Growth parameters of the InSb films on InSb substrate.

Table 3.2 Values of mobility and carrier concentration of the samples grown at different substrate temperatures.

Table 3.3 InSb films deposited at different V/III ratio with same temperature.

Table 3.4 V- III ratio, N-V ratio, growth temperature, pressure and time of $InSb_{1-x}N_x$ alloys growth.

Table 4.1 PL peak positions of InSbN alloy annealed at 450 °C at different temperatures.

Table 5.1 Specific data of element atomic percent of the corresponding spectrum.

CHAPTER 1. INTRODUCTION

1.1 Motivation

(i) InSb and InSbN materials for long wavelength application

In the area of infrared detector, interest has been mainly focused on the wavelengths in the two atmospheric windows 3–5 µm [middle wavelength infrared range (MWIR)] and 8–14 µm (LWIR region) (as indicated in Figure 1.1), as the atmospheric transmission of light in these two bands is the highest.

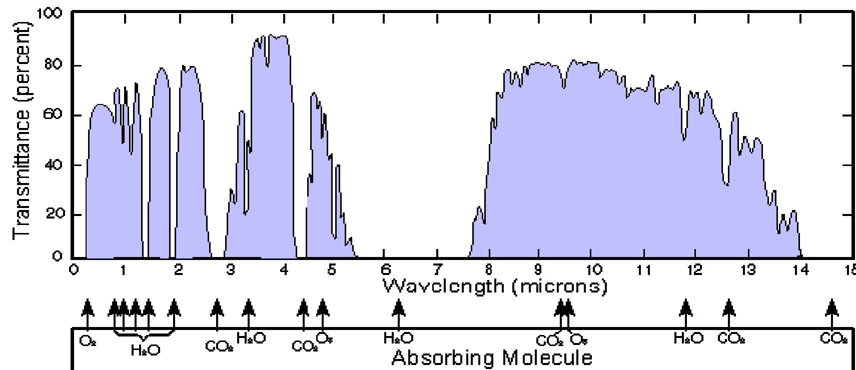

Figure 1.1Two transmission window in atmosphere, one is mid wavelength infrared (MWIR) between 3-5 µm, the other is long wavelength infrared (LWIR) between 8-14 µm.

For InSb, the cut-off wavelength of 7 µm at room temperature may block its direct utilization in the LWIR region. However, the transition wavelength of InSb could be red-shifted to longer wavelength by adding nitrogen (N) due to the negative band bowing effect, which excitingly rekindles the hope of InSb's application in the LWIR

area. As a candidate for the application in long wavelength region, $InSb_{1-x}N_x$ has many advantages over other materials. Compared to $InSb_{1-x}As_x$ or $InSb_{1-x}Bi_x$, the N incorporation required in $InSb_{1-x}N_x$ alloy to reach a band gap of 0.1 eV is only about x = 0.01[1], which is much lower than the requirement for $InAs_xSb_{1-x}$ and $InSb_xBi_{1-x}$ alloys (x = 0.1) [2-6]. Moreover, the large amount of arsenic or bismuth may lead to material quality issues. HgCdTe is still dominating the area of long wavelength. However, $InSb_{1-x}N_x$ is likely a better choice for optoelectronic devices in the long wavelength area. Auger recombination rate is considered as the limiting factor in the detector sensitivity and light emitting diode efficiency. Recent experiments reveal that the Auger recombination rate of InSbN alloys is one- third that of the equivalent band gap of HgCdTe due to their high electron mass and conduction band nonparabolicity [7]. This indicates that the device based on InSbN may have better performance than that of HgCdTe. These properties make InSbN alloy an important alternative for long wavelength device and naturally a great deal attention has been paid on it recently.

In the early report, the growth of $InSb_{1-x}N_x$ was made by electron cyclotron resonance assisted molecular beam epitaxy (ECR-MBE). For this deposition method, ECR plasma was used to crack N_2 efficiently for the incorporation into InSb. By using the same approach, $InSb_{1-x}N_x$ alloys with up to 10% N were made by T. Ashley et al. Light emitting diodes comprising a super lattice of $InSb_{0.945}N_{0.055}$/InSb were also made to measure the band gap and an emission wavelength of 10.5 μm was observed [8]. Later on, in order to continuously enhance N incorporation, hydrogen was intentionally introduced to the ECR source to make nitrogen plasma sustain at the lower pressure by Veal et al [9]. The N incorporation is turned out to be doubled,

although undesirable N- H complexes are also produced by this approach. Recently, radio frequency (rf) plasma- assisted MBE has been introduced to prepare $InSb_{1-x}N_x$ alloys. This technique reportedly generates more neutral atomic nitrogen species compared to the ECR MBE and may avoid significant number of energetic ions resulting from ECR source. By using rf MBE, H. T. Pham et al. have made InN_xSb_{1-x}alloys with substitutional N up to 2% [10-11]. Except for MBE, N ion implantation is also usually used to prepare $InSb_{1-x}N_x$ [12]. By utilizing two- step ion implantation, D. H. Zhang et al. have fabricated uniform $InSb_{1-x}N_x$ alloys and first reported photo-detection at 11.5 µm, which demonstrated that the alloys can be used for long wavelength infrared photo-detection [13]. Even though many important progresses have already been made, there are still some issues which need to be solved before the practical application of $InSb_{1-x}N_x$ alloy in the long wavelength range. Firstly, it is about the $InSb_{1-x}N_x$ alloy quality. Although ECR plasma enables efficient splitting of N_2, it also produces high density of ions which are very harmful to the quality of material. ECR with hydrogen addition may do well to N incorporation, but it will bring undesirable N- H complexes at the same time. High density of point defect will be introduced by low energy N_2 ion implantation and this technique also results in a non uniform electron concentration depth profile in the layer of $InSb_{1-x}N_x$ alloy. Therefore, there is much room for enhancement in term of the quality of $InSb_{1-x}N_x$ alloys. Secondly, further improvement is still needed for N incorporation. N incorporation in $InSb_{1-x}N_x$ alloys has already reached 5% or higher, but only a part of nitrogen is active by substituting Sb and the rest of N maybe in the form of the interstitial sites. Compared to the band reduction theory, the N incorporation needed in $InSb_{1-x}N_x$ alloy is only about $x = 0.01$ to reach a band gap of 0.1eV, Further research needs to be elaborated on enhancing effective N in $InSb_{1-x}N_x$ alloys. Thirdly,

specific information about point defects such as anti-sites, interstitials in $InSb_{1-x}N_x$ alloys is still lacking. Their energy levels in the band gap, and their effect on the electrical and optical properties of material, are yet unclear. Further investigations will therefore be required to address these issues.

Another existing issue to be addressed is the lattice mismatch between InSbN alloy and the substrates, since the main application of InSbN alloy is imaging where uniformity and low defect density is of paramount importance. So far, most reported hetero-epitaxial InSbN layers were grown on GaAs substrate [8, 9, 11]. However, due to a large lattice mismatch (~12.6%), the results about InSbN on GaAs substrate are still far from device application for infrared photodetector. There were limited reports on InSbN alloy grown on other III-V substrates. One of them is by S. M. Kim et al. who grown InSbN quantum dots on InAs substrate [14]. By decreasing the dimension of the material, the defects due to the lattice mismatch could be reduced dramatically. For GaSb and InAs substrates, the lattice mismatch (~6%) to InSb is much smaller than that of GaAs, which makes them an advantage as epitaxial substrates for InSbN. And thus more attention is worthy to be paid on the exploration of high quality InSbN on GaSb and InAs substrates.

It is noted that many devices like p-n diodes, and detector have already been made by some groups [15-17]. However, the quantum efficiencies of the devices are still inadequate. So, much more effort needs to be paid on the improvement of the quantum efficiency so as to realize the practical use of $InSb_{1-x}N_x$ alloy device in the region of long wavelength.

(ii) One dimensional InSb for application in nanoelectronics

Not only in the area of infrared devices, InSb also has significant potential application in high frequency, low power and spin electronic devices, due to its special properties like the highest electron mobility, smallest effective mass, and largest g factor among all III-V binary material systems [18-21].

For future electronic devices in industry, InSb is presumably necessary integrated into other material systems like GaAs, Si, etc [22-23]. However, growth of bulk InSb on other III-V semiconductors or Si is always a big challenge due to the large lattice mismatch between them. It will lead to stress when InSb was hetero-epitaxially grown on other materials, and consequently accompanying the formation of misfit dislocation, which may dramatically deteriorate the performance of electronic devices. A normal way used to solve this problem is to introduce a buffer layer between InSb and substrate, which may relax the stress by forming defects after a certain critical thickness is reached [24-25]. Another road of addressing the misfit issue is to synthesize InSb in one dimensional nanowires instead of thin films. On a lattice mismatch substrate, a nanowire grown hetero-epitaxially can relax part of the strain energy by elastically deforming its shape [26]. The tendency for bringing misfit dislocations at the wire-substrate interface is reduced due to the strain energy reduction, which is particularly for the situation of small diameter nanowires. It is consequently desirable to grow InSb nanowires with small diameters to increase the versatility referring to the choice of the substrate materials. What's more important, with the reduction of size in one dimension to the scale of nanometers, some novel and unique properties may happen to a crystal due to the surface effect or quantum size effect. Therefore, study on InSb nanowire means a lot on both integration to other material systems and discovery of new properties of InSb.

At present, the work on InSb nanowire is supposed to be in the stage of material study. However, it should be also beneficial to the detector applications of InSb. For example, the infrared detectors have all been fabricated based on bulk InSb in the past. InSb in nanostructures may lead to the change of band energy of InSb, and thus enlarge the responsive range of infrared light for a detector device. Due to the quite narrow band gap, the photodetectors based on InSb have some disadvantages such as limited absorbing area and low response efficiency. For a nano-array with high quality, high density, and high uniformity, the surface-to-volume ratio is normally much higher than that of bulk material, which could effectively increase the contact area between the device and environmental signal, and thus improve the response efficiency.

In the past, most research works were located on bulk InSb, while on InSb nanowire was scarce, perhaps due to the difficulty of growth of this material. In this thesis, the preparation and properties of InSb nanowires were carefully studied with purpose of exploring its new application in nanoelectronics.

1.2 Objectives

Driven by above motivations, the objectives of this thesis are described as below:

1. To eptiaxially grow InSb films and $InSb_{1-x}N_x$ alloys on InSb substrate by metal-organic chemical vapor deposition (MOCVD) and characterize their properties. In order to meet the requirements of practical use, the primary purpose of growing $InSb_{1-x}N_x$ alloy is to extend the cut-off wavelength to longer value. Therefore, the optimum conditions of preparing $InSb_{1-x}N_x$ alloys

with high quality and long cut-off wavelength by MOCVD will be investigated in details.

2. To grow a of $InSb_{1-x}N_x$ alloys hetero-epitaxially on GaSb and GaAs substrates by MOCVD. GaSb and GaAs have been normally used as substrates for growing InSb even there is a big lattice mismatch between them. Material quality is the primary issue of $InSb_{1-x}N_x$ alloys by hetero-epitaxial growth. Annealing treatment will be done to improve the film quality and investigate the change of the N bonding at the same time.

3. To grow and study one dimensional InSb by MOCVD. As at present, reports about InSb nanowires by MOCVD in literature are still limited, and many properties of InSb nanowires are still not very clear.

4. To synthesize InSb nanowires hetero-epitaxially on GaAs and Si substrates by MOCVD.

1.3 Major contributions

The main contributions in this thesis are as follows:

1. High quality InSb films on InSb substrate have been prepared by using MOCVD in the H_2 atmosphere with various growth parameters in temperature, and V/III ratio. A defect related emission resulting from the antisite Sb_{In} defects has been demonstrated for the InSb epilayers.

2. $InSb_{1-x}N_x$ alloys have been epitaxially grown on InSb substrate by MOCVD. A nitrogen incorporation as high as 0.26% was achieved in the alloy, and the band gap of the InSbN alloy has been successfully reduced by the nitrogen incorporation. The N bonding in the alloys has been studied by various characterization techniques. It is found that antisite N (N_{In}) is the dominant in the alloy, while the substitutional (N_{Sb}) occupies only a small part of the total N incorporation.

3. The effect of GaSb and GaAs substrates on $InSb_{1-x}N_x$ epilayers has been studied. The PL measurement at 10 K indicates that the transition wavelengths of InSbN alloys are shifted to 6.3 μm and 7.2 μm for the alloys on GaSb and GaAs substrates, respectively. The effect of annealing treatment on the $InSb_{1-x}N_x$ alloys has been studied. The defects and N bondings in the alloys have also been carefully investigated.

4. The synthesis and characterization of InSb nanowires epitaxially grown on InSb (100, 111) substrates by MOCVD have been performed. The dependence of InSb nanowire growth on V/III source ratio and, temperature has been discussed in detail. Uniform InSb vertical nanowires with high density on InSb (111) substrate were achieved. The underlying growth mechanism of InSb nanowires was also demonstrated.

5. InSb nanowires have been successfully realized on both GaAs and Si substrates. The underlying growth mechanism of InSb nanowire on different substrates has been investigated accordingly. These results may provide important information on controllable growth of InSb nanowire, and have significance for new applications of InSb in chip-scale industry.

1.4 Organization of this report

This thesis consists of seven chapters. It starts with the motivation, objective and major contributions in chapter 1.

Chapter 2 gives a rough introduction of III-V semiconductors and InSb. A brief overview of current status about the photo-detector devices in the middle and long wavelength range is also included. In addition, this chapter also elaborates some fundamental knowledge about the physics of nanoscience and fabrication of nanomaterials.

This chapter also describes the experimental setup and procedures employed in this project. The principle of metal-organic

chemical vapor deposition is introduced. Various characterization methods such as high resolution XRD, X-ray photoelectron spectroscopy, hall measurement, photoluminescence, etc, are also reviewed.

Chapter 3 introduces the growth of both InSb films and $InSb_{1-x}N_x$ alloys by MOCVD. The properties are characterrized by different methods and implications of the results are analyzed.

Chapter 4 is about the growth and characterization of $InSb_{1-x}N_x$ alloys on GaSb and GaAs substrates. The characterization and discussion are also presented in the chapter.

Chapter 5 presents the preparation and characterization of InSb nanowires on InSb (100, 111) substrates.

Chapter 6 gives the synthesis and characterization of InSb nanowires on GaAs and Si substrates have also been demonstrated in this chapter.

In the end, the last chapter gives a summary of the main work. Recommendations are also proposed for future researchers.

CHAPTER 2. BACKGROUND

2.1 III-V semiconductor materials

III-V compound semiconductor materials are basically composed of group III (Boron, Aluminum, Gallium, Indium) and group V (Nitrogen, Phosphorus, Arsenic, Antimony) elements in the periodic table. At present, Silicon is the most widely used material in semiconductor industry. Compared to Si, III-V compound semiconductors are usually fragile and their growths are more difficult. However, there is an extraordinary advantage for them, the lattice parameter and band-gap could be tuned to any desired values by combing more than two elements from the group III and V columns with different composition to from ternary or quaternary alloys. Figure 2.1 shows the III-V development milestones [27], which demonstrates that a very large range of wavelength from blue to near infrared light can be covered by many ternary

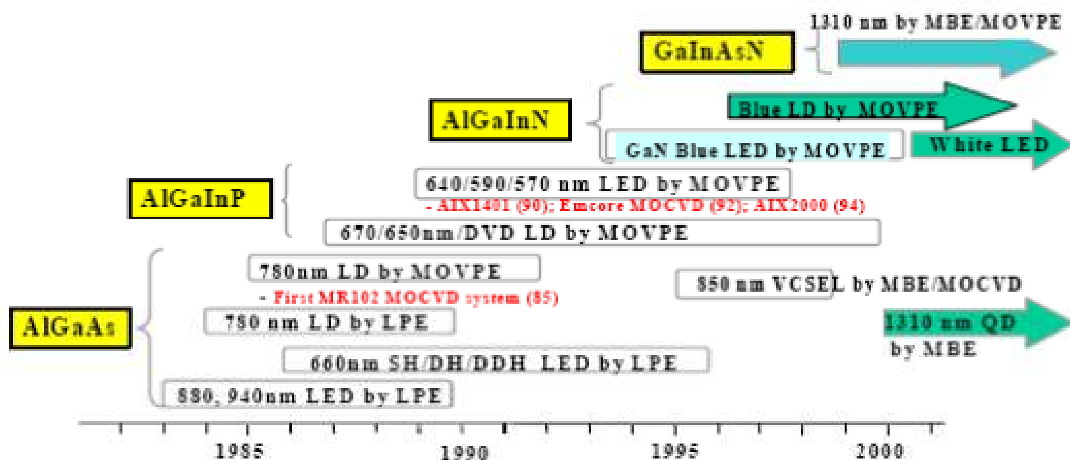

Figure 2.1 III-V development milestones.

or quaternary alloys, and for now billion US dollars industry has already been formed in laser diode, light-emitting diode, photo-detector, hetero-structure bipolar transistor and so on.

The second advantage of III-V compound semiconductors over Si is their high mobility, which makes their great application in high speed and high frequency device. Figure 2.2 gives a development of high frequency device by using different materials [28]. Another very important application benefited from the high mobility is COMS. Si CMOS has enjoyed its prosperity for several decades. However, with the continuous down scaling, Si CMOS design may approach its bottleneck due to the limitations of the silicon physical properties.

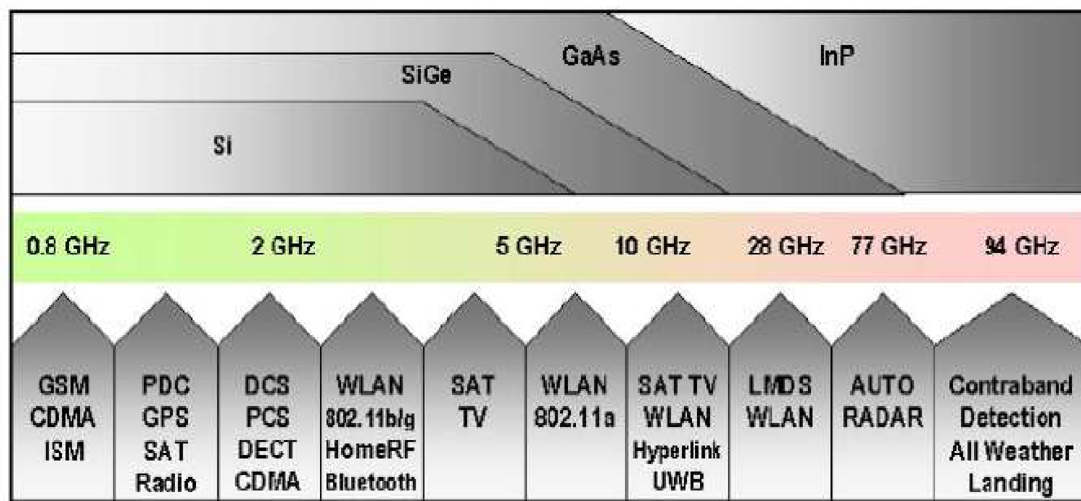

Figure 2.2 Wireless frequency spectrum showing RF semiconductor technologies and applications.

Recently, InGaAs, with indium mole fractions >70%, has been proposed as the channel materials to substitute Silicon in III-V transistors for CMOS [29].

Furthermore, materials of even higher electron mobility such as InAs and InSb are also considered having the potential as channel materials in future to achieve higher

Table 2.1 Physical parameters of InSb.

Crystal structure	**Zinc Blende**
Band gap	**0.178 eV (300 K)**
	0.23 eV (78 K)
Lattice constant	**6.4788 A**
Density	**5.77g cm^{-3}**
Melting point	**525 ^{o}C**
Infrared refractive index	**4.0**
Bulk modulus	**4.7×10^{11} dyn cm^{-1}**
Optical phonon energy	**0.025 eV**
Mobility	**7.7×10^{4} cm^{2}/V.S (300 K)**
	1.2×10^{6} cm^{2}/V.S (77 K)
Thermal expansion, linear	**5.37×10^{-6} $^{o}C^{-1}$**

performance. Although, for the real industrial application, there are still many problems unsolved such as lattice mismatch, poor interface quality, high-k dielectric growth, and off-state current. MOCVD is the most promising manufacturing technique of solving these problems. Besides the mentioned above, III-V semiconductors also have very important applications in photo-detector, laser device, solar cell and so on [30-35].

2.2 Physical properties of InSb

Among all binary III-V semiconductors, InSb is a very special one with important application in infrared detectors, optoelectronics and magnetic field sensors [18-21, 36]. It has the smallest band-gap with a cut-off wavelength of 7 μm at room temperature and 5.5 μm at 80 K [37]. The properties of InSb have already been researched for decades of years. Table 2.1 indicates some basic physical parameters of the InSb semiconductor [38-41]. During past thirty years, numerical studies on the fundamental band structure of InSb have been conducted by different ways such as Local density approximation (LDA), pseudo-potential, k.p model, empirical tight binding (ETB), etc, [42-47]. The particular small band gap of InSb leads to a strong band mixing and nonparabolity, which makes the effect of higher bands need to be taken into account by second order perturbation theory. Some recommended band structure parameters for InSb are given in the table 2.2 [48].

Table 2.2 Band structure parameters for InSb.

2.3 Utilization of InSb in infrared area

2.3.1 InSb for middle wavelength infrared region

InSb has the narrowest bandgap among the III-V compound semiconductors. It is extremely important for application as infrared detectors, providing excellent performance in the 1 to 5.5 μm wavelength region. In the area of infrared detectors,

interest has been mainly focused on the wavelengths of the two atmospheric windows: 3–5 μm [middle wavelength IR (MWIR)] and 8–14 μm (LWIR region). The atmospheric transmission of light in these two bands is the highest. InSb could cover the entire MWIR region up to 5.5 μm. Besides, the manufacturing of InSb is mature and high quality InSb wafer with diameter larger than 7 cm is commercially available [49]. Single crystal p–n junction technology yields high speed, low noise detectors with excellent uniformity, linearity and stability. All these advantages make InSb very suitable for the application in the MWIR region. Figure 2.3 shows the spectral detectivity of the InSb detector and indicates it has very high responsitivity in the range of 1 to 6 μm [50]. In infrared device technology, the development of large two dimensional focal plane arrays (FPAs) was a significant advance and the material

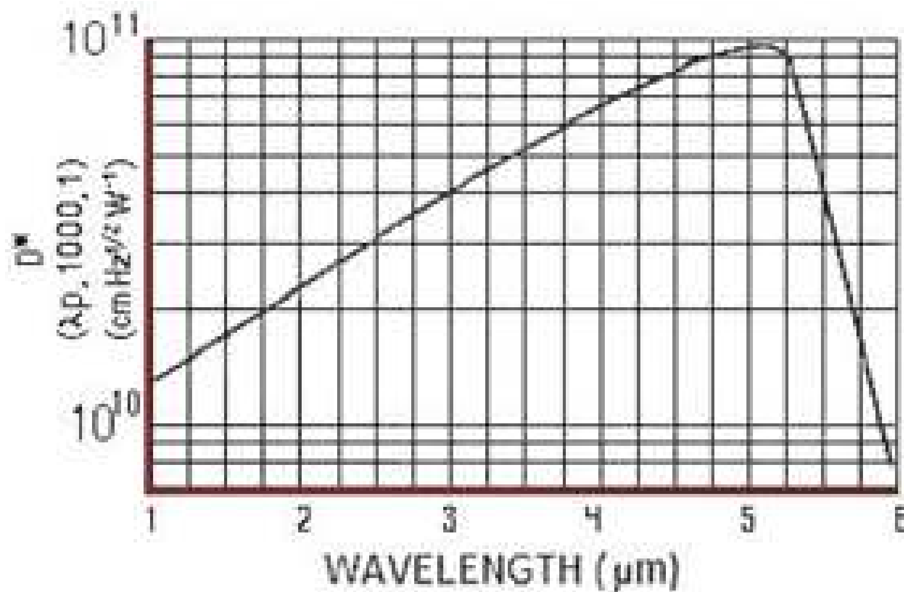

Figure 2.3 Spectral detectivity of InSb detector

which has attracted the most attention to date is InSb. Infrared devices are usually made with both p-n junctions and MIS capacitors. For the staring arrays, the linear formats of 64, 128, 256, 640 and 1024 have already been realized in actual high background and astronomy application [51-56].

In the MWIR region, except InSb, there are many other types of detectors based on different materials such as InAs, PbSe, HgCdTe, etc [57-61]. Each kind of them has its own advantages. But among these materials, HgCdTe is the most widely used semiconductor for IR photodetectors due to its high quantum efficiency. And the large flexibility of band gap makes HgCdTe not only fit for the MWIR region but also the LWIR region (8 - 14 μm). At present, kinds of LWIR detectors like Ge:Hg, Si:As PbSnTe, GaAs QW have been developed to compete with HgCdTe [62-67]. But none of these competitors can totally surpass HgCdTe detectors in terms of fundamental properties. HgCdTe now still dominates the LWIR industry with billions of dollars' scale due to its overall higher performance. However, as one basic material for IR detectors, HgCdTe also suffers from many disadvantages like lattice, surface and interface instabilities, uniformity issues from the high mercury vapor pressure, highly toxic compounds, mass production from weak Hg-Te bond [68-70], etc. Therefore, investigation still needs to be continued to improve the HgCdTe IR detectors or even find new ideal alternatives.

2.3.2 Materials for long wavelength infrared region

For InSb, the cut-off wavelength of 7 μm at room temperature may block its direct utilization in the LWIR region. Luckily, the band gap of InSb could be extended by

adding group III element thallium (Tl) or group V elements arsenic (As), bismuth (Bi), and nitrogen (N), which excitingly rekindles the hope of InSb's application in the LWIR area. TlSb is one semi-metal with a band gap of -0.95 eV. It is suggested that by alloying with InSb, the band gap can be tuned from -0.95 to 0.17 eV [71]. According to the calculation, the gap reaches 100 meV at x=0.09 at 0 K and 100 meV

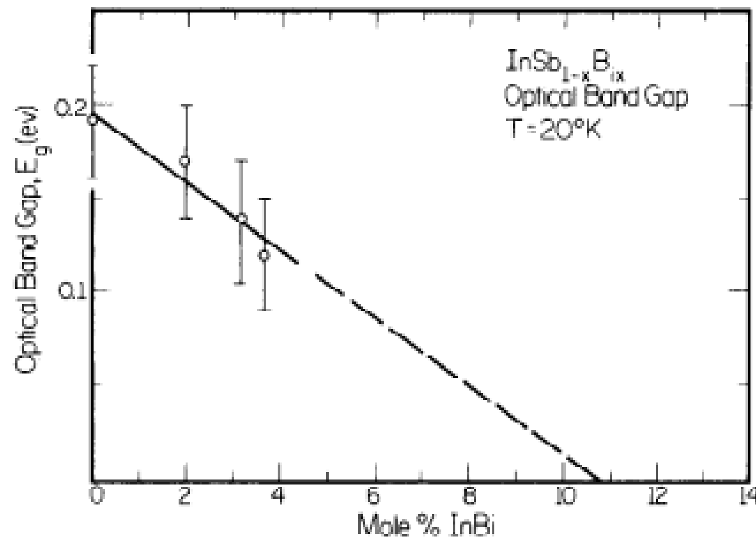

Figure 2.4 Optical band gap of $InSb_{1-x}Bi_x$ as a function of composition.

at x= 0.05 at 300 K, which means perhaps a relatively small amount of Tl (approximately 10%) is needed to narrow the band gap to the required value [72]. Several works about the preparation and properties of InTlSb have been reported and a shift of absorption spectra from 5.5 μm for InSb up to 8 μm for InTlSb was observed in transmission measurement by Y.H. Choi, et al [73-75]. As a candidate of alternative for HgCdTe, InSbBi was put forward very early in 1960s and attracted

much attention in later years [76-80]. In-Sb-Bi ternary phase diagrams reveal the solubility of InBi into InSb is very small, which means it is difficult to grow this mixed alloys. Earlier work indicated that the maximum equilibrium solubility of Bi was 2.6 % but at metastable solubility limit 12 % of Bi can be incorporated. Figure 2.4 gives the spectra of optical band gap of $InSb_{1-x}Bi_x$ changes with Bi composition [5-6, 79]. J. J. Lee, et al. have successfully demonstrated the room temperature operation of 8–12 µm InSbBi long wavelength infrared photo-detectors by making

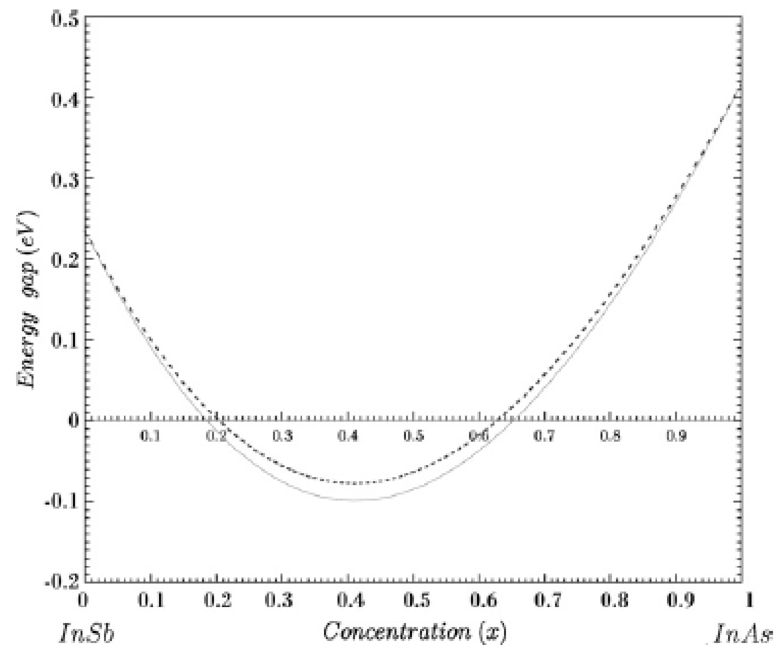

Figure 2.5 The dependence of energy band gap of $InAs_xSb_{1-x}$ on the composition.

InSbBi/InSb hetero-structures grown on GaAs by LP-MOCVD, although the corresponding Johnson noise limited detectivity was at a little bit low value of 1.23×10^6 $cmHz^{1/2}/W$. InAsSb alloy is another promising candidate based on InSb for the realization of IR detectors operating both in the 3–5 µm and 8–14 µm windows [81-

85]. Compared to HgCdTe, InAsSb has better stability, higher mobility and faster response. Figure 2.5 indicates the theoretical dependence of energy band gap of $InAs_xSb_{1-x}$ on the composition at 0 k. It can be seen that the band gap would reach 0.1 eV when x is near to a small value of 0.1 [86]. But according to the experimental results, the value of x needs to be about 0.3 to make the band gap reduce to 0.1 eV [84, 85]. As mentioned above, all these alloys InSbTl, InSbBi and InAsSb have the potential of application in the LWIR region. However, each of them also has some disadvantages, obstructing their adoption in detector device with satisfying performance. For example, the large miscibility gap limits Tl incorporation into InTlSb. Particularly, the element Tl is radioactive and very harmful to human body. InSbBi is very hard to grow due to the solubility limit of Bi. For InAsSb, it needs a large amount of arsenic to reduce the band gap to the requirement of value of 0.1 eV.

Type II Sb-based super-lattice, was first introduced by the Nobel laureate L. Esaki in 1970s, and then proposed for infrared detection applications by Smith and Mailhiot in 1987 [87-88]. Since then, various Type II Sb-based super-lattices like $InAs_xSb_{1-x}/InAs_ySb_{1-y}$, $InAs/In_xGa_{1-x}Sb$ have been grown and investigated in recent years [89-93]. For the application in infrared detection, one of the benefits of Type II superlattice is the capability to tune the detection cut-off wavelength in a very wide range by adjusting the thicknesses of constituent layers or changing the polarity of the bias applied on the device [94-95]. The devices based on Type-II Sb-based super-lattice may have better performance with low dark current density due to suppressed Auger recombination rate and tunneling current. Another advantage of Type-II Sb-based super-lattice is the promising low manufacturing cost on large substrates. [96]

All these benefits make Type-II Sb-based super-lattice as another alternative for HgCdTe in long wavelength infrared detection.

2.3.3 InSbN for long wavelength application

The incorporation of dilute quantities of nitrogen into III–V semiconductor compounds is well documented to dramatically reduce the band-gap of the material from that of the binary host [97-98], a great deal of work has been done to add small amounts of nitrogen into III-V semiconductors to modulate their band gap. This band gap bowing effect has been demonstrated in numerous III–V compounds including GaP [99-100], GaAs [101-102], InAs [103-104] and GaSb [105-106], which are shown

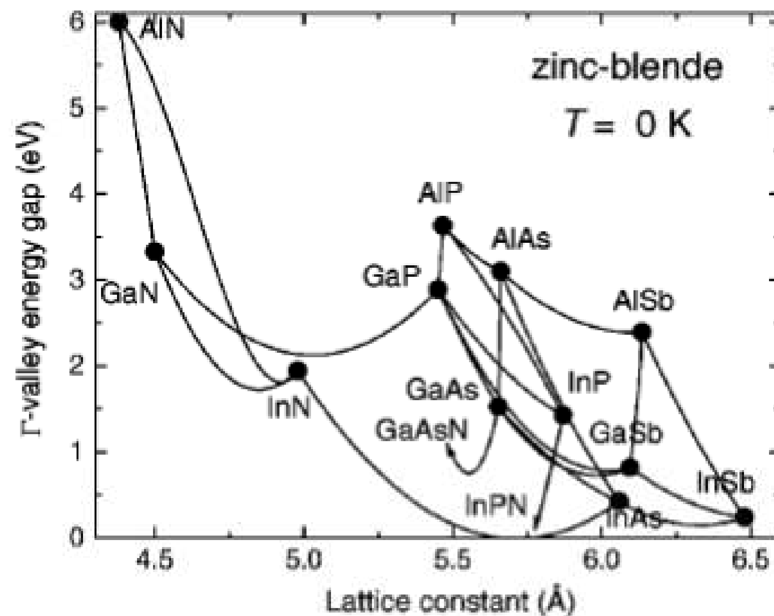

Figure 2.6 The Lattice constant, energy gaps for certain ternaries such as InAsN, GaAsN, InPN, etc.

in Figure 2.6. InSb is an ideal candidate for mid-infrared application. Since the discovery of this negative band-gap bowing effect by adding nitrogen, InSbN alloy has become another promising candidate for IR detectors in the atmospheric transmission window between 8 and 14 µm.

The dramatic band gap bowing in InSbN have been explained by a band anti-crossing model in which resonant localized N states within the conduction band interacts with the extended states of the conduction band [7, 107]. The theoretical band structure of $InSb_{1-x}N_x$ with small composition x can be analyzed using a ten-band k.p model previously developed for GaN_xAs_{1-x} [108-109]. The k.p approximation, which models the interactions between the E_c and E_v band, is modified to include the interaction of localized N states with E_c band of the InSb host. The k.p Hamiltonian can expressed as:

$$E_{N,C} = \begin{pmatrix} E_N - \alpha x & \beta\sqrt{x} \\ \beta\sqrt{x} & E_C - \gamma x \end{pmatrix} \tag{2.1}$$

For $InSb_{1-x}N_x$, the conduction band energy E_C = 0.177 eV, E_N = 0.647 eV, $\alpha = \gamma$ = 0.77 eV and β = 2.2 eV. Figure 2.7 indicates the E_C and E_V band edges and N level as a function of N content, calculated by the modified k.p model [110]. The calculated energies of E_+ and E_- subband edges resulted from the band anticrossing effect between the localized N states and the E_C of the InSb. The E_+ subband results from

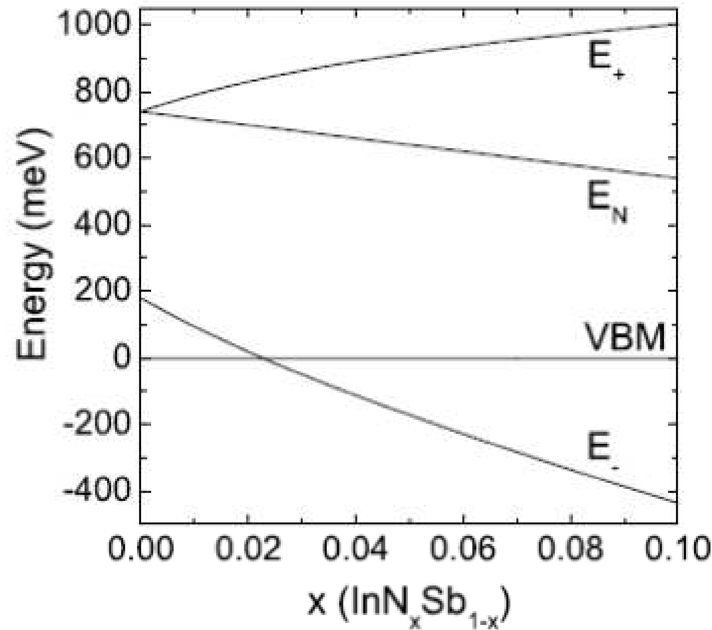

Figure 2.7 The E_C and E_V band edges and N level of $InSb_{1-x}N_x$ at 300 K as a function of x.

the E_N like states and E_- band acts the function of an E_C band. As shown in Figure 2.7, the band gap reaches zero at x ~ 0.022 and the band gap is negative at higher x values, indicating that the alloy is semi-metallic.

At the same time, as the band is reduced, the effect of mixing the localized N states with Γ- like E_C causes a very strong anticrossing and tends to increase the effective mass. The effective mass increase has been determined by the plasma reflection technique and it is shown to be consistent with pressure dependent differential reflectivity measurements.

2.4 Basics for one dimensional InSb

2.4.1 Nanoscience and nanotechnology

In recent years, nanoscience and nanotechnology have attracted a great deal of attention due to the huge potential implications in modern electronics industry. Nanowires are defined as structures that have a diameter in the range of tens of nanometers [111]. With the reduction in size of crystalline structures to nanoscale, the surface to volume ratio is considerable high enough that that the surface effects cannot be ignored anymore. As well, in nanowires, electrons could possibly quantum-confined laterally and thus could occupy discrete energy levels, thus may resulting in quite different electronic transparent behavior from which is found in bulk materials. Consequently, the surface effects and quantum confinement effects will become obvious on materials in nanoscale, leading to some interesting properties normally negligible in bulk [112].

The rising of nanowires have brought new building blocks for nanoscale electronic and optoelectronic devices. However, device components have been mainly fabricated in laboratory because the transition from promising science to practical use requires an even more thorough understanding and control of the growth and properties of nanoscale structures. To date, much of the interest in nanoscience has been focused on semiconductor materials due to their particular importance for electronics. Throughout the microelectronics, Silicon is the most widely used semiconductor due to its superior properties like high repeatability and stability, low hysteresis and susceptibility, naturally-forming native oxide, etc. Other semiconductors closely related to Si including other group IV materials such as Ge,

binary III-V materials such as GaAs, and binary II-VI materials including ZnO, ZnS, ZnSe, etc, were also the focus in research [113-120].

For nanostructures, including nanowires, there are two general manufacturing ways, referred to as "top-down" and "bottom up", first applied to the field of nanotechnology by the Foresight Institute in 1989 to distinguish between conventional and molecular manufacturing [121]. The top-down approach normally uses traditional workshop or microfabrication methods liking cutting, milling, lithographing, to make the materials into desired shape and order. This method has dominated materials processing over the last century, and now are still important part for fabrication of electronic devices. However, as the continuously shrinking of devices in length scales, the top-down way gradually cannot follow the needs, techniques to carve out ever-smaller structures are difficult to find. Bottom-up method, in contrast, is a way of self-organizing atoms to shape increasingly larger structures. By using the concepts of molecular self-assembly, the atoms are crystallized in a controlled way from vapor or liquid sources, forming uniform and highly ordered nanoscale structures. Such bottom-up method should be able to produce electronic components in mass and cut down the cost comparing with the top-down approach.

2.4.2 Nanowire growth mechanism and techniques

The growth of nanowires is typically in a bottom-up way, generally including two main categories of growth: template-directed and freestanding. Template-directed growth normally relies on a template with pre-defined shape to confine the forming

crystal, and thus obtaining nanowire through suppressing growth in other dimensions by physical confinement. Freestanding nanowires are normally epitaxially grown on a substrate with the relative distinction of growth rates in different directions. At present, the freestanding way is the most widely used in nanowire growth due to its exceptional versatility in terms of material and substrate options, variety of fabricating methods, etc. However, freestanding growth of nanowire is more complex to understand, leading to the uneasily controllable growth, which is one of primary difficulties for the practical integration and use in device.

The dominant category of freestanding nanowires is the ones grown with the assistance of small seed particles, which may lower the activate energy of growth and provide a tanker where nanowires spring outward from. The particles used are typically different metals like Au，Ag，Ni，Cu, etc, and they are normally not consumed with promoting the growth [122-126]**.** For one dimenstion semiconductor nanowires, vaiety of mechanisms like Vapor-Liquid-Solid (VLS), Vapor-solid-Solid (VSS), Vapor-Solid (VS) have been developed for explaining their growth [127-131]. Among these, VLS mechanism proposed by Wagner and Ellis has been used mostly wildly for the synthesis of semiconductor nanowires such as Si, GaN, GaAs, InAs, ZnO, ZnS, SnO_2 etc. The VLS mechanism assumes that a liquid alloy forms above the eutectic point, which can rapidly absorbs vapor source to supersaturation levels and one dimensional growth can subsequently occur from alloy seeds. The principle for Si nanowire growth is schematically shown in Figure 2.8.

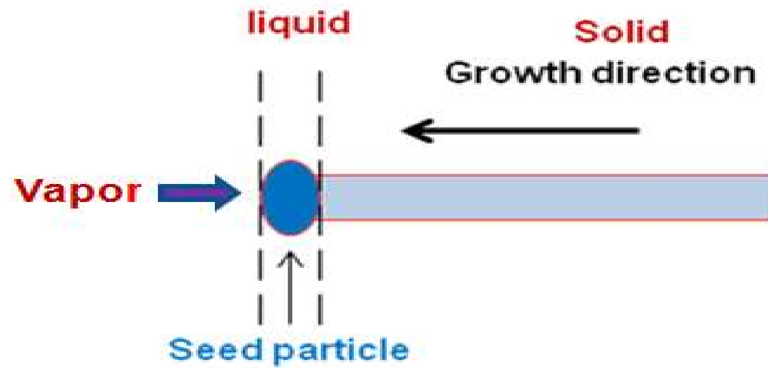

Figure 2.8 Diagram of the process of the VLS mechanism.

(1) Vapor-liquid solid (VLS)

The Au particles deposited on Si substrate react first with Si to form Au–Si alloy droplets at a certain temperature. As shown in the Au–Si phase diagram in Figure 2.9, Au and Si can form a solid solution for all Si content (0–100%)， the melting temperature of the Au– Si alloy at the eutectic point is very low (about 363 ^{o}C at an Si concent of ~20% [132]. At a temperature above 363 ^{o}C, The Au–Si droplets absorb Si from the vapor phase resulting in a supersaturated state. With the temperature slowly falling down, Si atom will precipitate from the supersaturated droplets along the separate line of liquid-solid until the eutectic point, and thus fulfill the formation of nanowire.

(2) Vapor-solid

In comparison to VLS growth, VS (vapor-solid) is a kind of growth with no use of seed particles or called self catalytic growth, and mainly used to prepare semiconductor and oxide nanowires like ZnO, SnO_2, In_2O_3, AlN, and so on [131, 133-135]. In the case of Si whisker from the reaction between $SiCl_4$ and H_2, the

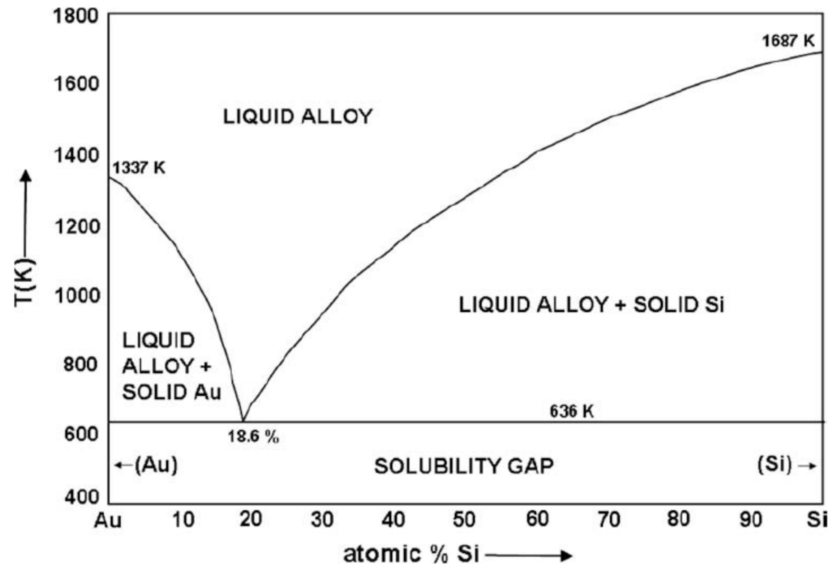

Figure 2.9 Phase diagram of Au-Si alloy.

temperature needs to be above 800 ^{o}C without the assistance of catalyst. This feather of VS is a major difference from VLS method. Although VS method may not lower the activation energy as VLS method does, it has its own advantages. Since no seed particle, the contamination from the metal catalyst could be avoid, and consequently leading to less defect resulting from environment and high quality of production, which may have positive influence on electron transport.

(3) Vapor-solid-solid

VSS (vapor-solid-solid) is another widely used mode to evaluate nanowires [129-130]. Similar to VLS mode, VSS also adopts foreign metal particles as catalyst. But the difference is that the growth temperature for VLS is above eutectic point (T_E), ensuring the existence of a supersaturation alloy for growth. While the temperature for VSS mode is below T_E, with the alloy staying in solid state. Compare to VLS, the growth rate is normally slower mainly due to the distinction of diffusion in liquid and solid state. Taking Ge/Au for example, we find that VSS is slower than VLS by about a factor of 10. But the advantage of VSS method is that it allows some kind of nanowires synthesized at a relative low temperature, which benefits materials with low melting point.

(4) Solution-liquid-solid

The so called SLS (solution-liquid-solid) mode discovered initially in mid-1990s, also has been suggested for a number of nanowire/catalyst systems [136-137]. Similar to the VLS reaction, during SLS growth, monomers generated by decomposition of molecular precursor react with the metal nanoseeds to form supersaturated alloy droplets [138]. The formation of nanowires from solution methods is relatively complicated. The process normally involves three steps: (1) crystalline seed formation; (2) crystal growth by aggregation of atoms to the seeds; and (3) surface stabilization by surfactants. SLS and VLS growth methods probably are equally capable of producing nanowires with narrow diameter distributions. SLS growth could afford mean diameter in the range of 4-10 nm, whereas VLS growth generally is responsible for mean diameters greater than 10 nm. SLS growth is not fit for high-quality oxide or nitride nanowires, but it can be used in most inorganic or organometallic laboratories, and also be easier to complement than VLS mode.

2.4.3 Physics for nanowire growth

For growth of nanowires, whether epitaxial or not, basic concepts of thermodynamics and kinetics are necessary to be involved. Crystal growth normally occurs in a range where there exists a chemical potential difference between precursors and the production to be grown. Furthermore during the growth, the chemical potential difference must be maintained by replenishing of vapor phase source, to keep providing a constant thermodynamic driving force:

$$\Delta\mu = \mu_v - \mu_s = \mathrm{RTln}(\mathrm{p}/\mathrm{p}_0) \qquad (2.2)$$

Where μ_v, μ_s refer to the chemical potentials of the vapor and substrate, respectively. p refers to the partial pressure of the component in the gas phase, and p_0 to the equilibrium partial pressure of that component over the crystalline material. This equation only concerns one component system, the situation will be much more complicated for binary and ternary systems. The partial pressures p and p_0 are replaced by concentrations when growing from a liquid phase.

The consideration in thermodynamics decides the potential for crystal growth, whereas the growth rate depends on kinetics, which is subdivided into three categories: Mass transport, surface effects and chemical reaction [139-141]. Mass transport describes the movement of material in the gas phase towards the growth interface, which is typically driven by difference in chemical potential. Surface

effects refer to the atomistic processes involved in nucleation, which may involve factors such as surface reconstruction, kink and dislocation formation, and usually include diffusion of material on the substrate. Finally, chemical reaction can be very complex, involving decomposition of precursors, gas phase reactions and heterogeneous reactions on substrate. In addition, the absorption and desorption of precursors are also very important. The growth rate for the chemical reaction is defined as the rate at which reactants are consumed with time, or at which production is grown. Take a simple reaction for example, mM + nN $\longrightarrow$ xX + yY, the rate is expressed as:

$$r = K(T)\,[M]^{m}\,[N]^{n} \qquad (2.3)$$

Where [W] and [N] refer to the concentration of W and N, respectively, concentrations are replaced by partial pressures when applied to a gas phase reaction. The coefficient k (T) refers to rate coefficient or rate and is defined by:

$$K = Ae^{-Ea/RT} \qquad (2.4)$$

Where E_a, the kinetic barrier which must be overcome for the reaction to proceed, and the prefactor A is an empirical factor which is usually temperature-independent. Therefore, chemical reactions limit crystal growth, the growth rate will follow this temperature dependence.

2.4.4 Preparation of InSb nanowires

Researchers have been studying and working on nanomaterials shaping in nanowires, nanodots, nanobelts or nanorods for decades. The developments in nanoscience and nanotechnology have brought a world of possibilities in a variety of industries and scientific endeavors. Recently, III–V semiconductors, such as GaN, GaAs, InAs, InP, and nitride nanowires have attracted much attention, because their novel properties make them a wide range of potential applications in nanoscale electronics and optoelectronics [142-151].

InSb has important application in high speed and low power devices, magnetic field sensors, mid or long wavelength detectors, etc. Recently, research on InSb nanowire has also attracted more and more attention, and lots of work on fabrication of InSb nanowire could be already found in literature. Among all fabrication techniques, chemical vapor deposition (CVD) is most widely used to synthesize nanowires. Using this method, a sealed quartz tube is normally adopted in a furnace to evaporate source material and deposit relative nanomaterial on substrates. The growth of InSb nanowires by using thermal CVD was firstly reported by Wang Zhongling et al [152]. With the assistance of Au nanoparticle, high quality and dense InSb nanowires were obtained on InSb (111) substrate. The diameters were found to be in a range of 80–200 nm. Using the same method, ultra small InSb nanowires with sub-10 nm diameter have been made by Rajat Kanti Paul et al. and Xunyu Yang et al [153-154]. In addition to the density and quality, another good virtue of CVD is capable of growing quite long nanowires, which is especially useful for further fabrication of devices. Referring to the disadvantage, the controllability in growth

direction or diameter has always been an issue for thermal CVD. However, controllable growth of nanowires has great significance for the practical application of this material in nanoelectronics. Alexander T Vogel et al. have realized certain controllability of growth of InSb nanowire by chemical beam epitaxy (CBE) [155]. For InSb nanowire growth, CBE usually runs at low pressure resulting in ballistic mass transport of the precursors from the sources to the substrate, which could minimize gas phase reactions. CBE could easily control the material fluxes due to the use of mass flow controllers. Another strong advantage is the pre-crack of the metal-organic precursors, which allows growth at much lower temperatures, adaptable for material like InSb with a melting point of 525 ^{o}C. By using laser interference lithography (LIL), the substrate was firstly pre-patterned with a regular arrangement of seed particles, and then InSb nanowires were synthesized by a CBE system. Following Figure 2.10 indicates a schematic diagram of the LIL-patterning and CBE process for the growth. A photoresist is first coated onto a substrate (a), and then partially exposed (b) and develop (c). After that, a thin layer of Ag was evaporated (d) and followed by lift-off (e). The final step was the growth process within the CBE system (f).

Figure 2.11 shows that the tilted SEM images of free standing InSb nanowires prepared by Alexander T Vogel et al., indicating certain controllability in the growth direction and diameter. However, the low growth temperature of 360 ^{o}C results in a high density of stacking faults in the wires.

Energy dispersiveX-ray (EDX) experiments indicated that an Ag content of about 14 at% inside the droplets for nanowires grown at 380 ◦C. All experiments

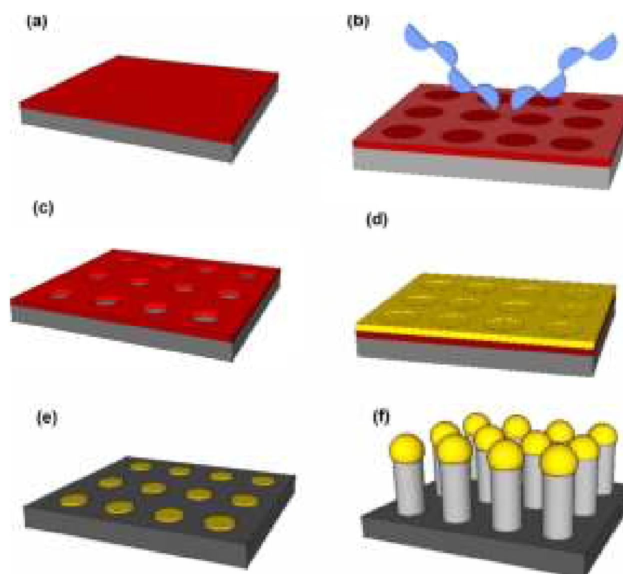

Figure 2. 10 Schematic diagram of the LIL-patterning and CBE process.

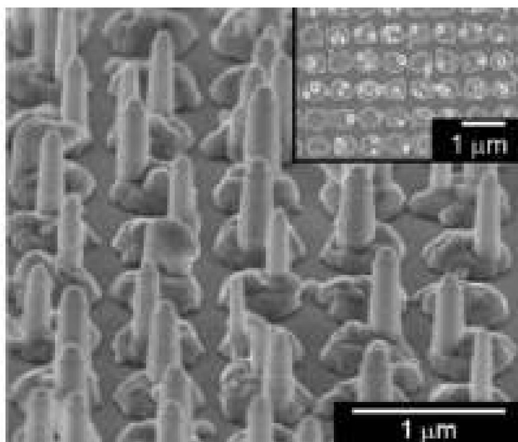

Figure 2.11 SEM micrographs of ordered InSb nanowire arrays grown on InAs (111)B with at 360 ^{o}C. Inset picture shows top view images of the corresponding sample.

consistently indicate that an In-rich alloy promotes InSb nanowire growth. According to the Ag–In phase diagram, at 380 ^{o}C about 27 at.% of Ag can be dissolved in liquid

In–Ag alloys. The seed particle is more likely to be liquid during the growth, and the InSb can be gown at the places where has In-Ag droplets, which leads to the formation of InSb nanowires by following the Vapor-liquid-solid process.

In the same way by using CBE, L Lugani et al. has reported growth of high quality InSb nanowire based on InAs to form a hetero-structure [156]. A diameter dependence of nanowire growth rate is demonstrated by them, suggesting that the InSb nanowire diameter and length could be controllable in certain degree.

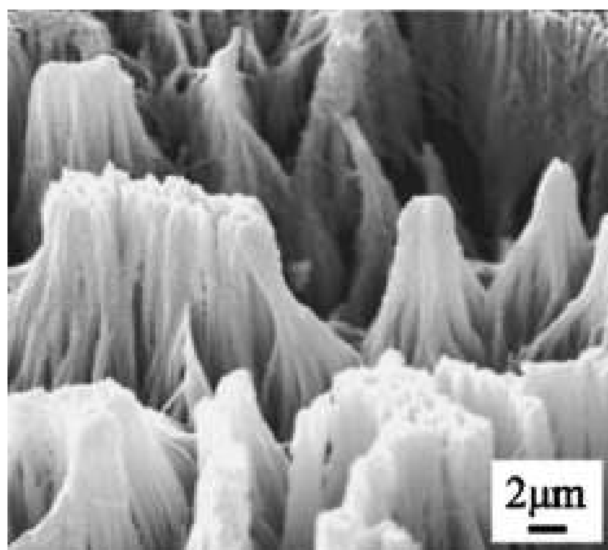

Figure 2.12 SEM images of InSb nanowires prepared by AAM.

As the achievement in controllability, anodic alumina membrane (AAM) is another normally used approach of preparing nanowires. AAM is capable of realizing uniform and parallel porous structures, which make them an ideal host for preparing ordered nanoarrays. Xueru Zhang et al. have reported the preparation of InSb nanowire arrays by AAM with the combination of electrical and chemical deposition.

Figure 2.12 gives the SEM image of the corresponding nanoarrays, which would have potential applications in infrared optical array nanodevices [157]. In addition, the diameter of nanowires could be modulated by changing the pore diameter of the AAM. Figure 2.13 shows the SEM images of InSb nanowires prepared by AAMs with different pore diameters by M. Ibrahim Khan et al [158]. Besides, achievement of better control of stoichiometry InSb nanowire here may be possible by modifying the growth parameters of electrodepoistion carefully.

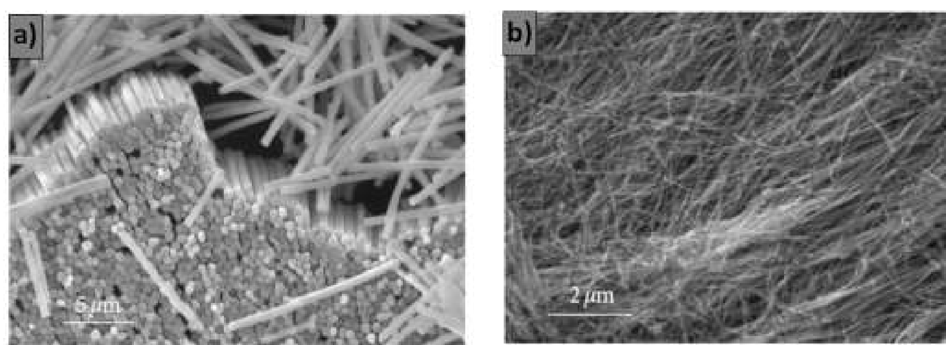

Figure 2.13 SEM of a bundle of aligned nanowires released from AAM with 200 nm pores, (b) SEM of a bundle of nanowires being removed from the template with 30 nm pores.

Metal-organic chemical vapor deposition (MOCVD) is another widely used technique to prepare III-V binary nanowires. It has many advantages like cost efficiency, high uniformity, large-scale commercial productivity. In addition, MOCVD has many important parameters, which could be carefully optimized for controllability of nanowire growth. To present, the InSb nanowires made by MOCVD are normally based on other materials like InP, InAs, GaAs, etc, by forming a heterostrucuture. Figure 2.14 indicates the SEM images of InSb nanowire based on

InAs, InP and GaAs, respectively [159-161]. This kind of growth of nanowire heterostructures is a success of integrating epitaxial nanoscale InSb, even at extreme lattice mismatches. However, the growth and study of single free standing InSb nanowire made by MOCVD is still lack in literature. Therefore, single InSb nanowire by MOCVD is one mission we are expecting to complete in this project.

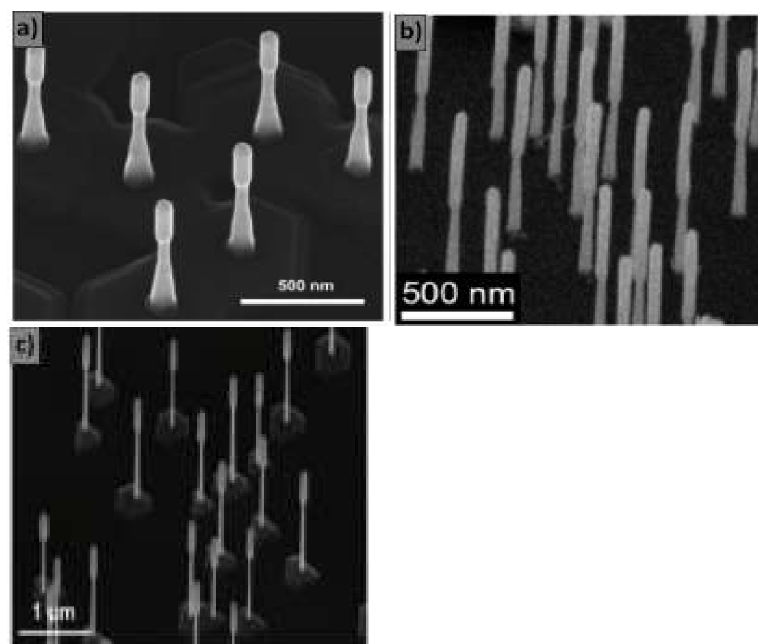

Figure 2.14 SEM illustrations of InAs/InSb (a), InP/InSb (b) and GaAs/InSb (c) nanowires.

2.4.5 Properties and application of InSb nanowire

For nanostructures, due to the reduction in size to nanoscale, surface and quantum confinement effects will become apparent, resulting in some interesting properties normally not observed in bulk. For InSb nanostructure, some interesting properties like maganetoresistance, a very large land´e g-factor, a strong Rashba effect, and a

high thermoelectric Figure of merit, have been theoretically predicted or experimentally observed.

Hongzhi Chen et al. have calculated the variation of band gap of InSb nanowire on diameter, which is indicated as in Figure 2.15 [162]. It was calculated by the following equation:

$$Eg_d = Eg_b + \frac{\hbar^2\pi^2}{2d^2}\left(\frac{1}{m_h^*} + \frac{1}{m_e^*}\right) - \frac{1.8q^2}{\varepsilon d} \qquad (2.5)$$

where ħ is the Planck constant, m_h^* and m_e^* are the effective masses of hole and electron, Eg_b is the bandgap of bulk material, Eg_d is the bandgap of the quantum confined material, and d is the diameter of the material. It is seen that with the diameter of the nanowire decreasing from 65 to 10 nm, the bandgap increases from 0.17 eV to 0.40 eV, covering the entire middle IR wavelength to near IR region. The bandgap has no obvisous change when the diameter of nanowire is above 65 nm, demonstrating a limit value of apprearance of quantum size effect.

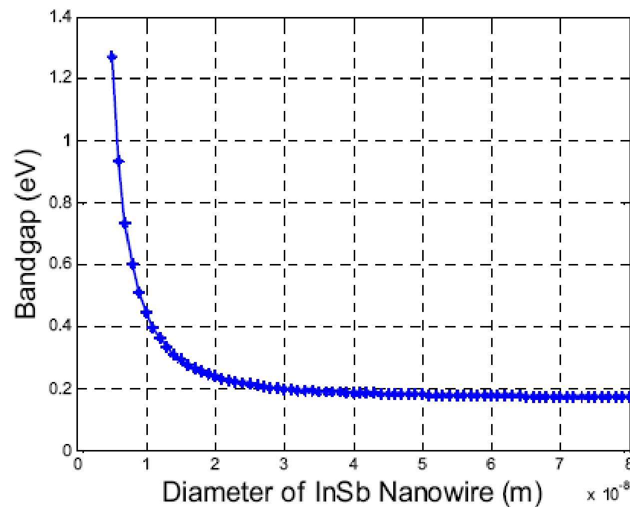

Figure 2.15 Relation of the diameters of InSb nanowire with the bandgap.

1. Transport property

Being negligible in bulk case, electron-electron correlation effects play the dominant role in one dimension (1D), which may result in the formation of the unusual state of the electronic subsystem called a Luttinger liquid. The important feature of the Luttinger liquid is a strong increase of power factor $S^2\sigma$ (where S is the thermopower and σ is the electrical conductivity) with enhancing temperature, which is promising for thermoelectric applications. Luttinger liquid behavior of the thermoelectric power has been revealed in InSb nanowires and carbonnanotubes. O.

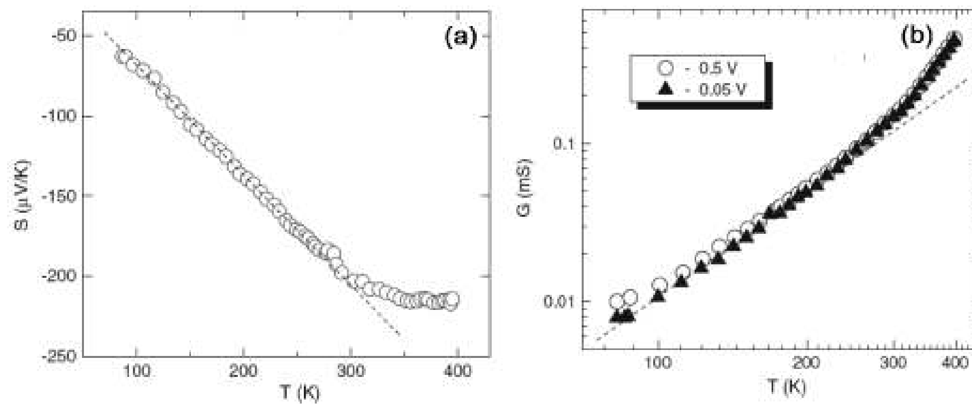

Figure 2.16 The temperature dependence of the thermoelectric power (a) and the differential conductance (b) of a bundle of InSb nanowires.

N. Uryupin et al. have measured the thermopower and electrical conductance of bundles of InSb nanowires over the temperature from 80 to 400 K [163]. Figure 2.16 a) and b) indicate the temperature dependence of thermoelectric power and the differential conductance of a bundle of InSb nanowires, respectively. It is shown that the conductance increases rapidly with increasing temperature, and the thermoelectric

power factor of the nanowires increases monotonically with temperature in this range. This property has important application on solid state thermoelectric (TE) devices for direct thermal-to-electric energy conversion and refrigeration with emission of greenhouse gases. The energy efficiency of TE devices relies on the TE Figure of merit (ZT), which could be expressed as $ZT = S^2\sigma T/\kappa$, where κ is the thermal conductivity. T is the absolute temperature.

2. Magnetoresistance

Magnetoresistance is the property of a material changing the value of its electrical resistance when an external magnetic field is applied to it. The observed magnetoresistance corresponds to a magnetic field induced variation of the exponents for $G(T) = G_0\,(T/\epsilon)^{\alpha(H)}$, and nolinear I-V curve $I(V) = I_0\,(V/V_0)^{\beta(H)}$. The exponents α, β are dependent on magnetic field, which may result from magnetic-field-induced breaking of the spin-charge separation. S. V. ZaitsevZotova et al. have studied the electrical conduction of long InSb nanowires in asbestos matrix as a function of magnetic field [164]. Figure 2.17 shows a typical variation of the electric current, I, measured at a set of fixed voltages, vs. magnetic field. It is seen that the conduction reaches a maximum at T ~1 T and falls down by a factor of 5 at H =10 T at given temperature, exhibiting a strong positive magnetoresistance effect.

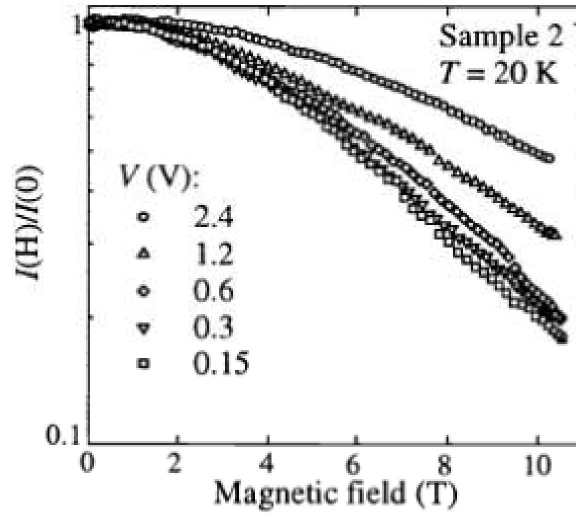

Figure 2.17 Typical set of electric currents vs. magnetic field curves measured at different voltages.

3. Large Land´e g-factor

The so-called Land´e g-factor thus describes deviations of experimentally observed magnetic moments from the classical case with $g = 1$ due to the effect of spin-orbit interaction. Nowadays, spintronics has received much of research in semiconductor physics due to its potential extensive applications. The g factors of energy levels in metal nanoparticles and semiconductor dots have been studied by several groups. In ultra small quantum dots defined in InAs nanowire heterostrucutre and Ge/Si core shell nanowires, a strong reduction in the effective electron or hole g factor toward 2 was observed [165-166]. It was found that the g factor was strongly reduced, from the bulk value of ~ 2 to value of ~ 0.3 in Au nanoparticles [167]. This reduction of g factor could be interpreted as a result of the quenching of the orbital

momentum in such small quantum structures. Via the magneto-transport measurements, Henrik A. Nilsson et al. have calculated the absolute values of giant g factors nearly to ~ 70, in InSb quantum dots with quantum levels [168]. Such giant, level-dependent effective *g* factors in the InSb quantum dots renders various spin physics phenomena, which is promising for the application in spintronic devices and spin-based quantum information processing and communication.

4. Rashba effect

Rashba effect is another quite important property of nanostrucutres. It is due to the Rashba spin orbit coupling caused by the structure inversion asymmetry, which can be introduced by an external electric field. People pay more attention to the Rashba spin orbit coupling in nanowires because of its abundance of interesting physical phenomena and application values like spin-based devices. One of the most important spin-based devices was proposed by Datta and Das, which is to make use of the Rashba spin-orbit coupling in order to perform controlled rotations of a field-effect transistor (FET) [169]. X. W. Zhang et al. have studied Rashba spin-orbit coupling brought by transverse electric field in InSb nanowires [170]. Figure 2.18 indicates the Rashba coefficients of InSb nanowires as functions of the external electric field and radius, respectively. It is seen that the Rashba coefficient is approximately a linear function of the external electric field (Figure 2.18 (a)), and shows a saturating trend in the large E_{ext} range at a larger radius of nanowire. The cause is due to the Stark effect which changes the state components, mixing the conduction-band states with the

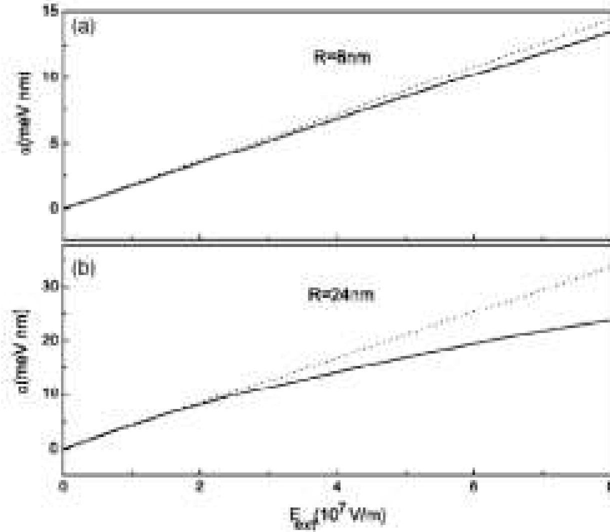

Figure 2.18 Rashba coefficients of InSb nanowires as functions of external electric field of at fixed radius of 8 nm (a) and 24 nm (b), respectively.

valence-band states. The tunable Rashba spin-orbit coupling brought by transverse electric field will strongly influence the longitudinal spin-dependent transport properties, which may help the design of devices like Datta-Das spin-FET and spin filter.

2.5 Experimental setup and methods

2.5.1 Metal-organic chemical vapor deposition

MOCVD is the most versatile thin film deposition technology for compound semiconductor materials by using metal-organic compounds as precursors. This growth technique was developed in 1960's. After many decades' development, it has been widely used as deposition process in both research and industrial manufacture.

In this project, a LP- MOCVD (AIX200 (#1499)) developed by AIXTRON Corporation is used as the growth system. The system is computer controlled and made up of three main parts: Vacuum and exhaust system, MOCVD reactor system, gas handling system. Figure 2.19 indicates a schematic diagram for the system.

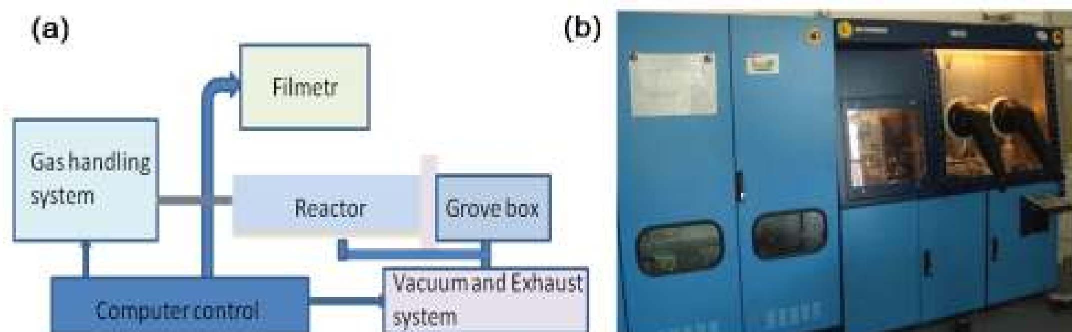

Figure 2.19 (a) The schematic diagram of MOCVD system and (b) the photograph of the system under the growth process.

The function of gas handling system is metering and mixing the gases that will enter the reactor. Timing and composition of the gas entering the reactor will determine the eplilayer structure. Exhaust system has two functions, one is controlling the growth pressure and the other is waste gas treatment by using mechanic pump and pressure controller. The overall growth process in the reactor is very complicated due to a complex interplay between gas phase and surface chemistry as well as hydrodynamics. Figure 2.20 shows the major growth procedures in the reactor by taking InSb layer growth as the example. During the growth, important parameters such as growth temperature, chamber pressure, the partial pressures of each source, etc, must be very carefully controlled and optimized in order to obtain the material grown with ideal quality and nice structure.

Figure 2.20 Schematic diagram of the growth process in the MOCVD reactor.

2.5.2 Characterization methods

(1) Photoluminescence spectroscopy (PL)

Photoluminescence spectroscopy is a contactless nondestructive method of probing the electronic structure of materials. When incident light source (usually a laser beam) is illuminated on the semiconductor crystal, electrons in the material will be excited to higher levels by absorbing the photon energy. The excited electron is unstable and will return to its ground state accompanied by releasing energy in the radiative or nonradiatvie way. Emission peaks will be detected in the radiative process and the emission spectrum contains "fingerprint"-type peaks indicating the

energy of each excited level and can be used as a sensitive probe to find impurities and other defects in semiconductors. In this project, the band gaps and defect states of $InSb_{1-x}N_x$ alloys will be collected by a home-made PL system and the set up is shown in Figure 2.21. During the measurement, the laser beam is focused onto the sample in the chamber. The chamber could be pumped to the vacuum by a mechanical pump when low temperature measurement is needed. Through a long pass 5 μm filter, the PL emission from the sample after laser excitation is directed into the monochrometer. After being decomposed by optical grating in the monochromator, the signal is detected by a thermo-electric cooled HCT detector. The output signals from the detector are amplified by a lock-in amplifier. Computer is used to monitor and control the PL measurement.

Figure 2.21 Schematic diagram of the PL system.

(2) X-ray diffraction (XRD)

X-ray diffraction is a standard approach for analyzing the crystal structure of materials. Crystal lattice is regular three-dimensional distribution of atoms in space. For any crystal, planes exist in a number of different orientations - each with its own specific *d*-spacing. When a monochromatic X-ray beam is projected on a material with an angle θ, diffraction peaks will be observed when the Bragg's law conditions are satisfied by wavelength λ, incident angles of θ, and d-spacings of the crystal planes. By using XRD, a wealth of structural and physical information about phase identity, lattice parameter, crystal quality, material composition, and superlattice structures, etc, can be obtained.

(3) Hall effect measurement

Electrical properties like carrier concentration, film resisitivity and mobility can be measured with aid of the Hall measurement system. The basic physical principle underlying the Hall effect is the Lorentz force. When a charged particle moves along a direction perpendicular to an applied magnetic field, it experiences a force acting normal to both instantaneous velocity and the magnetic field. In this project, the Van Der Pauw technique of four-point probe measurements will be used to investigate the electrical properties of $InSb_{1-x}N_x$ alloys.

(4) X-ray photoelectron spectroscopy (XPS)

XPS is a general surface chemical analysis technique due to its high surface sensitivity, combined with quantitative and chemical state analysis capab ilities. By using XPS, information about the elemental composition, chemical state

and electronic state of the elements in a material can be obtained. XPS can detect all the elements but hydrogen or helium.

(5) Energy-dispersive X-ray spectroscopy (EDX or EDS)

EDX is a normally used technique for elemental analysis or chemical characterization for the materials. Since each element has a unique atomic structure, the elemental content, percentage, etc. could be analyzed by investigating the interaction of X-ray and a sample. In our work, the EDX setup was appended to a SEM equipment (JSM-5600 LV).

(6) Atomic Force Microscopy (AFM)

AFM is another powerfull system in surface roughness and topography of substrates and deposited thin film. The information is gathered by "feeling" the surface with a mechanical prob made by piezoelectric elements, which facilitate tiny but accurate and precise movements, and thus enable the very precise scanning and demonstrated resolution on the order of fractions of a nanometer.

CHAPTER 3. EPITAXIAL GROWTH OF HIGH QUALITY INSB AND $INSB_{1-x}N_x$ ALLOYS BY MOCVD

3.1 Introduction

Metal-organic chemical vapor deposition (MOCVD) is an excellent way of preparing compound semiconductor materials. Till now, there has been only one report about growing $InSb_{1-x}N_x$ alloys by MOCVD and the x value is as high as 0.24 [171], and not much information is available for MOCVD on $InSb_{1-x}N_x$ alloys. Therefore, it is necessary to investigate the properties of $InSb_{1-x}N_x$ alloys grown by this technique. In this chapter, InSb was epitaxially grown on InSb substrate first in order to find an optimum growth condition for InSb. Based on that, nitrogen was then introduced to prepare $InSb_{1-x}N_x$ alloys.

3.2 InSb epilayers on InSb substrate

3.2.1 Experiment

The sample was grown in a horizontal low pressure MOCVD reactor (Aixtron, AIX200) with gas foil rotation of the susceptor. The MO sources used in the growth were trimethylgallium (TMSb), Dimethylhydrazine (DMHy), and trimethylindium (TMIn). Hydrogen gas was used as the carrier gas. The reactor pressure for the growth was set at 100 mbar. V/III source ratios and the substrate temperature were

optimized to achieve good film quality of InSb. After that, different N/(Sb+N) ratios were used aiming to modulate the N content in the film. InSb oriented in the (001) direction was used as the substrate for the growth. The surface morphologies of the epilayers were inspected by Scanning electron microscope (SEM). The XRD measurement provided the crystal quality of the epilayers grown. The optical and electrical properties of the epilayers have been characterized using photoluminescence spectroscopy and Hall measurement.

The low melting point of the III-V antimonide-based semiconductors limits the temperatures at which these materials can be grown by MOCVD. In particular for InSb, it melts at 525 ^{o}C and must be grown below this temperature. However, the Sb-source used in the growth TMSb does not decompose significantly until 500 ^{o}C [172]. For this consideration, our growth temperatures of $InSb_{1-x}N_x$ are chosen around 500 ^{o}C. The second consideration about growing the Sb-based compound semiconductors

Table 3.1 Growth parameters of the InSb films on InSb substrate.

Sample	**V/III ratio**	**Temp (^{o}C)**	**Pessure(mbar)**	**Time (min)**
S1	4.2	510	100	40
S2	4.2	500	100	40
S3	4.2	490	100	40

is about the low equilibrium antimony vapor pressure at the typical growth temperatures. A very high V/III ratio may lead to excessive antimony, which will result in a separate elemental antimony phase on the surface. However, Indium will also appear as a separate phase if the V/III ratio is too low [173]. Therefore, the V/III ratio must be well controlled in order to avoid antimony or indium condensation on the surface. InSb has been investigated for decades of years. Various techniques like MBE, and LPE have been used to prepare the material [174-176]. MOCVD is a popular technique remarkably advanced in growing high quality InSb and very high mobility has been obtained [177-179]. As we know, too high or too low V/III ratio

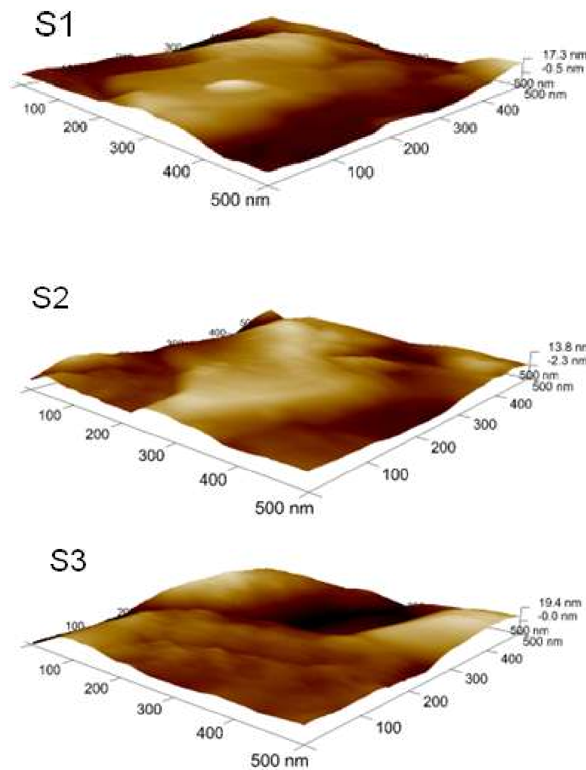

Figure 3.1 AFM images of the sample S1, S2 and S3

will result in condensation of antimony or indium, most part of the past work in relative to InSb growth suggested the optimum V/III ratio should be between 2 and 6. During our growth, the V/III was set at about 4.2 and the specifics about the growth parameter of epitaxial InSb on InSb (100) substrate are as shown in table 3.1. The growth pressure and time are 100 mbar and 40mins, respectively. Temperature is changed from 490 ^{o}C to 510 ^{o}C to seek the optimum point for the growth.

3.2.2 Characterization

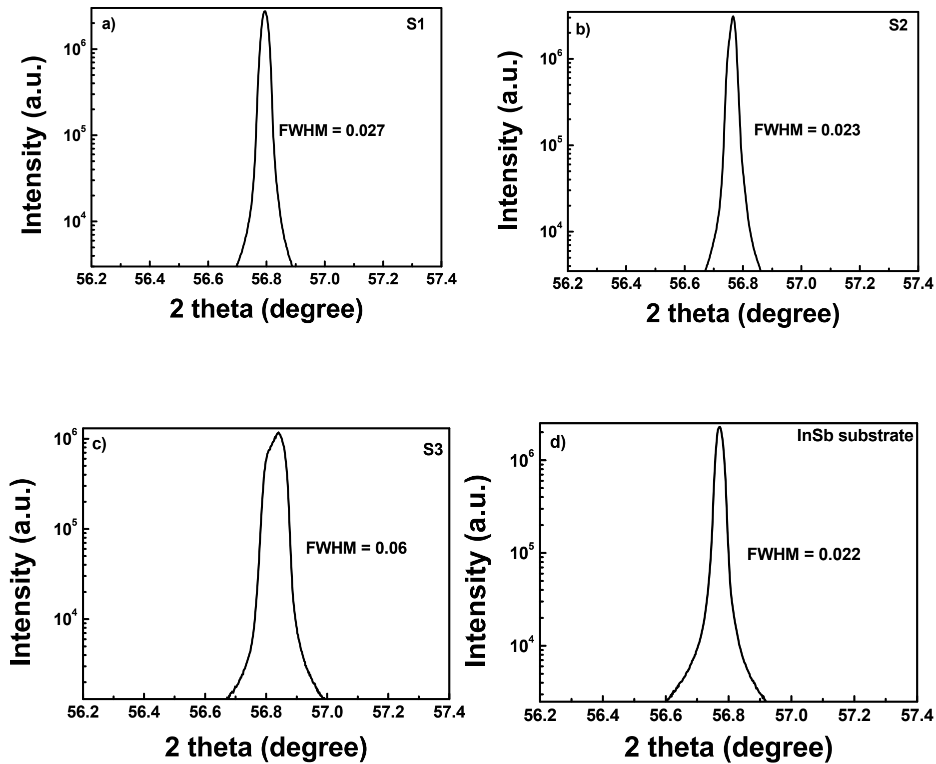

Figure 3.2 XRD spectra of samples: S1, S2, S3, InSb substrate. InSb substrate was measured for comparison.

As a result, we got a group of mirror-like samples from S1 to S3. The surface morphologies are indicated in Figure 3.1. It can be seen that the films have quite smooth surface. Figure 3.2 refers to the XRD results of the samples. The extremely strong peaks and narrow Full-Width Half-Maximum (FWHM) indicate that the films possess very high quality. Moreover, the FWHM values of S1 and S2 are very close to that of InSb substrate, which demonstrates the range from 500 ^{o}C to 510 ^{o}C seems to be an optimum growth window in term of temperature.

The band gap and defect states of the samples were investigated by a home-made PL system. The excitation source used in the system is one Nd: YAG laser with peak wavelength at 1.064 µm. A compressor with continuous helium flow is used to realize low temperatures (10 K and above). Through a long pass 5 µm filter, the PL emission from a sample is directed into the monochromator. After being decomposed by optical grating in the monochromator, the signal is then detected by a nitrogen cooled MCT detector and amplified by a lock-in amplifier. To assure the accuracy of the measured signal, the system was first calibrated by measuring the standard InSb wafer with knowing band gap before measuring the samples under test.

Figure 3.3 (a) shows the PL spectra of InSb substrate at various temperatures. It is seen that PL peak has a red shift with increasing the temperature and the peak position moves by approximately 1.6 µm as the temperature is varied from 10 to 300 K. The calculated band gap energy of the substrate at 10 K is about 0.235 eV, which is just the same as the theoretical value. Figure 3.3 (b) indicates the fitting curve which is fitted by Varshni equation [180]:

$$E_g = E_0 - \alpha T^2/(\beta + T) \quad (3.1)$$

Where E_g is the energy gap, E_0 is its energy gap at 0 K, and α and β are two empirical constants, which are 0.25 and 170 here, respectively.

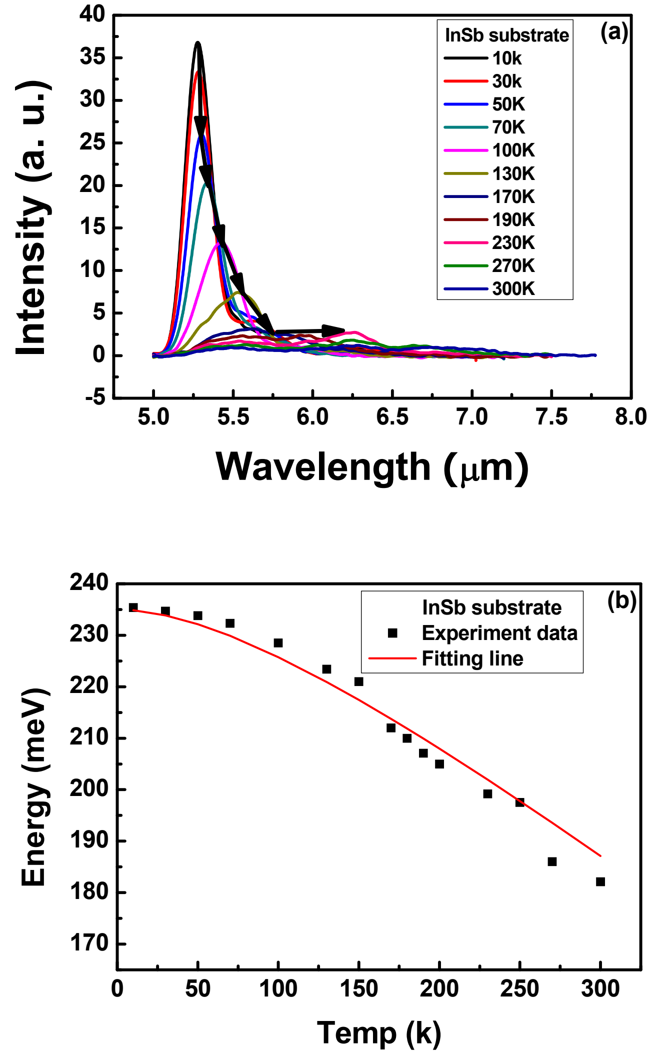

Figure 3.3 PL spectrum of InSb substrate at various temperatures. The peak positions shifts to longer wavelength with increasing temperature as indicated by the black allows. (b) The fitting curve by Vanshni equation.

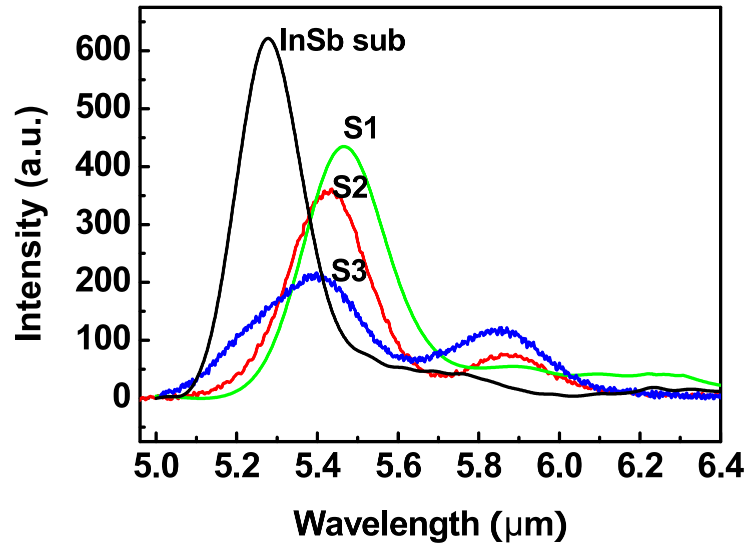

Figure 3.4 PL spectra of samples S1, S2 and S3 measured at 10 K.

Figure 3.4 depicts the PL spectra of samples S1, S2 and S3 measured at 10 K. For an easy comparison, the PL spectrum of the InSb substrate was included as a reference. From the PL spectra, it can be seen that one peak around 5. 28 μm (0.235eV) exists in the line of InSb substrate, which matches well with the reported band gap value for InSb. However, different from that of the InSb substrate, there are two PL peaks which are at about 5.4 μm (0.230 eV) and 5.87 μm (0.211 eV) in all InSb epilayers. The peaks at 0.235 eV of InSb substrate and 0.230 eV of deposited films should be assigned to band-to-band transition, even though there is a small energy discrepancy between them. For the low energy emission peak in the InSb epilayers, previous reports suggested either defect related emission or optical phonon-assisted band-edge emission [181-182]. The reason for attributing this peak to phonon-assisted emission by previous report is that the energy separation between this peak and the intrinsic emission peak is close to the calculated optical phonon energy in InSb [183]. There are several reports on the defect related emission with

energies at 0.230, 0.228, 0.225 and 0.224 eV [184-186]. In order to further clarify the origin of this emission, PL measurement over a wide temperature range from 10 to

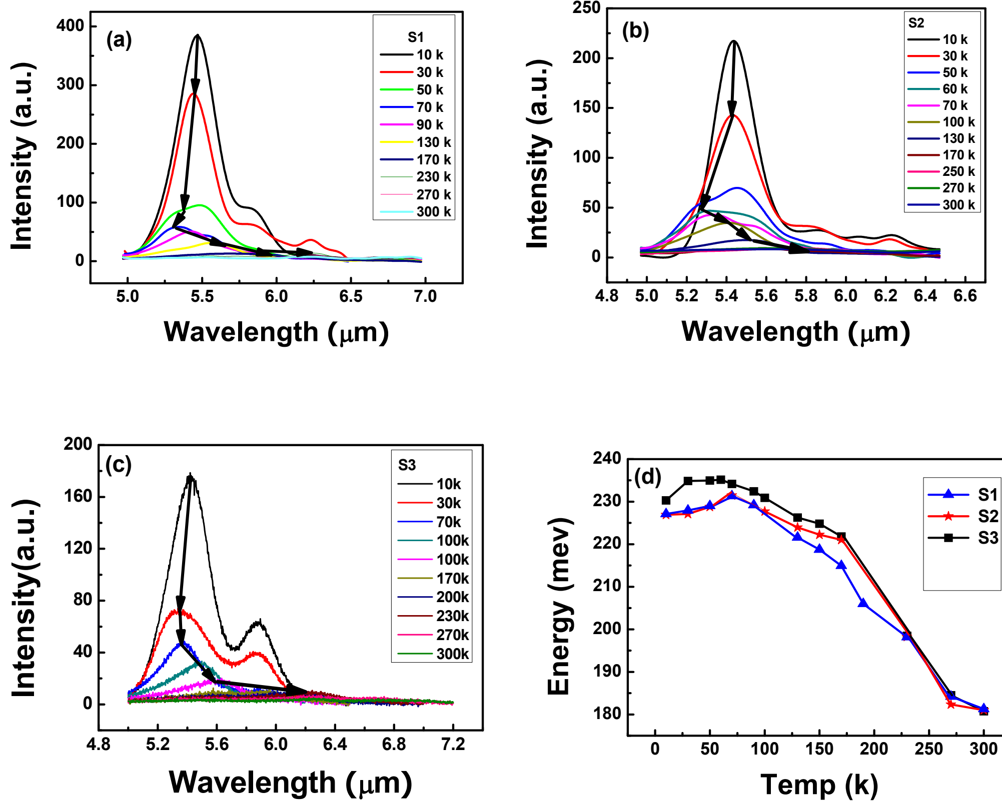

Figure 3.5 (a), (b), (c) indicate the PL spectra of S1, S2 and S3 measured at various temperatures, respectively. The main emission peak has a blue shift first and then a red shift with enhancing the temperature as indicated by the arrows. (d) Summarized band energy values from 10 to 300 K of the samples.

300 K was carried out. Figure 3.5 (a), (b) and (c) show the temperature dependence of PL spectrum of S1, S2 and S3, respectively. Compare to the PL of InSb substrate, a

very different but interesting phenomenon is found in our samples. It is seen that the

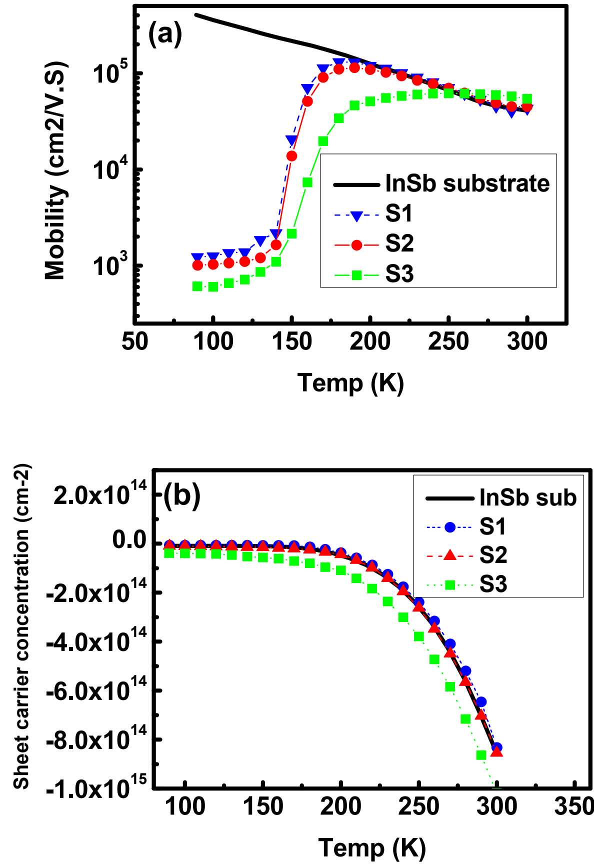

Figure 3.6 Temperature dependence of mobility (a) and surface carrier concentration (b) The data of InSb substrate was included as reference.

main emission peak has a blue shift first and then a red shift when the temperature increases from 10 to 300 K. This could be explained by the existence of the localization of excitons in the epilayer at low temperatures, as suggested by Chen et al. [187] However, for the peak at 0.211 eV, the position remains basically unchanged with the increased temperature, as indicated by the arrow in the Figure. These results indicate that the low energy peak is very likely originated from defects.

To identify the emission at 0.211 eV of our InSb sample in this study, we first studied the electrical properties of the samples by temperature dependent Hall measurement. The InSb substrate was also measured for reference. The magnetic field adopted for the measurement is 1 T. The mobility and carrier concentration of

Table 3.2 Values of mobility and carrier concentration of the samples grown at different substrate temperatures.

Sample (Growth temp)	Mobility (cm^2/v.s)	Surface carrier concentration (cm^{-2})
InSb substrate	300 K. 4.1×10^4 90 K. 4.04×10^5	300 K. 8.58×10^{14} 90 K. 8.46×10^{12}
S1 (510 ^{o}C)	300 K. 4.5×10^4 180 K. 1.14×10^5 90 K. 1.0×10^3	300 K. 8.6×10^{14} 90 K. 9.5×10^{12}
S2 (500 ^{o}C)	300 K. 4.3×10^4 190 K. 1.31×10^5 90 K. 1.2×10^3	300 K. 8.33×10^{14} 90 K. 6.3×10^{12}
S3 (490 ^{o}C)	300 K. 5.4×10^4 240 K. 6.1×10^4 90 K. 6.0×10^3	300 K. 1.02×10^{15} 90 K. 3.9×10^{13}

the samples with the temperature changed from 90 to 300 K are shown in Figure 3.6 (a) and (b), respectively, and the quantitative data is collected in table 3.2 at room temperature. It should be admitted that the carrier concentration and mobility obtained from the measurement should have a small deviation from the actual values of the samples due to the conductivity of InSb substrate. Luckily these values are used for some qualitative analysis, or explaination for the trend of mobility verifying with temperature. The mobilities of all samples are ~ 4 x 10^4 cm^2/V s, indicating high quality of the epilayers. According to Matthiessen's rule, the mobility is mainly limited by lattice scattering under room temperature, which may explain the fluctuating phenomenon of the mobility. The mobility reaches a maximum point at about 160 k depending on different samples. K. D. Chaudhuri, etal suggested that in the low-temperature region, other than from optical phonon scattering (OPS), deformation potential scattering (DPS), the defect-band conduction significantly contributed to the mobility [188]. It is found that the defect-band conduction increases with decreasing the temperature, resulting in mobility decreasing dramatically in the low temperature region. According to previous reports, InSb will reach a maximal point near 70 K, being limited by ionized impurity scattering at the intermediate temperatures [189]. The maximum couldn't be observed because the lowest point in our measurement is 90 K. However, a maximal point could be observed in all deposited samples grown by MOCVD.

3.2.3 Antisite defect Sb_{In}

When the temperature is reduced, the mobility of the samples increases first and then decreases. For the InSb substrate, however, the mobility monotonically increases with the temperature to a very higher value. At low temperature, ionized impurity

scattering is dominant, which means the films deposited by MOCVD contain more defects in comparison to InSb substrate. From the data in table 3.2, we can see that the temperatures of the highest mobility for S1, S2 and S3 are 180, 190 and 240 K, respectively. It means that S3 should have the highest defect concentration of among the three samples, indicating that the relative low growth temperature will produce more defects in the layers. Figure 3.6 (b) shows the sheet carrier concentration as a function of temperature for the three samples. It is seen that all the samples are n-type and that the electron concentration of S3 is the highest among them. The unintentional n-type doping of the epilayers and the results shown above suggests that the emission at 0.211 eV is due to the transition of electronson D^- centre to the valence band. In general, the native defects in epitaxial InSb layers are Sb vacancies (V_{Sb}), In vacancies (V_{In}), Sb interstitials (Sb_i), In interstitials (In_i), Sb antisites (Sb_{In}) and In antisites (In_{Sb}). Figure 3.7 indicates the formation energy of the native point

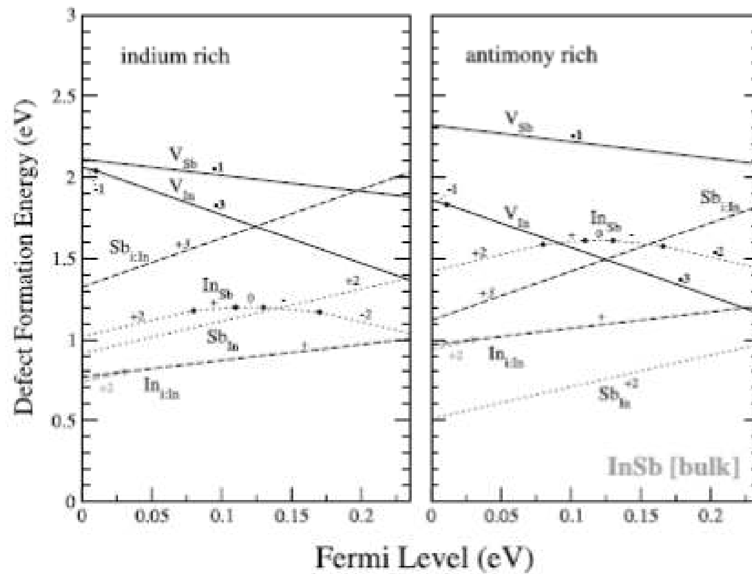

Figure 3.7 Formation energy of the native point defects in bulk InSb as a function of the Fermi level under In rich and Sb rich conditions.

defects in bulk InSb as a function of the Fermi level under In rich and Sb rich conditions [190]. It is seen that under Sb conditions, Sb_{In} has the lowest defect formation energy and is positively +2 charged in the bulk, and would work as donors by providing electrons. In our case, the V/III ratios we set during the growth were from 2 to 6, which provided a Sb rich growth environment in the chamber. As a result, some In sites in the InSb lattice will be taken up by the extra Sb atoms during the growth, leading to the formation of Sb_{In} defects and n-type conduction. The emission at 0.211 eV should be corresponding to the Sb_{In} defects. In order to further confirm the above conclusion, we did the growths by changing the V/III ratio. Samples S3–S5 were grown at 490 ^{o}C with the V/III ratios of S3, S4 and S5 set at 4.2, 6.2 and2.2, respectively. Table 3.3 indicates the growth parameters of the group of samples. Figure 3.8 shows the PL spectra of this group of samples measured at 10 K. Similar to the first group of samples, two peaks are observed from all the samples.

Table 3.3 InSb films deposited at different V/III ratio with same temperature.

The sample grown at the smallest V/III ratio has the biggest band-to-band emission peak but the smallest defect emission. The ratios between the intensity of the main peak (I_M) and that of the defect emission (II) are 1.8, 1.7 and 16.2 for

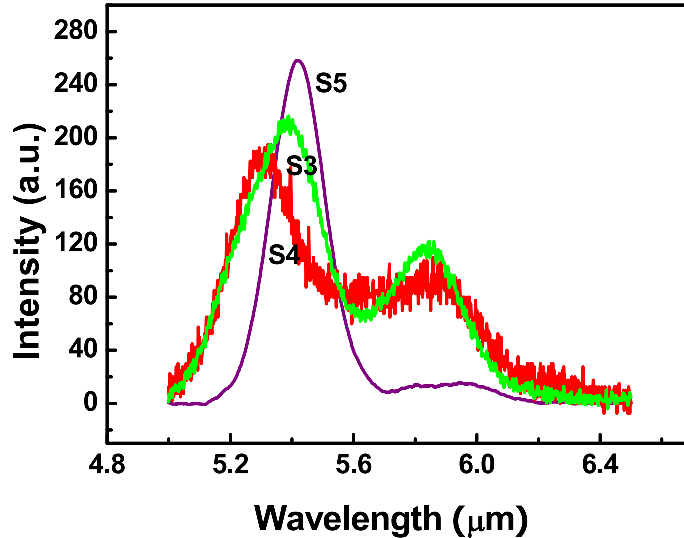

Figure 3.8 PL spectra of the samples dependent on V/III ratio at 490 ^{o}C, measured at 10 K.

sample S3, S4 and S5, respectively. It can be seen that the InSb layers grown with the higher V/III ratio received the higher defect emission as more Sb_{In} defects can be generated in this case. These observations confirm Sb_{In} defects being the origin of the emission at 0.211eV.

3.3 $InSb_{1-x}N_x$ alloys on InSb substrate

InSbN alloy has attracted a great attention recently for its exploitation in long wavelength detection [7, 13, 107]. By adding nitrogen into the alloy, the cut-off

wavelength of InSb could be extended to longer wavelength due to the negative band gap bowing effect, which makes InSbN alloy another new extraordinary candidate for the long wavelength detectors.

3.3.1 Growth details

Based on the growth of pure InSb by MOCVD, $InSb_{1-x}N_x$ alloys were continuously made by introducing nitrogen into InSb. Dimethylhydrazine (DMHy) is used as N source. Different growth temperatures and N/(Sb+N) ratios are aiming to modulate the N content in the film. InSb (001) was still used as the substrate for the growth.

Table 3.4 V- III ratio, N-V ratio, growth temperature, pressure and time of $InSb_{1-x}N_x$ alloys growth.

Sample	V/III ratio (Sb+N/)In	V/III ratio N/(N+Sb)	Pressure (mbar)	Temp (°C)	Time (min)
R1160	59.78	0.93	100	490	40
R1166	59.78	0.93	100	505	40
R1167	59.78	0.93	100	500	40
R1168	59.78	0.93	100	510	40
R1173	59.78	0.93	100	503	40
R1176	60.21	0.95	100	505	40
R1178	56.7	0.88	100	505	40

Table 3.4 shows the details about growth parameters of $InSb_{1-x}N_x$ alloys on InSb substrate. Samples R1160- R1173 were processed at a temperature range of between 490- 510 ^oC with (Sb+N)/In and N/(Sb+N) ratio at 59.786 and 0.93, respectively. Sample R1166, R1176 and R1178 were deposited at different V/III and N/V ratios but under the same temperature. These different experimental parameters were set to optimize the growth for achieving good film quality and for studying their effects on the N content in the film.

3.3.2 Characterization and measurement

Almost all of the $InSb_{1-x}N_x$ epilayers obtained on InSb substrate were smooth and shiny. Several samples were selected for the SEM measurement and the images are as shown in Figure 3.9. It can be seen that the samples have smooth surface but some small slits on them. The sample R1160 grown at 490 ^oC shows fewer defects than the other samples deposited at 505 ^oC. For InSb, the optimal growth window of temperature is quite narrow. Growth at a relative high temperature may bring damage to the film quality, due to the low melting point 525 ^oC of InSb. Besides, growth at 505 ^oC may lead to higher N incorporation than that at 490 ^oC, which is also probably the origin of the defects.

Figure 3.10 refers to the XRD results of the samples grown at different growth temperatures. InSb substrate has been measured as a reference and the FWHM is ~0.022 degree, which is the indication of the quality of the InSb substrate used. Except for the main diffraction peak of InSb substrate, the peaks originated from

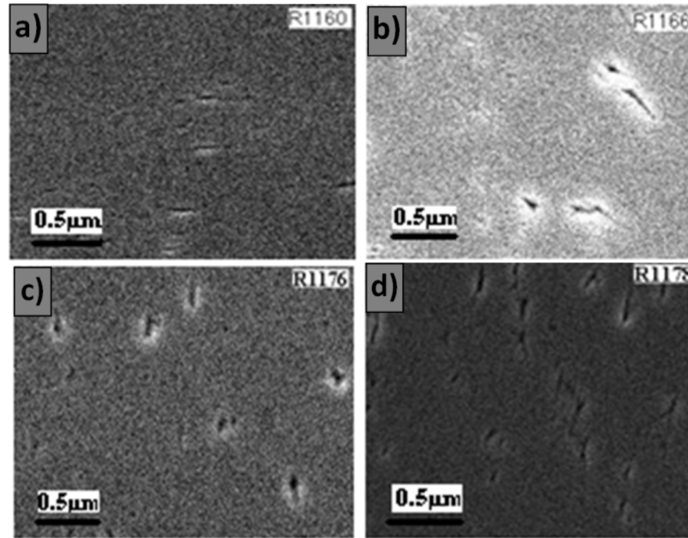

Figure 3.9 SEM photographs of (a) R1160, (b) R1166, (c) R1176 and (d) R1178 surface.

epilayers are also observed in many samples, which demonstrate that nitrogen has been successfully incorporated into the InSb. The lattice mismatch reaches to a maximum value for the sample grown at 505 ^{o}C. According to the Vegard' law, $a_{ABC} = xa_{AB} + (1 - x)a_{Ac}$, we have made a rough estimation of the nitrogen content in the epilayers and Figure 3.11 shows the nitrogen content changes with the growth temperature. We can see that the nitrogen content increases first and then decreases with raising the growth temperature. At low temperature, it may not provide enough energy for the N incorporation, but desorption of N may happen to the growth during the deposition. Therefore, too high or too low growth temperature is not appropriate for the N incorporation for the MOCVD grown InSb.

The variation of the nitrogen content in the grown InSbN films with input source ratio was also investigated, which is shown in Figure 3.12. It shows that the lattice

mismatch is the highest at a value of 0.93 in terms of the gas flow ratio, referring to the sample R1166. It is seen that the N content increases with increasing the N/(Sb+N)

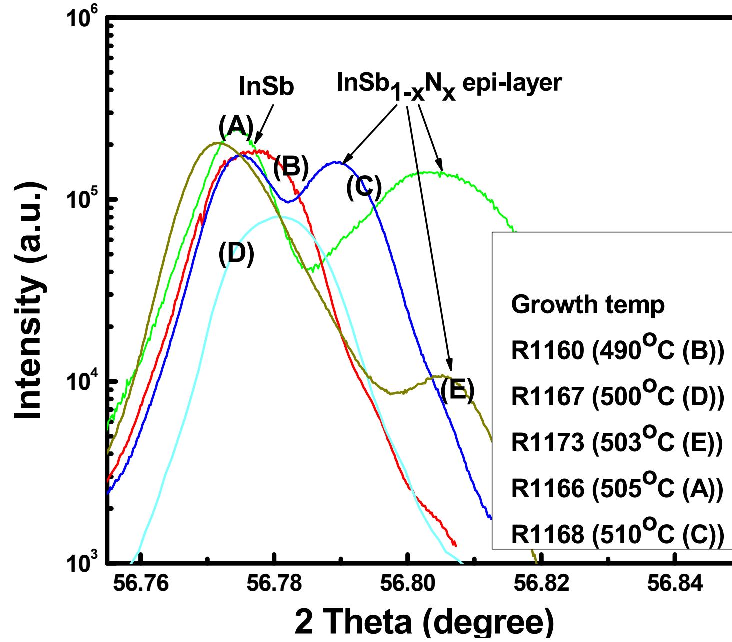

Figure 3.10 XRD spectra of the films grown at different temperature with same (N+Sb)/N and N/(Sb+N) ratios.

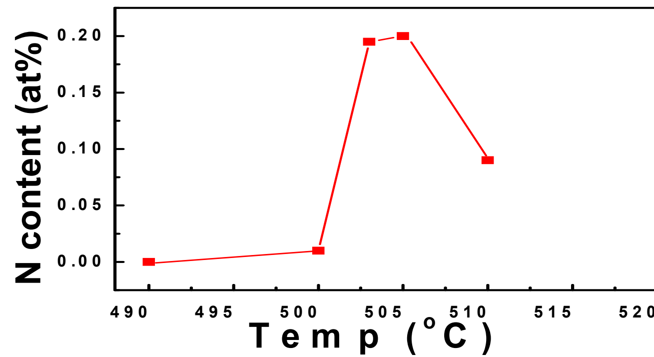

Figure 3.11 Growth temperature dependence of N content in $InSb_{1-x}N_x$ epilayer.

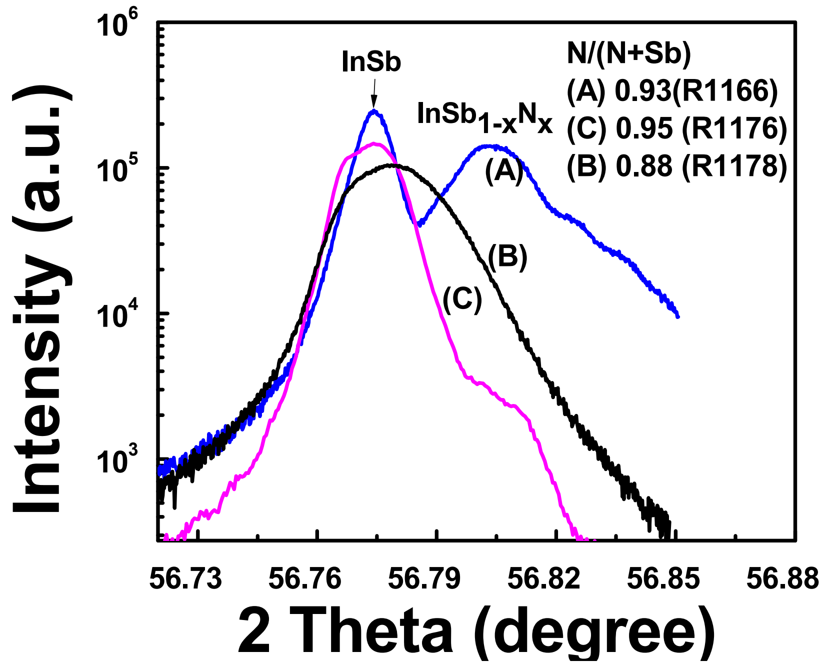

Figure 3.12 XRD results (004) of the InSbN alloys at different N/(N+Sb) ratio, R1166 (0.93), R1176 (0.95) and R1178 (0.88), at a fixed growth temperature of 505 °C.

ratio from 0.88 to 0.93, which we think it should be due to the increase of the N source during the growth. However the N content stops increase with increasing the N/(Sb+N) ratio further to 0.95.

It is generally known that adding nitrogen into InSb will lead to an effect of negative band-gap bowing. To see this effect, photoluminescence measurement (PL) on the samples has been done at low temperature. Figure 3.13 gives the PL spectrum of the samples grown at different temperatures and with different N/(Sb+N) ratios,

respectively. The measurement temperature was 10 K. Two obvious peaks are observed in all the samples. The main peak at the wavelength of 5.4 μm (0.230 eV) should be assigned to the band-to-band transition of the InSbN films and the one at around 5.87 μm (0.211 eV) is attributed to defect related emission from the samples.

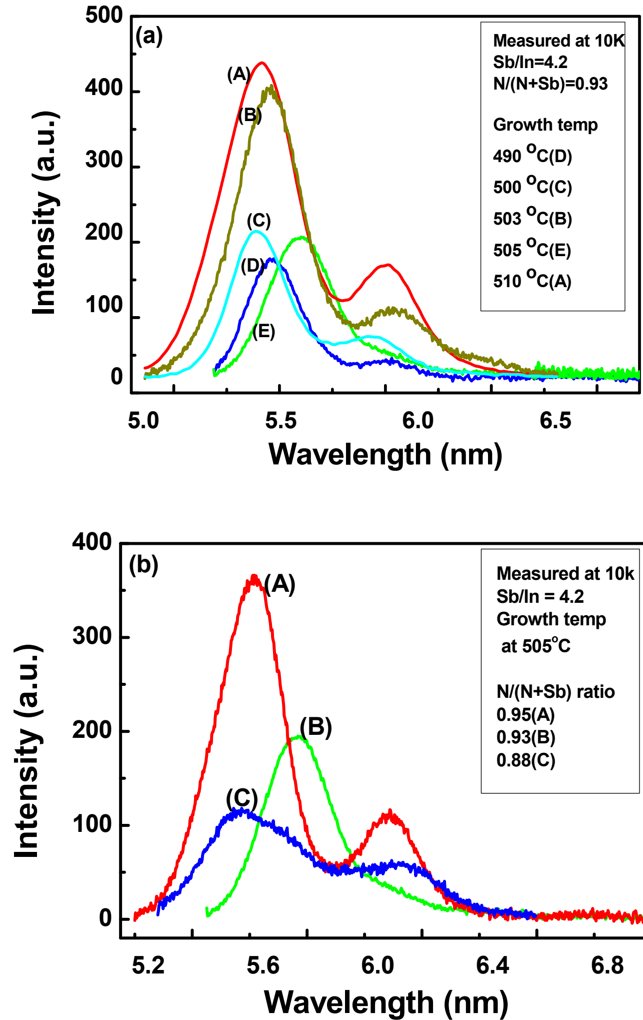

Figure 3.13 PL spectra of alloys with (a) different growth temperature and (b) different N/(N+Sb) ratios, respectively.

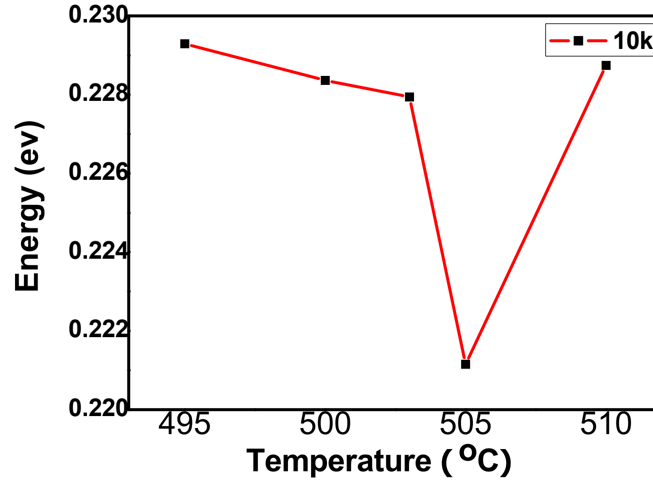

Figure 3.14 Band gap energy changes with the growth temperature.

Figure 3.14 indicates the film's band gap energy changing with the growth temperature. We can see that the band gap reaches the minimum value of the sample grown at 505 ^{o}C with the N/(N+Sb) ratio of 0.93. The band-to-band transition PL wavelength of this sample is about 5.6 μm (0.221 eV), a nearly 200 nm red shift of the InSbN film compared to that of the other samples. This indicates that a reduction of band gap has been realized likely due to the N content in the alloy. To see the temperature dependence of band gap, PL measurement over 10 K to room temperature was further carried out, and the spectra is shown as Figure 3.15. It is seen that with increasing the measurement temperature, the emission peak moves to higher energy first, and then turns the direction to lower energy at 60 K. This has been explained by the competition between the recombination of localized exciton to

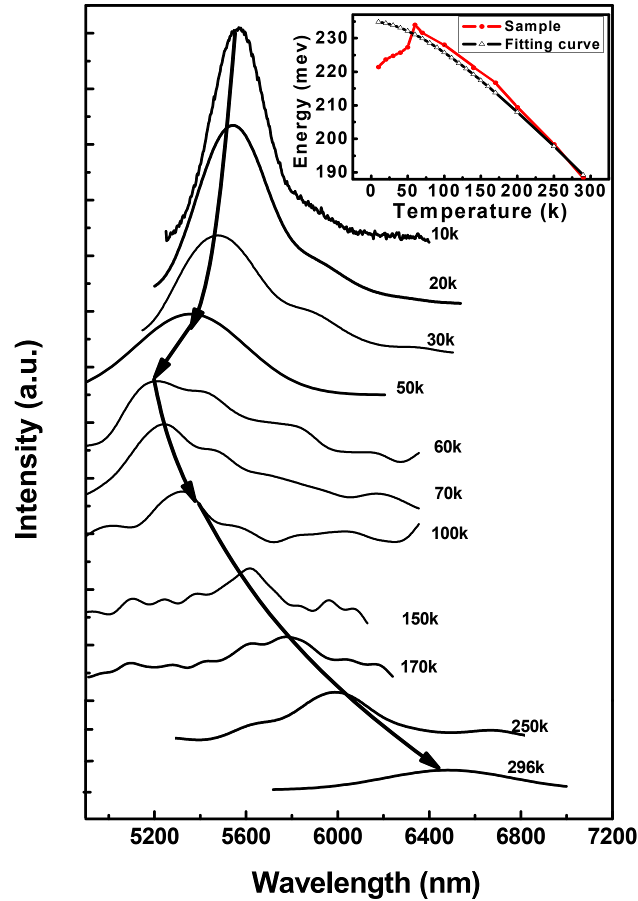

Figure 3.15 PL spectra of the sample R1166 at a wide temperature range from 10 K to 296 K.

conduction band and the lattice dilation due to the temperature elevation [187]. The inset Figure is about the calculated band gap energy at different temperatures, it can be seen the curve is well matched with the fitting line by Varshni equation above 60 K.

3.3.3 Behavior of nitrogen in the epilayers

The XRD result has demonstrated that the sample grown at 505°C with the N/(N+Sb) ratio of 0.93 has the highest N content. According to calculation result by

using a ten-band k.p model, the band gap reduction of the sample corresponds to an N content of 0.07% in the InSbN epilayer. However, according to the Vegard's law, an N content of 0.07% would cause a lattice mismatch ($\Delta a/a_0$) of the eiplayer to the InSb substrate only about -1.2×10^{-4}, which is smaller than the value of -4.3×10^{-4} observed from the XRD measurement. To get information about bonding configuration of N, this sample was measured by X-ray photoelectron spectroscopy (XPS). Figure 3.16 indicates the N1s XPS spectrum of the sample and the deconvolution of the spectra of different N componets. Four types of nitrogen bonds are indicated, they are

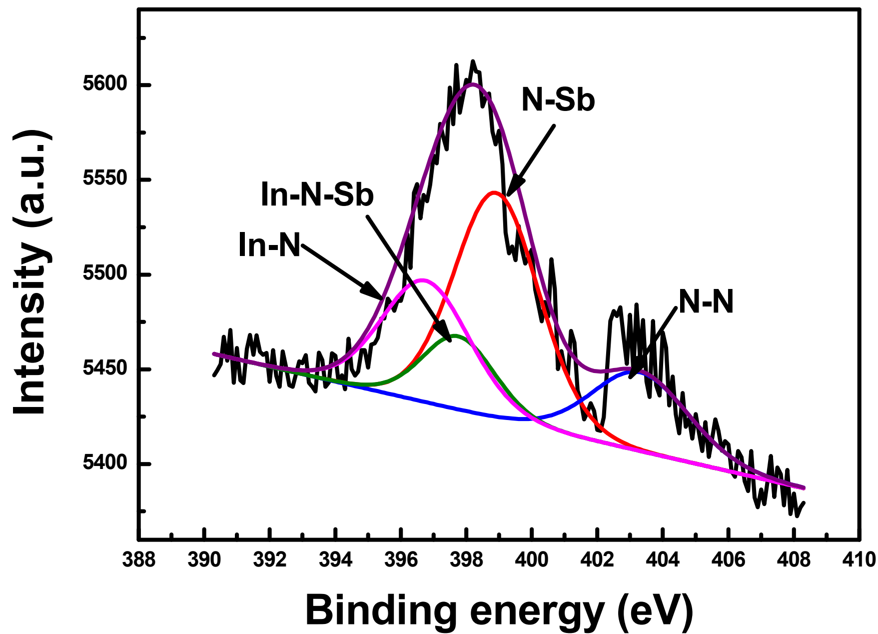

Figure 3.16 XPS spectra of the alloy grown at 505 ^{o}C with N/(Sb+N) ratio of 0.93, referring to the sample R1166.

substitutional N bonded to In (In-N) at a binding energy of (396.5 eV), interstitial N bonded to both In, N (In-N-Sb) at 397.9 eV and antisite N bonded to Sb (Sb-N) at 399 eV [1], and the molecular N_2 (N-N) at 403.6 eV [191]. According to the area covered by each N bonding peak over the total spectrum, the contributions of the four types of N bonds are 27% (In-N), 13% (In-N-Sb), 46% (Sb-N) and 14% (N-N), respectively. Therefore, the actual N content of Sample R1166 is 0.26% in total, which is a little bit bigger than the value estimated by the Vegard' s law. The XPS spectrum shows the most part of N locates at the position of antisite by forming the N-Sb bond, which is different from the samples grown by MBE or direct N implantation. Antisite defects in a single crystal would also contribute to the lattice mismatch. Therefore, in the lattice mismatch calculation here, antisite defects of the epilayer have been included. Using the model suggested by Chen et.al [192], the lattice mismatch due to the substitutional and antisite defects of the sample is given by following equation:

$$\frac{\Delta a}{a} = \frac{C_{11} + 2C_{12}}{C_{11}} \sum_i \frac{d_i - d_0}{d_0} \times \frac{[N_i]}{N_0} \tag{3.1}$$

Where C_{11} and C_{12} are the stiffness coefficients of the crystals, C_{11} = 6.67, C_{12} = 3.65 ($x10^{11}$dyn/cm^2), r_{Sb} (1.4 Å), r_N (0.75 Å) and r_{In} (1.44 Å) are the covalent radii of the antimony, nitrogen and indium, respectively. d_0 is the nearest distance between In and Sb atoms. $d_i = r_{In} + r_N$ and $r_{Sb} + r_N$, corresponding to the substitional and antisite defect, respectively. N_i and N_0 are the densities of point defects and the matrix atoms, respectively. Single In-N-Sb interstitials do not have obvious effects on the lattice parameters because r_N is much smaller than r_{In} and r_{Sb}. But for N-N defects, the interstitial couples will lead to splitting in the [100], [110] and [111] directions. d_i in each direction could be expressed by:

$$d_i^{100} = 1/\sqrt{3}r_{effect} + \sqrt{(r_{effect} + r_{In})^2 - 2/3r_{effect}^2}$$
$$d_i^{110} = \sqrt{2}/\sqrt{3}r_{effect} + \sqrt{(r_{effect} + r_{In})^2 - 2/3(r_{effect}/\sqrt{2})^2} \qquad (3.2)$$
$$d_i^{111} = 2r_{effect} + r_{In}$$

Where $r_{effect} = (r_N + r_N)/2$ for interstitial N-N. Figure 3.17 shows the lattice strains caused by different point defects in the film. It can be seen that the substitutional In-N, antisite Sb-N and interstitial N-N ([100], [110]) lead to lattice contraction, while the interstitial N-N [111] leads to lattice expansion. From the results of PL and XPS, we can get that the concentrations of different N defect forms in the alloy are 0.07% (In-N), 0.034% (In-N-Sb), 0.12% (Sb-N) and 0.036% (N-N), respectively. According to equation (1), the lattice mismatches ($\Delta a/a_0$) due to the substitutional In-N, antisite Sb-N, interstitial and molecular N is approximately -4.9×10^{-4} in total, which is very close to the XRD result -4.5×10^{-4}.

Only substitutional N-In bonding will lead to the band-gap reduction effect. However, nearly 50 % of the total N incorporated to InSb is occupied by the non-substitutional Sb-N bonding, while N-In bonding only takes up a small percentage. The reason for this is supposed to be due to the formation energies of various N defects. Till now, theoretical studies about defect formation energy of InSbN alloy are not available. Nevertheless, the formation energy of the native point defects in bulk InSb studied by A. Höglund et al. indicated that Sb_{In} has the lowest defect formation energy, which means In sites could be easily taken up by additional Sb atoms [190]. Hence, we here speculate that the defect N_{In} should probably have the lowest formation energy among all N forms in InSb. N atom would preferably occupy at In

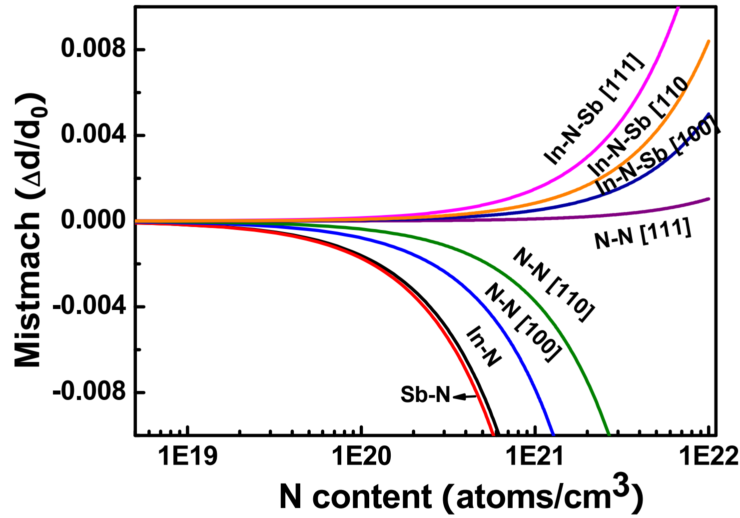

Figure 3.17 Lattice strains $\Delta a/a_0$ of InSb caused by different N point defects with the densities of N content.

sites and fraction can also be found by forming other N bondings. For this point, it needs to be confirmed by further theoretical studies.

3.4 Summary

InSb epilayers have been successfully prepared by MOCVD. PL measurement shows that in addition to the main band-to-band emission around 5.4 μm, an emission peaked at around 5.87 μm was detected. From both the electrical and optical properties of the InSb epilayers, this emission is attributed to the defect related emission resulting from the antisite Sb_{In} defects which can be eliminated by reducing the V/III flux ratio. InSbN films have been prepared by adding N. PL spectroscopy demonstrated that the band gap of the InSbN alloy has been extended to longer wavelength by N incorporation. For the alloy grown at 505°C with the N/(N+Sb) ratio of 0.93, the substitutional N_{Sb} measured by PL is estimated to be around 0.07%. The

band gap information was also investigated by photocurrent measurement, which has been made compared to the PL results. XPS spectroscopy shows that antisite (N_{In}) is the dominant N form in the alloy. Substitutional N_{Sb} occupies only a small part of the total incorporation. Other N forms like interstitial N and molecular N_2 (N-N) also exist in the alloy. Therefore, further work needs to be done to improve the active part of the N content in the InSbN alloys.

CHAPTER 4. $INSB_{1-x}N_x$ ALLOYS on GAAS AND GASB SUBSTRATES

4.1 Introduction

Previous work indicates that InSbN alloy could be obtained by homo-epitaxially growing on InSb substrate or ion implantation. However, the incorporation of N is limited to only few percents, and the degree of band gap reduction is also not enough to reach the 8- 14 μm atmosphere transmission window [10, 13, 48].

InSbN alloy hetero-epitaxially grown on GaAs by MOCVD will be discussed in this chapter. GaAs has been used as the substrate for the growth of InSb epilayers for many years. The growth of this material on GaAs substrate have already been explored via various growth techniques, such as LPE, ALE, MBE, magnetron sputtering, plasma assisted epitaxy and MOCVD [193-198], etc. Even though there is a large lattice mismatch, quite high values of mobility have been obtained from InSb epilayer on GaAs substrate in many works [199-200]. The use of GaAs substrate is interesting because a wide band gap and semi-insulating substrate facilitates electrical isolation and decreases parasitic capacitances. It is also convenient for the signal processing circuits and integration of infrared detection like silicon charge-couple devices (CCD). Hence, the growth of InSbN on GaAs substrate is very meaningful for its future use in photo-detectors. To date, several studies about InSbN on GaAs substrate have been reported by using MBE [8, 9, 11, 201-203]. However, not much work has been done to the hetero-epitaxial growth of InSbN by using MOCVD except the only one reported by T. Ishiguro [171].

InSbN alloy hetero-epitaxially grown on GaSb substrate was investigated in section 4.3. Compared to GaAs, the lattice mismatch between GaSb and InSb is much smaller. Till now, not much work is present on the heteroepitaxial growth of InSbN on GaSb substrate. In this work, InSbN alloys were prepared by using GaSb as substrate, aiming to acquire alloys with high quality and long cut-off wavelength.

4.2 InSbN alloys on GaAs substrate

4.2.1 Growth and annealing treatment

The samples were grown on semi-insulating GaAs (001) by MOCVD. The input V/III and N/(Sb+N) ratios were kept at 56.7 and 0.93, respectively. The growth temperature was set at 410 ^{o}C. The reactor pressure was kept at 100 mbar and the growth time was 30 mins. Hydrogen was also used as carrier gas.

SEM images indicate that the surface of the sample looks a little bit rough, which should be due to film imperfection caused by the low growth temperature and the large lattice mismatch between the material and substrate. In order to improve the alloy quality and also see the effect on the N incorporation, rapid annealing treatment has been applied on InSbN alloy in nitrogen ambience at temperatures of 440 ^{o}C, 450 ^{o}C and 460 ^{o}C, respectively. The annealing is conducted under atmosphere pressure for 3 mins. Figure 4.1 shows the XRD spectra of sample annealed at different temperatures. We can see that obvious peak referring to $InSb_{1-x}N_x$ epilayer could be

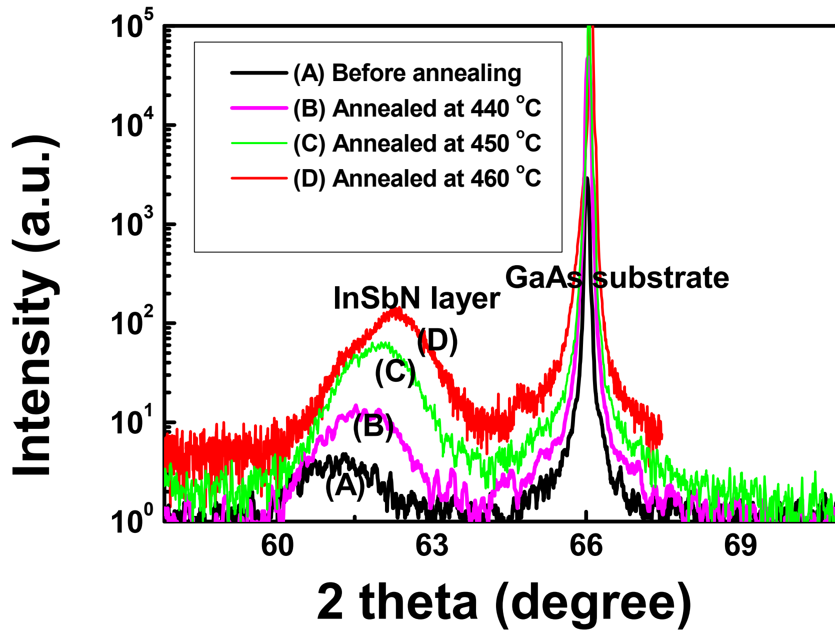

Figure 4.1Spectra of XRD obtained from (004) diffraction of annealed and unannealed $InSb_{1-x}N_x$ samples.

observed, demonstrating that nitrogen has been incorporated into the grown InSb. The peak intensity of the InSbN layer gets stronger, which means that the sample quality is improved by the annealing treatment. Besides, there is a blue shift of the peak position after the annealing. This is probably due to the conversion of N form in the alloy and will be discussed later in this chapter.

4.2.2 Optical property

In order to study the optical property and also the effect of N incorporation on alloy band-gap, photoluminescence measurement was made over a wide temperature range. Figure 4.2 shows the PL spectra of the alloy measured at 10 K. Before annealing treatment, no PL emission is detected, whereas peaks around at 7.2 μm are

observed for all annealed samples. The PL intensity becomes stronger after the annealing treatment, demonstrating an improvement in the sample quality.

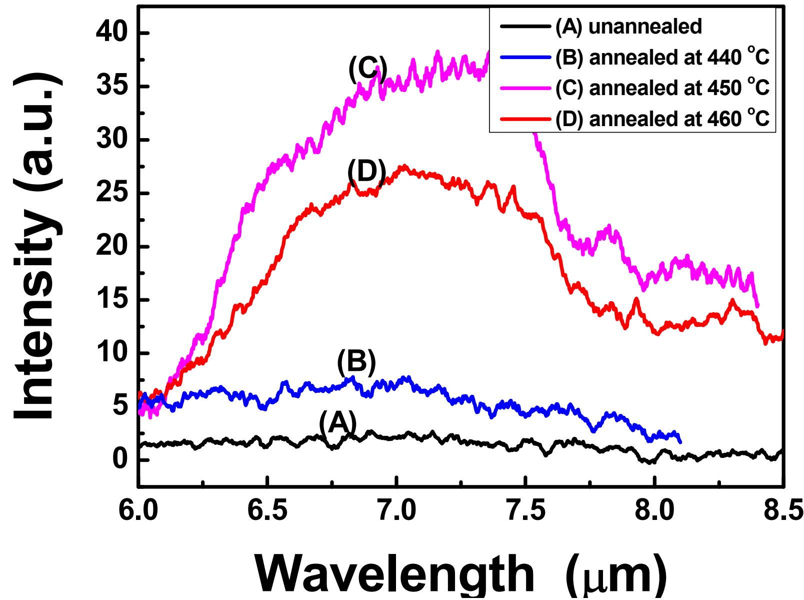

Figure 4.2 PL spectra of the alloys with and without annealing treatment measured at 10 K for 3 mins.

Moreover, we can see a small red shift of PL position when increasing the annealing temperature. The wavelength of PL is near 7.4 μm for the film annealed at 460 °C. Although the peak intensity obtained here is not strong enough due to the imperfection of quality, the PL wavelength we got is every close to the long wavelength atmospheric window from 8 to 14 μm, which is hopeful for the application of the InSbN alloy in long wavelength area. The broadness of the PL emission is very big, which should be due to defects induced by the big mismatch between the alloy and GaAs substrate. Figure 4.3 gives the PL spectra of the sample annealed at 450 °C for 3, 5 and 10 mins, respectively. It is seen that the PL emission moves to longer wavelength by increasing annealing time. The emission wavelength

reaches nearly 8 μm with 10 mins annealing time. We didn't prolong the annealing time further since the emission intensity has degradation. It seems that annealing with either too high or too long duration may bring damage to the emission efficiency of the samples.

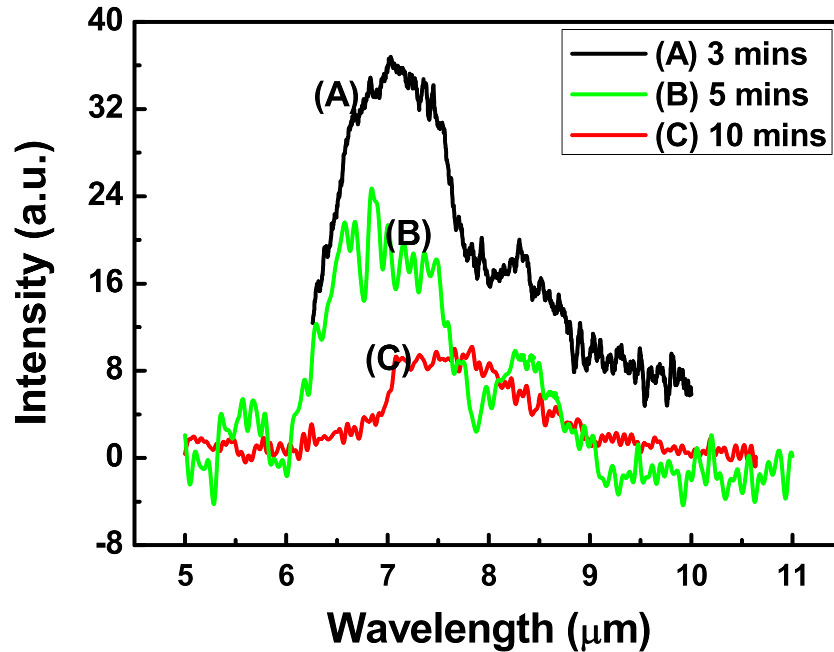

Figure 4.3 PL spectra of the sample annealed at 450 °C for 3, 5 and 10 mins, respectively.

To see the temperature dependence of band gap energy, PL spectra were measured at different temperatures and the result of the alloy annealed at 450 °C is shown in Figure 4.4. With increasing the temperature, we can see that the PL peak has a red shift. Table 4.1 gives the positions of the PL spectrum peaks under different measuring temperatures. It is seen that the PL peak shifts from 7 μm at 10 K to 7.8 μm at 100 K. Since the peak intensity drops dramatically, the PL signals become too weak to be recorded above 100 K. But according to the estimation by the Varshni

equation, the PL peak could be around 10 μm at room temperature.

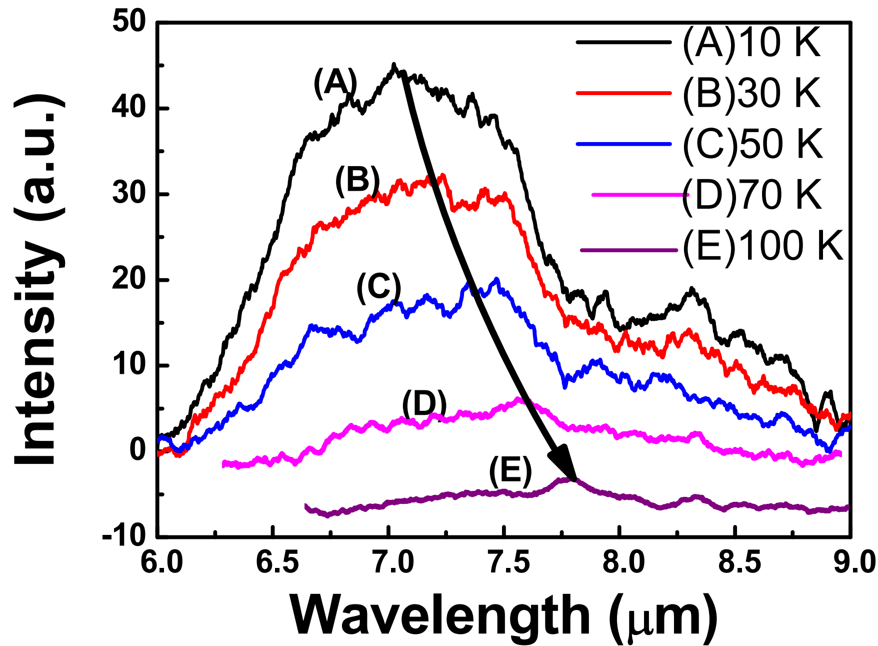

Figure 4.4 Temperature dependence of PL spectra of the alloy annealed at 450°C.

Table 4.1 PL peak positions of InSbN alloy annealed at 450 °C at different temperatures.

Measuring T	10 K	30 K	50 K	70 K	100 K
PL wavelength (μm)	7.0	7.2	7.5	7.6	7.8

The measurement results above indicate that a mismatch seems to exist between the N concentration and the PL wavelength. According to the XRD results as shown

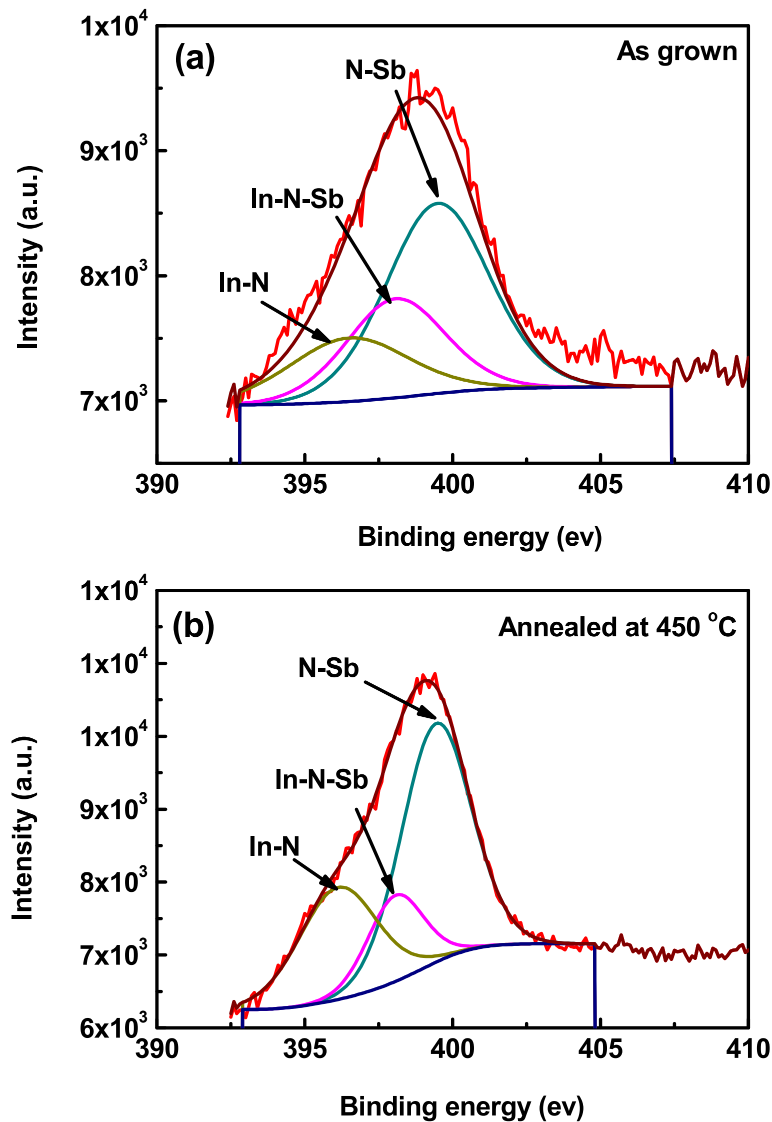

Figure 4.5 XPS spectra in N1s of InSbN alloy, (a) before annealing and (b) after annealing at 450°C.

in Figure 4.1, there is a big lattice separation between the InSbN alloys and GaAs substrate, indicating a quite large N incorporation in the alloys. Theoretical calculation demonstrates the N incorporation required in $InSb_{1-x}N_x$ alloy to reach a band gap of 0.1 eV is only about x = 0.01. However, the band gap of alloy is around

0.124 eV (λ~ 10 μm) at room temperature, which is still far from the theoretical revelation.

The reason for this phenomenon is because the N elements in the $InSb_{1-x}N_x$ alloy which cause band-gap reduction only take a small portion of the total N incorporation. To get information about N bonding configuration, the sample was characterized by XPS measurement. Figure 4.5 (a) and (b) indicate the XPS spectrum of the samples in N1s region before annealing and annealed at 450 ^{o}C. The curve could be fitted into three types of nitrogen bonds: substutional N (In-N) at a binding energy of (396.5 eV), interstitial N (In-N-Sb) at 397.9 eV and antisite N (Sb-N) at 399 eV. The XPS spectra indicate that the N-In bonding only takes up a small percentage of the total N in the film, most part of that is at the antisite position. It is already known that only substitutional N-In bonding will lead to the band-gap reducing effect. Therefore, the wavelength of the PL emission in our deposited sample is far away from the theoretical value. Besides, we can see that the part of N at interstitial position decreases after annealing. According to the model suggested by Chen et al [192], interstitial N would lead to lattice expansion, which also could explain the shift of X-ray diffraction peak as shown in Figure 4.1.

4.3 InSbN alloys on GaSb substrate

Above work indicated that quite high nitrogen content could be introduced to InSb grown on GaAs, but the alloy quality was not quite good due to the large lattice mismatch to InSb. In comparison to GaAs, the lattice mismatch between GaSb and InSb is much smaller. Therefore, InSbN alloys with high quality could probably be obtained on GaSb substrate.

The details of the sample growth have been elaborated in previous section 4. 2. The growth parameters like temperature, reactor pressure and growth temperature were similar to those used for the alloys on GaAs substrate. Different input N/(Sb+N) ratios were adopted to adjust the N content in the alloys. After the deposition, annealing treatments at different temperatures were applied on the samples.

The treatment was done in N_2 ambience and the annealing duration was 3 mins. Figure 4.6 shows the (004) 2θ /ω scans of samples annealed at different temperatures. Apparent peaks corresponding to $InSb_{1-x}N_x$ epilayer could be observed in all curves on GaSb substrate and a blue shift of the eplilayer peak with annealing temperature was also observed, which is a similar situation to those of layers on GaAs substrate.

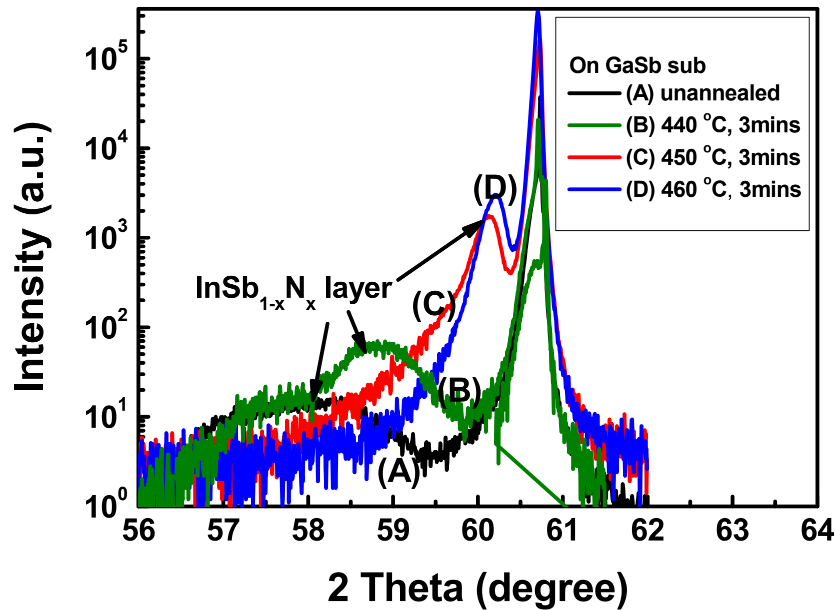

Figure 4.6 XRD (004) 2θ /ω scans of samples annealed at different temperatures.

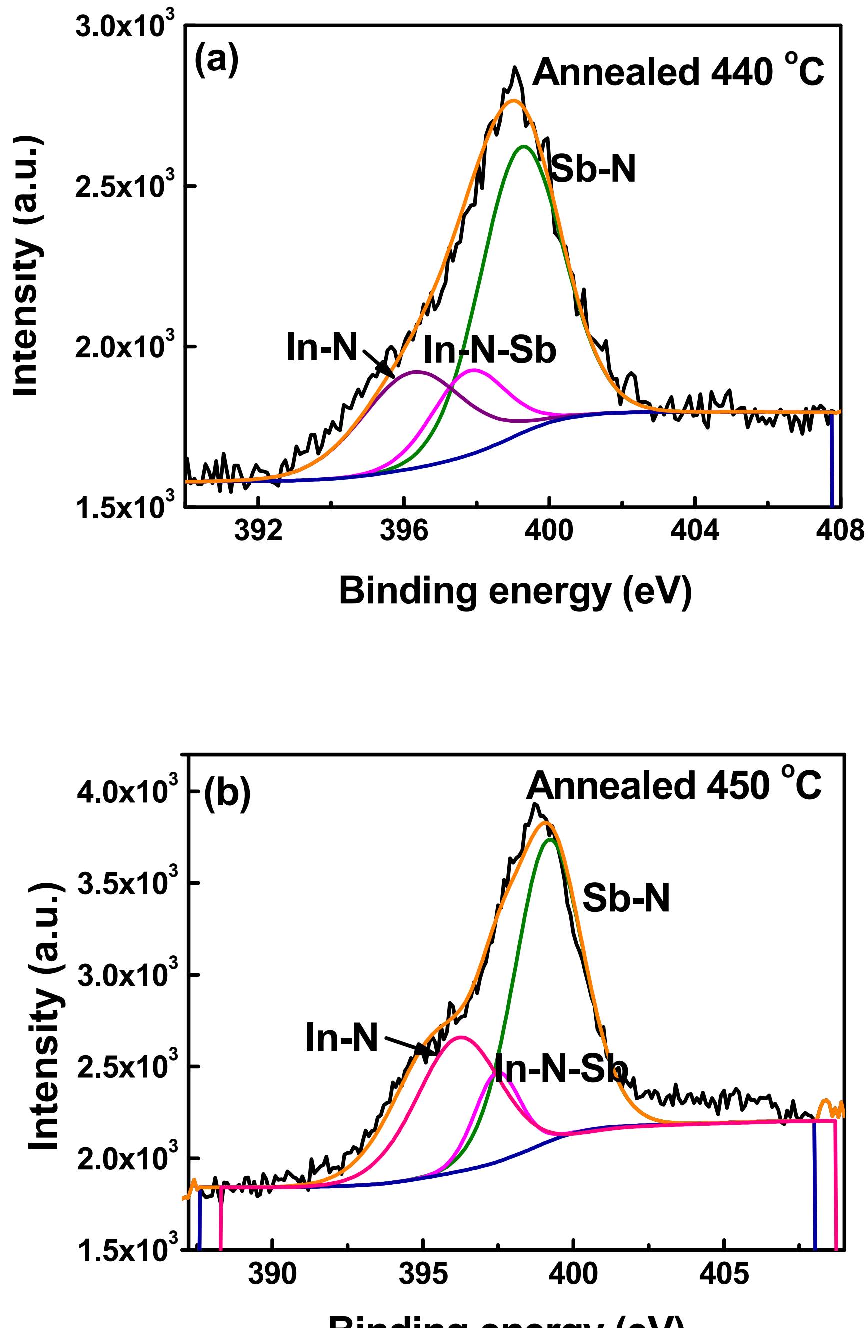

Figure 4.7 XPS spectra in N1s of InSbN alloys after annealing at (a) 440 °C and (b) 450°C.

Figure 4.7 (a) and (b) show the XPS spectrum in N1s region of the alloys after being annealed at 440 ^{o}C and 450 ^{o}C, respectively. From the two spectra, the portion of N at antisite N_{In} increased by increasing the annealing temperature and the interstitial N has decreased, which could explain the change of lattice separation in the XRD spectra.

PL measurement was carried out to investigate the energy band and defect state in $InSb_{1-x}N_x$ alloys. Figure 4.8 shows the PL spectrum of samples annealed at different temperatures. No emission is detected before the annealing treatment. However, two obvious PL peaks with very high intensity can be observed in all annealed

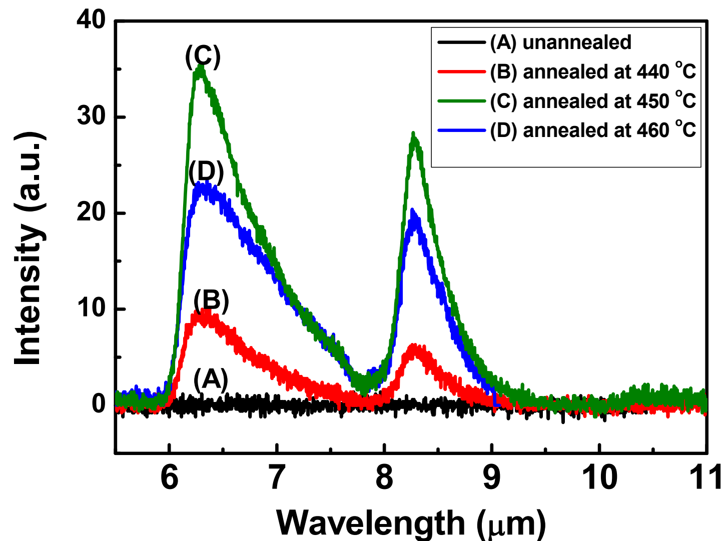

Figure 4.8 PL spectra of the alloys annealed at 440 ^{o}C, 450°C and 460 ^{o}C measured at 10 K.

curves. The peak at ~ 6.3 μm (0.197 eV) should be due to the near band emission, which is quite close to the band gap energy of InSb at room temperature (0.17 eV). For the alloys on GaSb substrate, there is a large shift of the band gap emission in comparison to the sample grown on InSb substrate (~ 5.4 μm), which demonstrates the effects of N incorporation on bang gap reduction.

In addition to the 6.3 μm peak, the emission peak at ~ 8.3 μm (0.155 eV) was also observed in all spectra curves, which is already included in the long wavelength atmospheric window between 8–14 μm and peak intensity is comparably strong regarding to the main band emission.

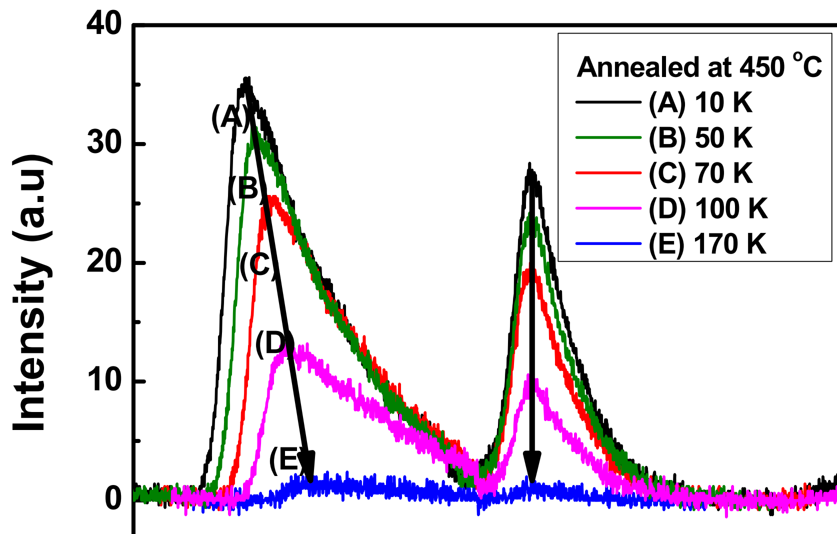

Figure 4.9 Temperature dependence of PL spectra of the alloy annealed at 450°C.

In order to clarify the origin of the emission peaked at 8.3 μm and also to find the temperature dependence of energy band gap, PL measurements over a wide temperature range from 10 K to 170 K were performed. The sample annealed at 450 ^oC is chosen here as an example. The temperature dependent PL spectra are shown in Figure 4.9. A small red shift of the near band emission can be seen by raising the measurement temperature. The emitted wavelength is increased from 6.3 μm at 10 K to ~ 6.7 μm at 170 K, which is believed to be due to the lattice dilation caused by the change of temperature. Different from the main band emission, the emission peak at 8.3 μm is basically stationary. This behavior demonstrates that the peak should be attributed to an impurity emission.

Based on all of the above observation and results, it seems that the antisite N_{In} defects are responsible for this emission. From the PL spectra shown in Figure 4.8, the intensity ratios between the main band emission (I_M) and defect emission (I_D) are calculated. The I_M/I_D values for the alloys annealed at 440 ^oC, 450 ^oC, 460 ^oC are 1.6, 1.3 and 1.15, respectively. It means the relative intensity of the defect emission gets improved while enhancing the annealing temperature. The XPS spectra in Figure 4.7 indicate that the content of antisite N_{In} is also augmented by raising the annealing temperature. It tells higher antisite N_{In} concentration may lead to higher emission at 8.3 μm and provides the evidence that the cause of the defect emission is probably the formation of defect energy state from antisite N_{In} in the alloy band gap.

Tto confirm the above point, we did one more growth with different N/(Sb+N) ratio at 0.9. The Sb/In source ratio and growth temperature were still kept at 4.2 and 410 ^oC. Annealing treatment at 450 ^oC with 3 mins was also applied to the

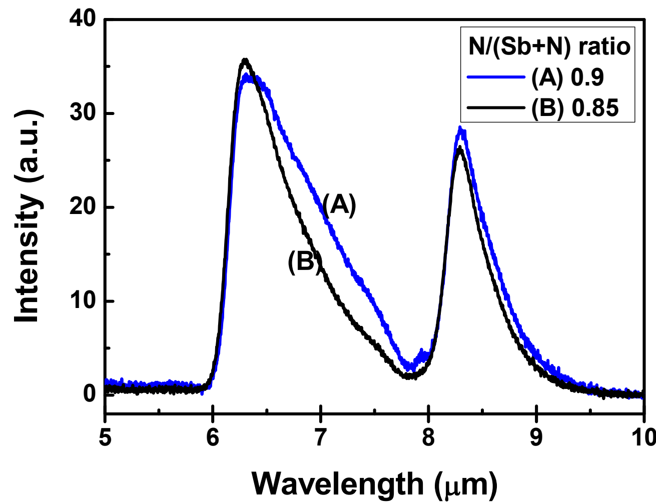

Figure 4.10 PL spectra of the alloys grown with N/(Sb+N) ratios of 0.85 and 0.9, respectively, measured at 10 K.

samples after the deposition. The PL spectrum of the alloys grown at different N/(Sb+N) ratios is given in Figure 4.10. It is the same as previous samples, two evident peaks referring to band emission and defect emission can be seen in the spectra. The intensity ratios I_M/I_D calculated here for the alloy with N/(Sb+N) ratio at 0.9 is 1.19. This value is smaller than that of the alloy with N/(Sb+N) ratio at 0.85, which demonstrates that higher defect emission is obtained while the sample with larger N/(Sb+N) ratio. XPS measurement was made to get information about antisite N_{In} in the sample and the spectra is as shown in Figure 4.11. In comparison to the N configuration indicated in Figure 4.7 (a), antisite N_{In} is occupying a larger component in this alloy, which means more N_{In} defect can be generated in the case of higher N/(Sb+N) ratio. These results confirm the emission at 8.3 μm should come from N_{In} defects.

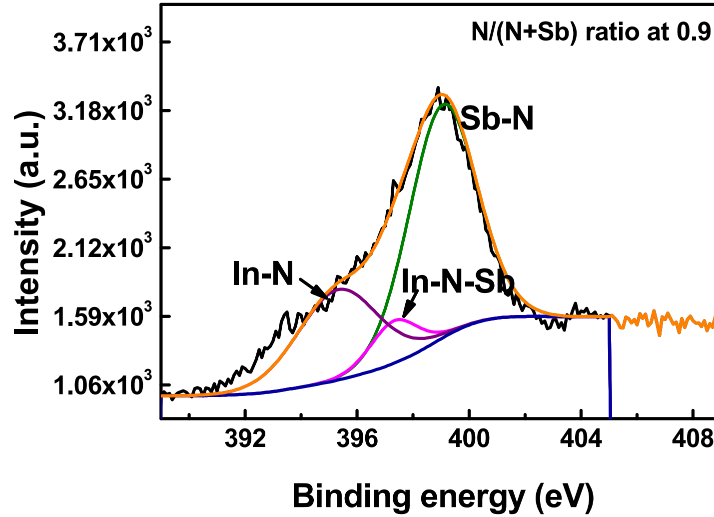

Figure 4.11 XPS spectra in N1s of the InSbN alloy grown with the N/(Sb+N) ratio of 0.9.

4.4 Summary

$InSb_{1-x}N_x$ alloys have been hetero-epitaxially deposited on GaAs, and GaSb substrates by MOCVD to investigate the influence of substrate on the incorporation of N into InSb. The effect of the annealing treatment on the $InSb_{1-x}N_x$ alloys on GaAs is also well studied. PL results at 10 K indicate that PL intensity becomes stronger, accompanying with a small red shift of peak position with the annealing temperature varying from 440 ^{o}C to 460 ^{o}C. The wavelength of PL we obtained here is around 7.4 μm for the film annealed at 460 ^{o}C. For the alloys on GaSb, the transition wavelength of the alloys is prolonged to 6.3 μm by N incorporation. In addition to the main band emission, a peak around at 8.3 μm also can be detected, this observation is beneficial to the alloy application in long infrared wavelength area. With the combination of PL and XPS measurement observation, antisite N_{In} defect was attributed to the origin of defect emission at 8.3 μm.

CHAPTER 5.GROWTH AND CHARACTERIZATION OF INSB NANOWIRES ON INSB SUBSTRATE

Considerable study has been carried out on InSb for its fascinating properties. However, most research work was imposed on bulk InSb material or quantum dots in the past. The study on preparation and properties of InSb nanowire is very scarce, perhaps due to the difficulty of growth of this material. Many methods like anodic alumina membranes (AAM), thermal chemical vapor deposition and chemical beam epitaxy (CBE) have been adopted to fabricate InSb nanowire [155, 204-208]. However, the study on fabrication and properties of InSb nanowire is far from enough. Besides, the InSb nanowires prepared by AAM and thermal CVD often encounter the quality and uniformity issues.

So far report on single crystalline vertical InSb nanowire is limited [206, 209-210]. In this chapter, we will present the synthesis and characterization of InSb nanowires epitaxially both on InSb (100, 111) substrates by MOCVD. The dependence of InSb nanowire growth on V/III source ratio, and temperature has been carefully studied. Uniform InSb nanowires with high density vertically on InSb substrate are obtained, which makes future application of them in electronic devices possilbe. The underlying growth mechanism of InSb nanowire will also be discussed.

5.1 InSb nanowires on InSb (100)

The precursors used in the growth were still trimethylgallium (TMSb) and trimethylindium (TMIn). H_2 was used as carrier gas. Different growth parameters

were adopted to see the dependence on the InSb nanowires. Both InSb wafers along (001) and (111) B were used as substrates. Before transferring to reactor, the substrates were dispersed with Au aerosols as catalyst and the sizes of catalyst nanoparticles are around 40 nm.

The effect of temperature on the growth was first investigated. We tried to find proper temperature for the growth and it was turned out that the temperature parameter for growing InSb NW had a very narrow range, which also may explain the difficulty of growing InSb NW. Figure 5. 1 (a) to (d) show the SEM images of the samples on an InSb (001) substrate grown from 380 ^{o}C to 410 ^{o}C with a duration of 30 mins, and a V/III ratio of 60. The cracking efficiency of TMSb is limited at low temperature, leading to an actual lower V/III ratio than the input value. Therefore, the input V/III ratio needs to be set at a higher value in order to make sure there is enough Sb supply.

A crystallization process is generally divided into two steps: nucleation and growth. The control of these two steps has significant influence on the properties of final products like crystal structure and quality. The rate of nucleation can be expressed in the form of Arrhenius equation, which is commonly used for a thermally activated process:

$$J = A \exp(\frac{-\Delta G}{kT}) \qquad (5.1)$$

where ΔG is the overall Gibbz free energy, indicating an energy barrier for a nucleation process. From this equation, it could be noted that the nucleation rate would be suppressed at low temperature, which may explain that a low density of InSb nanorod is observed on the sample grown at 380 ^{o}C. With increasing the

temperature, the nucleation rate would increase and thus leading to a higher density of product for the samples grown above 380 ^{o}C

For these four samples, the short rods were predominately found at the growth temperature of 390 ^{o}C. Above this temperature, InSb nanorods suffer deterioration with the increase of temperature and are hardly seen on the sample grown at 410 ^{o}C. Previous literatures indicate that appropriate temperatures for growing InSb NWs are normally low, while high growth temperature may easily lead to the formation of bulk material. However, low temperature may decrease the growth rate and also result in insufficient Sb source due to incomplete decomposition of TMSb, which may consequently hinder the growth of InSb nanorods. As shown in Figure 5. 1 (a), the lengths of nanorods grown at 380 ^{o}C are shorter than those at 390 ^{o}C, which are probably owing to the decrease of growth rate. The lengths of InSb nanorods at 390 ^{o}C are around 1.5- 2 μm and the diameter around 30 nm.

It seems that the InSb nanorods on Sample (b) have an orientation along [1-10], which might be due to two possible reasons. The first reason is the mis-cut of the substrate. The InSb substrate used is along (100) with a mis-cut of $\pm 5^{o}$, so that surface atomic steps may form along a certain direction; The second reason may be the surface re-construction due to the rearrangement of surface dangling bonds. In the case of GaAs, dimer arrays will form along a certain direction, typically [1-10] direction, which has been demonstrated in previous literature [211-212]. As indicated in the inserted image of Sample (b), an obvious tip could be seen at the head of each nanorod, indicating tip-led growth of nanrods. This should be relevant to the growth mechanism, which will be discussed later in the text.

Figure 5.1 InSb nanorods grown at diffrerent temperatures on InSb (100) substrate with a fixed V/III ratio of 60.

Based on the elaboration above, a conclusion could be drawn that 390 ^{o}C seems to be an optimum temperature for growing InSb nanorods. In addition to temperature, V/III source ratio also imposes great influence on the growth. To examine the effect of V/III ratio on growth, we set a series of V/III ratios, for a fixed temperature of 390 ^{o}C at a constant group III input source. As shown in Figure 5.2, a clear dependence of nanorod morphology on V/III ratios between 30 and 80 could be observed. For the sample (a) and (d), the V/III ratios are 30 and 80 respectively, which may lead to the

shortage of Sb or In elements during the nucleation process and thus result in a lower density of product. In addition, it can be seen that the length of InSb nanorods increases with increasing the V/III ratio to 60, while the diameter decreases slightly at the same time. With raising the V/III ratio continuously to 80, the diameter of nanorods no significant change, but the axial growth rate seems to be slower. This is probably because the excessive Sb source affects the migration length on the growing interface or the surface, leading to a change in the V/III ratio.

In addition, the orientation of the InSb nanorods on these four samples indicates certain distinction. One reason might be the images being taken from different angles during the SEM measurement. For the orientation disorder of the product on Sample (a) and (d), it should be due to the inapproperiate V/III ratios adopted. Previous discussion indicates that there should be a growth window in term of V/III ratio for the InSb nanorod. Too high or too low V/III ratios not only suppress the nucleation, but also harm the growth of InSb nanorods.

From all the morphology images of samples above, a small tip could be seen at the head top of InSb nanorods, which may be used to explain the growth mechanism of InSb nanorods here. In order to analyze the content of the tip, EDX was applied by using both point analysis and line scanning. The point analysis was performed just in the top region of InSb nanorods. Figure 5.3 (a) shows the SEM picture of the actual position for the point detection. From the point EDX spectrum, we can see that the head tip is a alloy composed of mainly In, and Sb with small amount of Au. The measured compositions are 82% of indium, 16% of antimony and about 2% of gold, respectively. This confirms that the tip is indium rich, indicating an indium tip-led growth process.

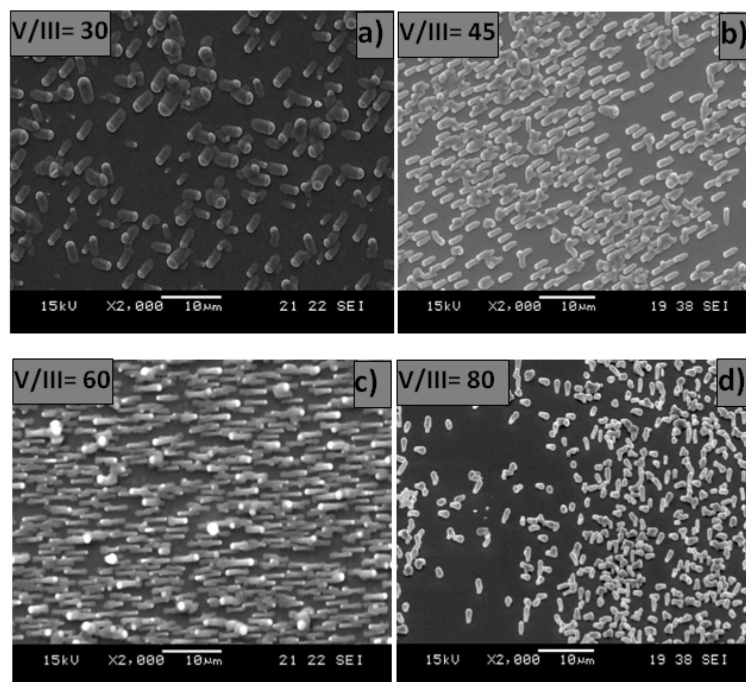

Figure 5.2 InSb nanorods grown at diffrerent V/III ratios on InSb (100) substrate at a fixed temperature of 390 ^{o}C.

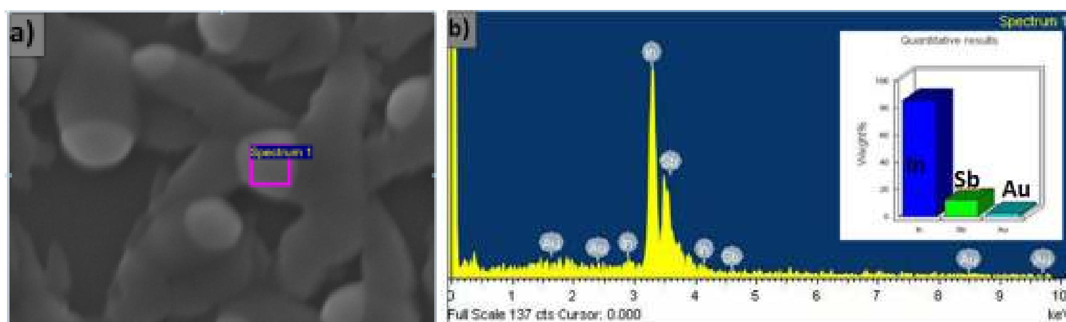

Figure 5.3 EDX analysis performed in the top region of InSb. (a) The SEM image of the probing area, and (b) the corresponding EDX spectrum.

5.2 InSb nanowires on InSb (111) B

The crystal orientation in semiconductor nanowires is profound as it not only affects surface properties, but also their optical and transport properties. Free-standing InSb nanowires hold promise for making fast and low power vertically integrated nanowire transistors, chemical/biological sensors or detectors, etc [213-215]. But the difficulty of growing well-defined vertical nanowires has suspended these technologies in the air. Recently, the growth of InSb-containing heterostructure nanowires (InSb/InAs, InSb/InP, InSb/GaAs) by MOCVD have been demonstrated [159-161], which possibly lights a hope on the practical application of InSb nanowire in low power devices. However, only a few reports about free-standing InSb nanowires are available in literature. The results as above show that the InSb nanorods obtained on InSb (100) substrate are lying laterally on substrate but not vertically. Nanowires generally grow in the crystal direction that minimizes the total free energy which, in most cases, is dominated by the surface free energy of the interface between the semiconductor and the metal catalyst. For compound semiconductors with zinc-blende structure like GaAs, InAs, InP, Si, it has been widely observed that the semiconductor–catalyst interface often forms a single surface at the lowest-energy (1 1 1) plane and thus nanowires tend to grow in the (1 1 1) direction for most growth conditions [216]. For III-V binary semiconductors, the (111) direction can be further distinguished into (111) A and (111) B, based on the type of surface termination. The (111) B (group-V terminated) is the lower energy plane, and consequently wafers in (111) B direction are generally adopted as substrate to grow nanowires. In the section below, we present the growth and characterization for the free-standing InSb nanowires on InSb (111) B substrate.

5.2.1 Growth and characterization

The details of growth are similar to the previous illustration. Before insertion to the MOCVD chamber, the substrates have been carefully treated to eliminate

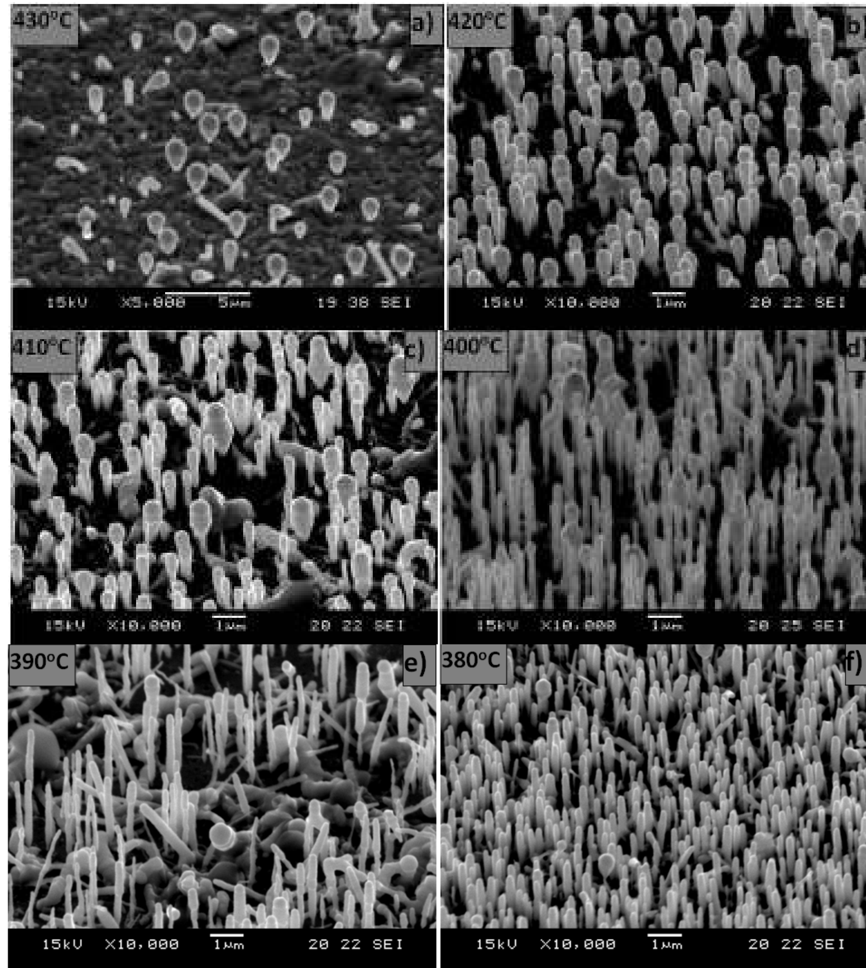

Figure 5.4 SEM images (45° angle view) of InSb nanowires epitaxially grown on InSb (111) B substrate, from 380 ^oC to 430 ^oC, with a V/III ratio of 50 and growth time of 30 mins, respectively. Dependence of morphologies on temperature is clearly observed.

oxide and contamination on the surface by HF solution and ethanol, and then being dispersed with Au aerosols. Different V/III ratios and temperatures were used to study their influence on the properties. In comparison to the InSb nanorods laterally on InSb (100), vertical InSb nanowires were realized here on InSb (111) substrates.

We observed a clear dependence of InSb nanowire morphology on temperature, from 380 ^{o}C to 430 ^{o}C with a V/III ratio of 50. The growth duration is 30 mins. The SEM images of free-standing InSb nanowires on InSb (111)B substrate are as shown in Figure 5.4 (a) to (f). There are no wires but large drops standing on the substrate with a diameter size of ~ 600 nm for the Sample (a) at 430 ^{o}C. Below the temperature of 430 ^{o}C, materials start precipitating from the head-tip and the production is more and more wire like.

Different from the growth on InSb (100) substrate, the product on InSb (111) B still shows a high density at a temperature of 380 ^{o}C (Figure 5.4 (f)). In comparison to the InSb (100) substrate, the InSb (111)B has lower surface energy, which makes the nucleation energy barrier (ΔG) of InSb nanowire on InSb (111)B lower than that on InSb (100) substrate. Therefore, considerable nucleation and growth of InSb nanowire are allowed on InSb (111)B substrate at a low temperature of 380 ^{o}C. With increasing temperature, the density of product has a tendency of decrease. At high temperature, the catalytic alloys must absorb more vapor to reach the supersaturation levels before precipitating nanowires, which may increase the nuclei size and thus facilitate the lateral growth of product.

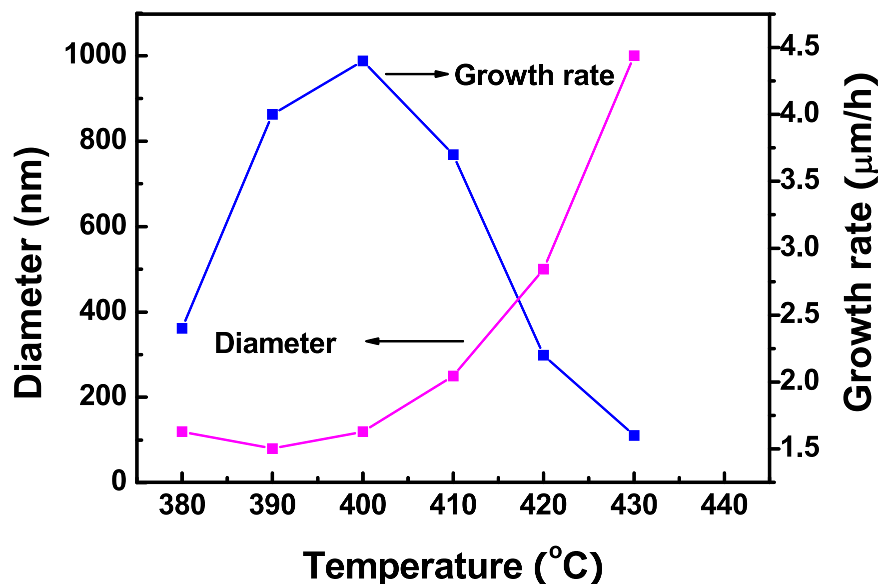

Figure 5.5 InSb nanowire diameter and growth rate as a function of temperature from 380 ^{o}C to 430 ^{o}C.

In addition, the length of nanowire first gets longer and then turns to the opposite direction at 390 ^{o}C, which means the growth rate is supposed to be limited at low temperature. The quantitative information on the relation between temperature and growth rate is indicated in Figure 5.5. No wire like production could be observed with growth temperature above 430 ^{o}C. To characterize the structural property of the production, we chose the sample grown at 400 ^{o}C for X-ray diffraction measurement and the XRD spectra (Figure 5.6) shows that the growth direction of the nanowire is mainly along (111) orientation and almost no other orientation peaks is observed, which indicates that the sample posses a single crystalline structure with quite high quality.

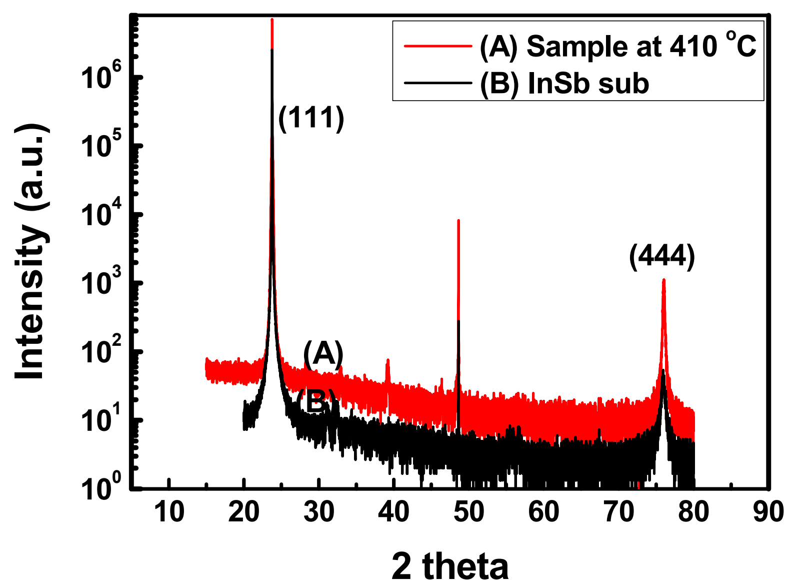

Figure 5.6 XRD spectra of InSb nanowires grown at 400 ^{o}C. InSb substrate was measured for reference.

In Figure 5.7 (a) to (d), the evolution of InSb nanowire growth on dependence of V/III ratio is illustrated by selected SEM images, at a fixed temperature of 400 ^{o}C and a constant group V molar flow. We can see a strong dependence of growth rate and diameter of InSb nanowire on input III/V ratio. The quantitative information on the relation between growth rate, diameter and V/III ratio is shown in Figure 5.7 (e). It is seen that InSb nanowires grows faster with decreasing V/III ratio to 50, but decreasing the V/III ratio further will reduce growth. Moreover, the diameter of the nanowires is growing larger with increasing input of group III sources. It seems that the lateral growth of InSb naowires is favored at high indium molar fraction.

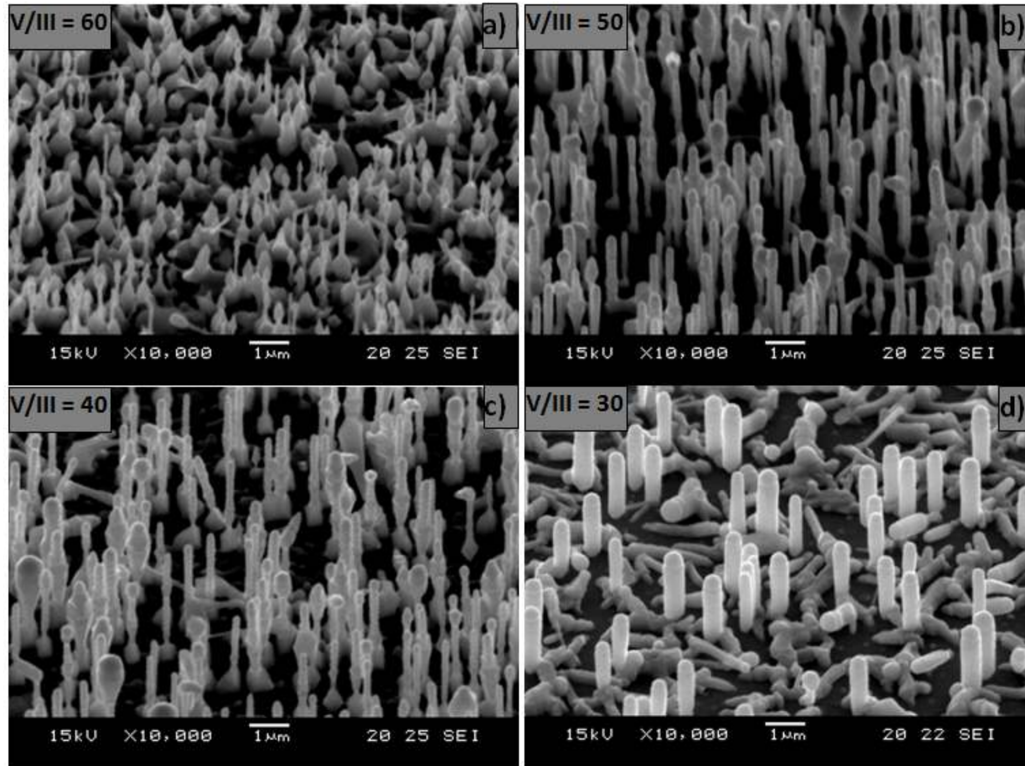

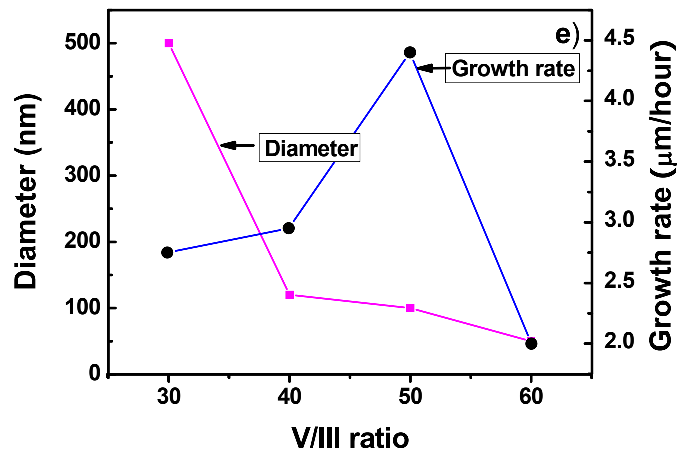

Figure 5.7 From (a) to (d), 45° angle view SEM micrographs of InSb nanowire morphology evolves with input V/III ratio from 30 to 60 at a fixed temperature of 400 ^{o}C. (e) Quantitative relation between growth rate, diameter and V/III ratio.

5.2.2 Growth mechanism

For one dimenstional semiconductor mateirals, various mechanisms like Vapor-Liquid-Solid (VLS), Vapor-solid-Solid (VSS), Vapor-Solid (VS) have been developed to explain their growth. Among these, VLS mechanism proposed by Wagner and Ellis has been most wildly used for the synthesis of semiconductor nanowires such as Si, GaN, GaAs, InAs, ZnO, ZnS, and SnO_2 etc. The VLS mechanism assumes that a liquid alloy forms above the eutectic point, which can rapidly absorb vapor source to super saturation levels and one dimensional growth can subsequently occur from alloy seeds. For the tip-led InSb nanorods fabricated in this work, the underlying mechanism seems to be related to VLS. In order to understand the growth behavior of III-V nanowires by using Au particles as catalyst, it is necessary to know how these materials interact first. Among all binary III-V materials, InSb is very special since not only a series of binary compounds between Au and In exist, but also one stable phase could be formed between Au and Sb ($AuSb_2$). No stable phases have been observed between Au and other V-group materials. Besides, a bunch of In-Au-Sb ternary pseudobinary systems like $AuIn_2$-InSb, AuIn-InSb, AuIn-Sb, γ,γ'-$AuSb_2$, $r\varepsilon,\varepsilon'$-$AuSb_2$, etc. have been identified [217]. Therefore, it is not easy for researches to depict the growth mechanism of InSb nanomaterial clearly.

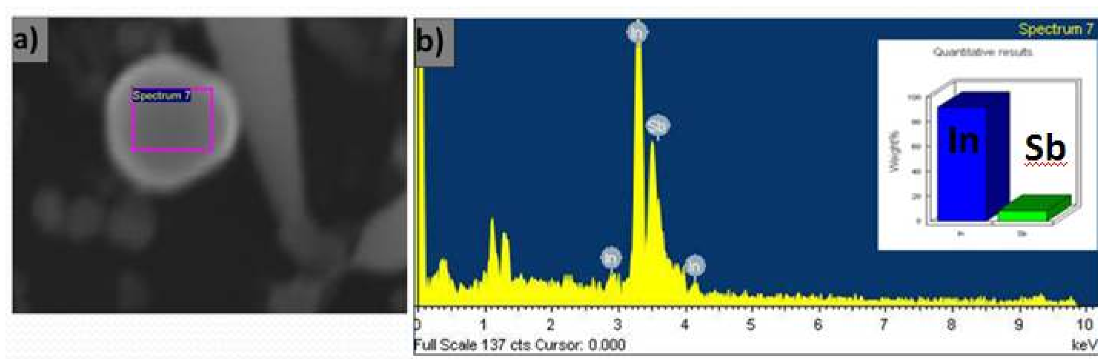

Figure 5.8 EDX analysis at the top area of InSb nanowire. (a) Image of the probing area, and (b) the corresponding EDX spectrum.

As indicated by the EDX spectrum in Figure 5.8, the head tip is indium rich, which means the tip-led growth of InSb nanorods should not be based on the Au-Sb alloy. We think that the underlying growth mechaism could probably be infered by the distribution variation of In, Sb content along the nanorod. To further investigate the growing information along the InSb nanorods, a line scan was performed along one single nanorods from the tip to the end and the spectra of the content of antimony and indium along the nanorod is shown in Figure 5.9. It is seen that indium and antimony are nearly equal in the alloy at the beginning.

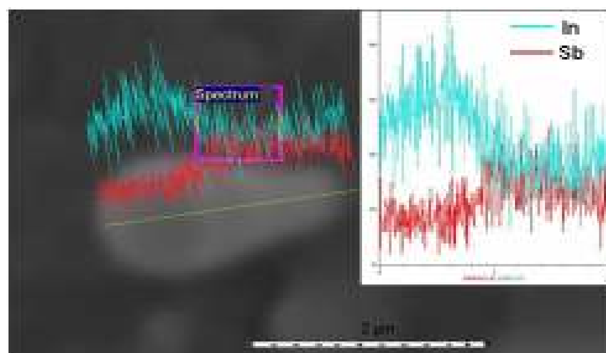

Figure 5.9 EDX Line scan of a single InSb nanowire. The inset curve indicates the indium and antimony varies along the InSb nanowire.

Before inletting indium source to the chamber, Sb source was introduced into growth tube in advance to protect the substrate. Therefore, it could be imagined that the Au particle may form an alloy with Sb first. When starting to grow, the alloy droplet seems to prefer absorbing indium than antimony. And then the amount of indium keeps increasing until reaches to a high limit, where the intake of antimony to the alloy speeds up again and InSb nanowire appears to start growing. Then the quantitative content of nanowire reaches approximately 50: 50 (In: Sb) at% ratio afterward until the end of growth. The whole growth process of InSb nanowires could be illustrated by the systemic diagram indicated by Figure 5.10 (a) to (d).

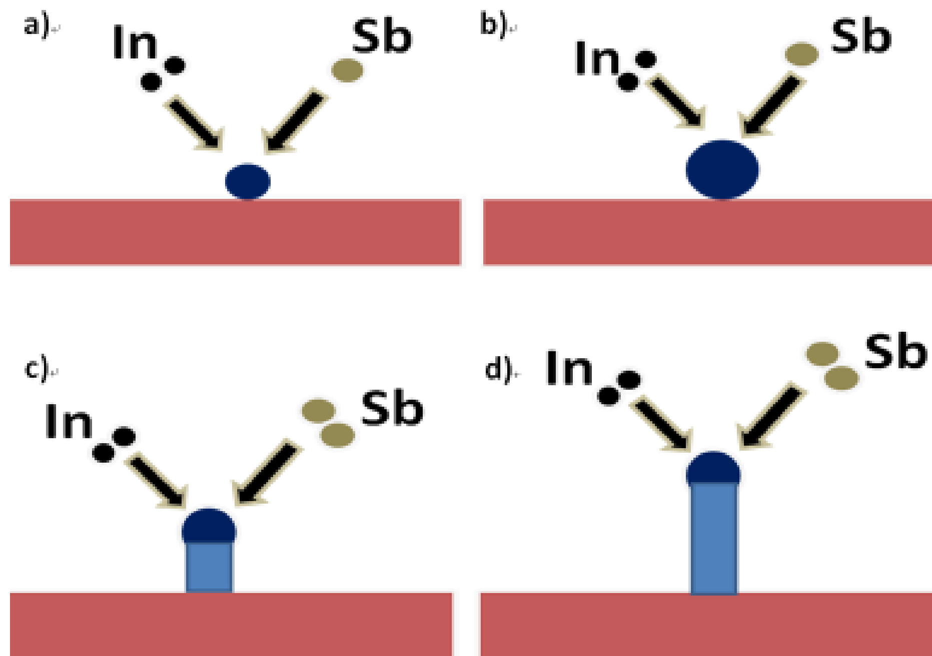

Figure 5.10 Schematic illustration of the growth process of a InSb nanowire. (a) and (b) An Au nanoparticle absorbs In and Sb atoms from the vapor and forms an alloy droplet, the alloy droplet is preferably absorbing indium than antimony at this stage; (c) the intake of antimony to the alloy speeds up

and InSb nanowire starts growing; (d) the content of nanowire gradually reaches 50: 50 (In: Sb) at% ratio to the end of growth.

Considering the head alloy contains certain amount of Sb, it is diffcult to say the InSb nanorods are grown from binary Au-In alloys. It appears there is only one possibility —the pseudobinary systems in the form of AuIn-InSb or $AuIn_2$-InSb, leading to the formation of rod production. Furthermore, if the considerably high capacity of In in the alloy is taken into account, it seems the $AuIn_2$-InSb should probably be the origin of InSb nanorods precipitating from. The $AuIn_2$-InSb has been indentified already to be a pseudo binary system. It has a eutectic point at around 723 K (450 ^{o}C) with up to 12% InSb in the alloy as indicated in Figure 5.11 [218]. For the VLS mechanism, a liquid alloy above eutectic point must exist before springing out nanowires. This suggests that if the VLS mechanism is applied to explain the growth here, the InSb should be precipitated from a supersaturated liquid particle (leaving $AuIn_2$).

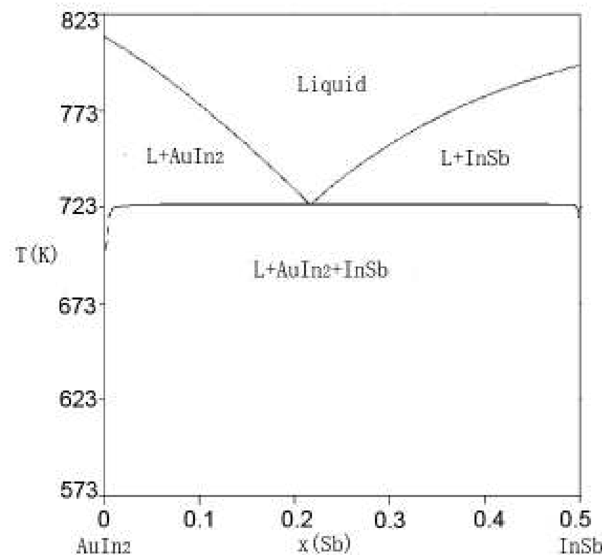

Figure 5.11 Phase diagram of the $AuIn_2$-InSb system.

However, our growth temperature (≤ 430 ^oC) is lower than the eutectic temperature of 450 ^oC, which means that the InSb nanowires would be precipitated from a supersaturated solid $AuIn_2$ particle. In this case, growth from a solid particle, the growth mechanism would match the VSS situation, which was first proposed in 1979 for Ag-catalyzed Si whiskers [219].

5.3 Self-nucleation of InSb nanowires

As shown above, InSb nanowires have been successfully synthesized on via VLS or VSS mechanism on InSb (100), (111) substrates with the assistance of Au nanoparticles. In the following paragraphs, we would demonstrate a mode of self-nucleation growth of InSb nanowire by MOCVD. Actually, it has been revealed that low melting group III metals like Ga, In could be employed for the catalyst-free growth (called 'self-catalysis') GaSb and InSb nanowires [208, 220]. Unlike the conventional tip-led VLS or VSS growth in the catalyst-assisted processes, the observed growth mode for self-catalysis is attributed to the extremely low equilibrium solubility of one group species in other group that leads to very small critical nuclei sizes which causes nucleation and growth rather than precipitation at the interface.

5.3.1 Based on indium droplet

In previous growth, after the annealing treatment at 500 ^oC in H_2 atmosphere to eliminate surface oxides, the temperature was decreased to growth point accompanying with input of Sb source, and then the In source was opened to start the growth, which as a result of leading to a VLS or VSS growth of InSb nanowires. For

the self-nucleation growth, most part of growth process is the same as above. The difference was, when the desired growth temperature was reached, TMIn source was introduced first into chamber to make a surface of indium rich, and which consequently serves as a seed layer of InSb nanowire growth. After 5 mins, The TMSb source valve was then turned on to initiate the growth. As a result, a group of samples were made and the SEM images were indicated in Figure 5.12. The morphologies of InSb nanowires obtained here are quite distinct from samples made previously. The InSb nanowires toward [111] in tapering shape are observed, the wires are growing based on triangle stems and no tips are found at the head of wires, which indicates a different mechanism from VLS and VSS growth.

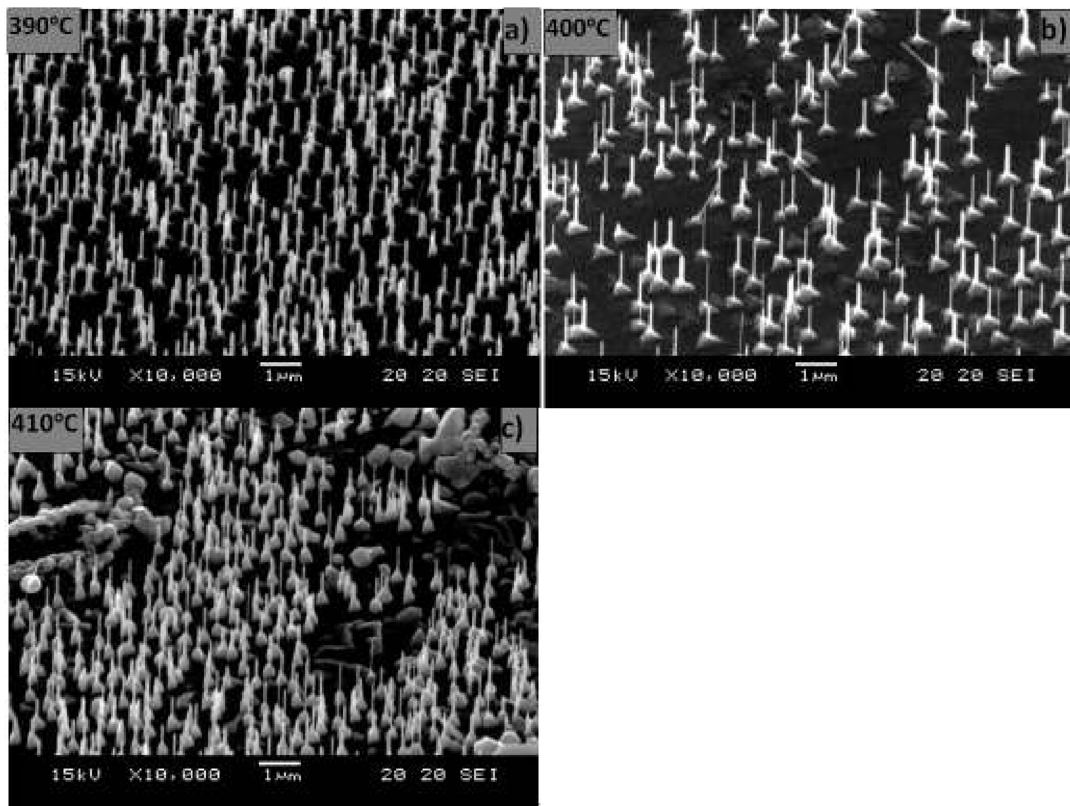

Figure 5.12 45° angle view SEM images of InSb nanowire dependent on growth temperature from 390 ^{o}C to 410 ^{o}C with a fixed V/III ratio of 45.

From the images shown in Figure 5. 12, it is observed that the diameter has quite high uniformity. The diameter is inversely proportional to the growth temperature, while the length increases a little bit and then decreases with enhancing the temperature. The InSb nanowires are nearly in form of an array, which has great value for the nanowire-based devices like vertical wrap-gate field effect transistor. Since most of the nanowire-based devices require nanowires grown as an array, the proposed growth mode here can be used to synthesize nanowire arrays on desired substrates.

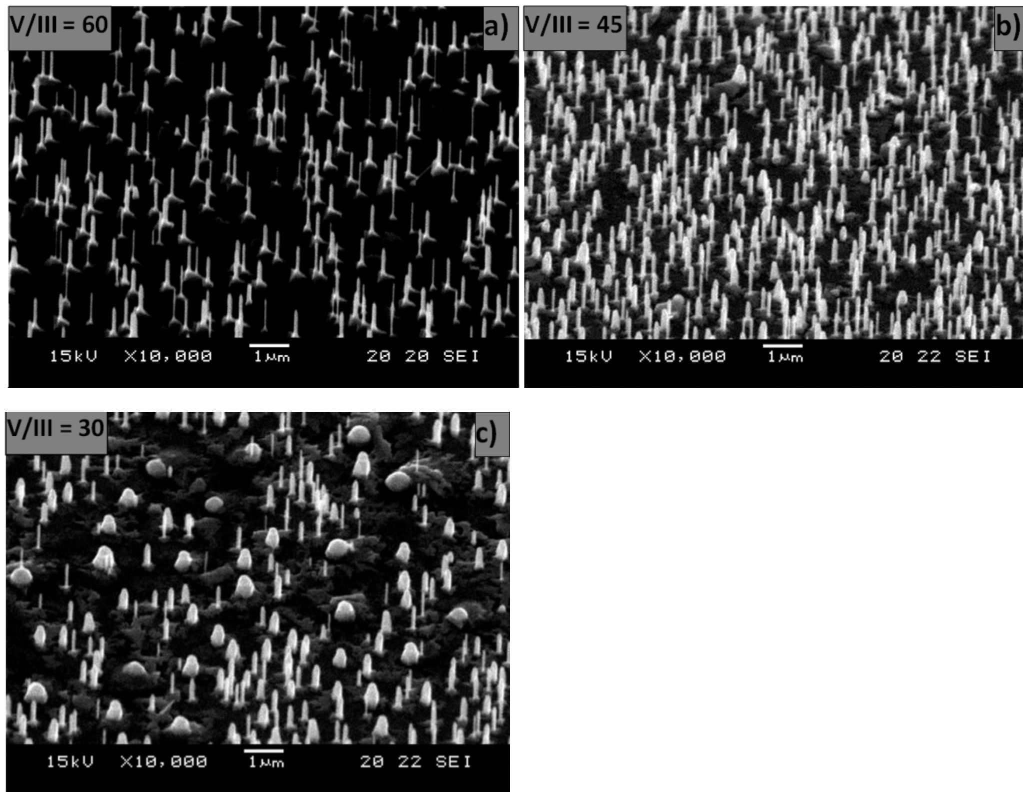

Figure 5.13 45° angle view SEM images of InSb nanowire dependent on V/III ratio from 30 to 60, with a fixed V/III ratio of 400 ^oC.

Figure 5.13 (a) to (c) indicate the dependence of InSb nanowires on V/III ratio for a fixed growth temperature at 400 ^{o}C. It also could be seen that the diameter changes inversely with the input V/III ratio, which is the same situation as previous observation, indicating lateral growth being favored by high group III source flux. It is generally noted that group-III materials diffuse much further on semiconductor surfaces than group-V materials. As a result, nanowire growth may be limited by the availability of group V source. At low V/III ratio, the flux of Sb atoms to the droplet surface is insufficient to keep up with the nanowire growth rate and then the droplet will grow in size, leading to nanowires in wider diameter. This observation is very apparent at a low V/ III ratio. The wire has a slight reduction in length with deceasing V/III ratio. However, no obvious change in length is observed for wires synthesized at variety of V/III ratios and temperatures, which we think here is probably owing to the limitation in diffusion of elements along the axis by the mode of growth. Therefore, the growth here is supposed to be related to self-nucleation.

To prove this point of view, EDX measurement along InSb nanowire at different parts was performed to examine the content of elements. The probing areas selected are following the growth direction of the wire, which are indicated as in Figure 5.14 (a). We can see that the InSb nanowires are explicitly growing on the base of alloy clusters. Element indium is dominant in alloy at the first stage of growth, which is primarily caused by the decomposition of TMIn at the beginning of the process. No gold was detected, perhaps it has been coverd by indium shell. The gold seems no longer to play the role of a catalyst in this situation. However, without the assistance of gold, no wires could be obtained on the substrates. Therefore, we infer that gold nanoparticles should have two functions in the growth. One is helping the

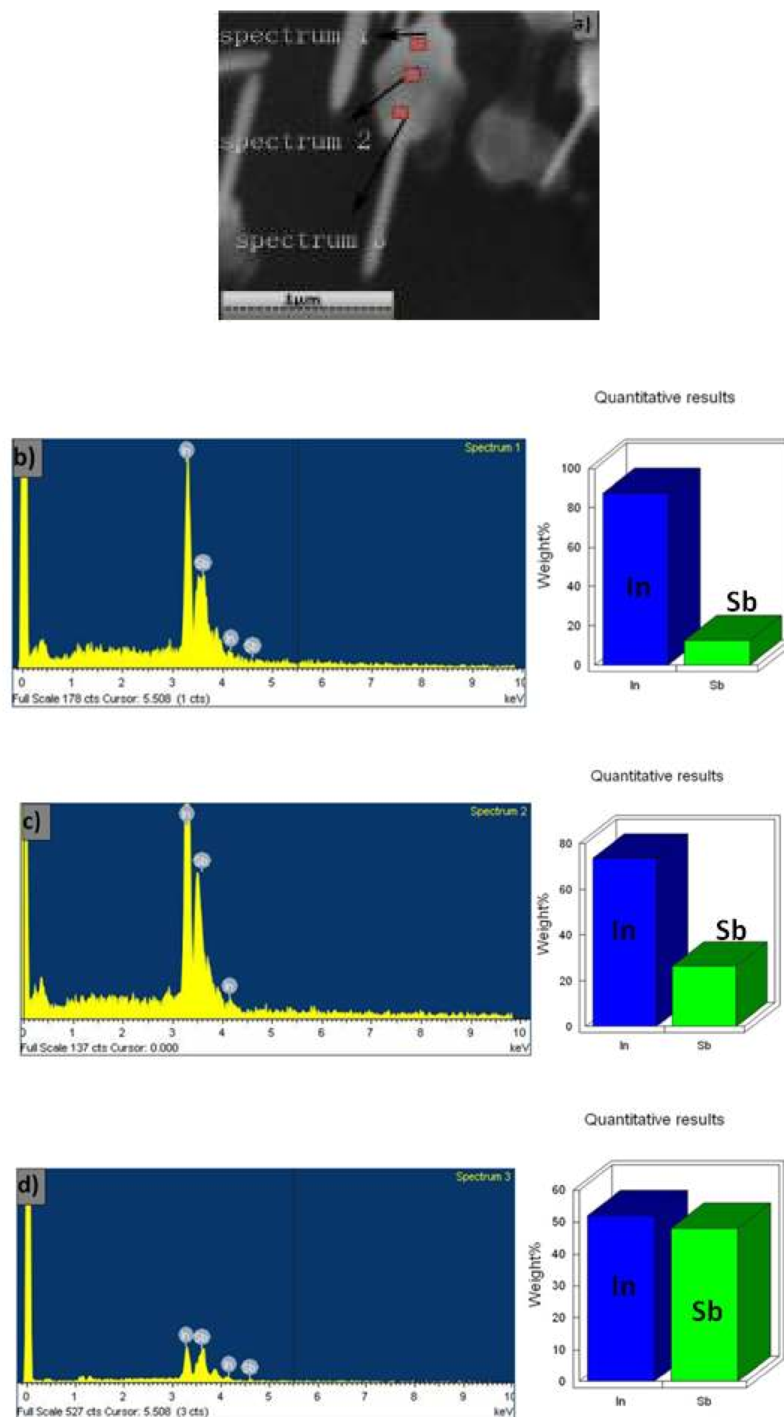

Figure 5.14 (a) SEM photograph of the EDX analysis at different point areas along a InSb nanowire. (b), (c) and (d) The EDX spectrum to the relative point areas.

decomposition of precursors at low growth temperature and the other should be acting as collecting tank for vapor source. It is hard to say whether the gold has played a role in decreasing the activation energy of InSb nanowires during the growth, which is not a universal effect and is insufficient to explain the general mechanism of particle-assisted nanowire growth. It has been shown that GaAs nanowires grown by MOVPE using trimethylgallium and arsine exhibit the same activation energy as the (non-catalyzed) GaAs layer growth in the same system with the same precursors [221].

The EDX spectrum for different positions of wire is given from Figure 5.14 (b) to (d). With the growth going on, the content of indium dramatically decreases along the wire, while antimony behaves in opposite way. Specific data of element atomic percentage is summarized in table 5.1. The quantitative percentages of indium and antimony at the front point of the alloy, indicated by spectrum 3, are 51.3% and 48.7%, respectively, which is quite close to stoichiometric InSb, indicating good quality of the grown wires. Figure 5.15 gives the binary phase diagram of the In-Sb system with two eutectics. At indium rich side, the eutectic solubility is ~0.5 at% of antimony in indium. Hence in principle, it should be possible to spontaneously

Table 5.1 Specific data of element atomic percent of the corresponding spectrum.

	Spectrum 1	Spectrum 2	Spectrum 3
In (atomic%)	78.2	64.3	51.3
Sb (atomic%)	21.7	45.7	48.7

nucleate InSb crystal nuclei by supersaturating molten indium droplets with antimony. The spontaneity of nucleation could be explained based on the thermodynamic arguments proposed by Chandrasekeran et al. [222] It has been suggested that there exists a supersaturation limit at which the nucleation of InSb from indium melt tends to be spontaneous. Bulk nucleation of InSb nanowires by antimonidization over

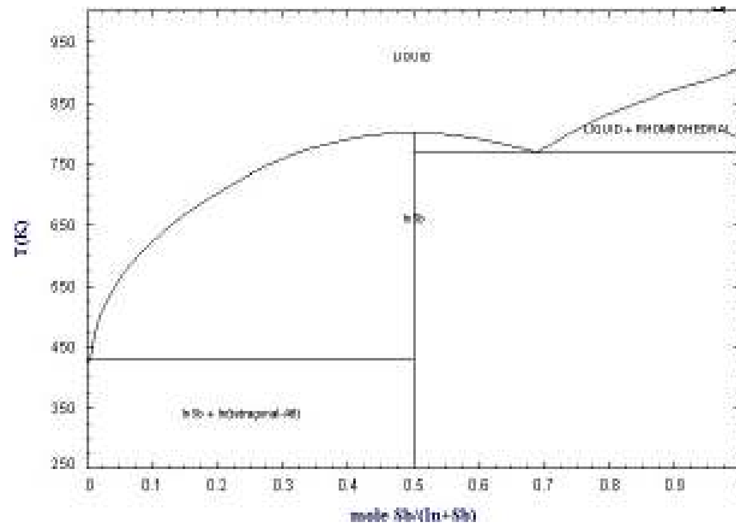

Figure 5.15 The binary phase diagram of the In-Sb system.

substrates coated with large indium droplets (indium-rich region) also has already been demonstrated.

5.3.2 Based on antimony droplet

For group III metals, both Ga and In display very low melting points, normally far below typical growth temperatures of materials like GaSb, InSb, GaAs, InAs, etc.

Therefore, there is no solubility limit of gallium and indium in Au at these growth temperatures. For the group-V materials N, P and As, no binary Au-V phase or ternary Au-III-V phases have been reported to be stable at temperatures below around 600 ^{o}C. However, Sb is an exception. There exists a simple eutectic system between Sb and Au with eutectic point at about 350 ^{o}C. Confirming this, N, P and As have never been observed in seed particles on nanowires by ex-situ post-growth characterization, which does not hold true for Sb. This implies that the growth mechanism of material like InSb, GaSb nanowires may possibly be related to both group III-Au and Sb-Au alloys. Consequently, InSb and GaSb nanowires are expected to be obtained based on group III or antimony droplets theoretically, and there already many related reports could be found in literature. In the work performed above, we have demonstrated that InSb nanowires have been synthesized based on In droplets by a decomposition of TMIn source prior to growth. In this paragraph, a deposition of TMSb source was first performed, aiming to acquire InSb nanowires with the principle of self-nucleation from antimony droplets.

For the process, it is slightly different from previous growth. Considering the limited decomposition rate of TMSb below 450 ^{o}C, the TMSb source was opened immediately when the chamber was heated to 500 ^{o}C, and the annealing treatment was performed simultaneously. Thus, antimony vapors are generated and get deposited onto a substrate first for 5 mins. These results in a condition where indium vapors in antimony-rich composition are transported over antimony clusters. The reactor was then cooled down to growth temperature and TMIn source was turned on to initiate the growth. The input V/III ratio was set at 30 and the growth duration was

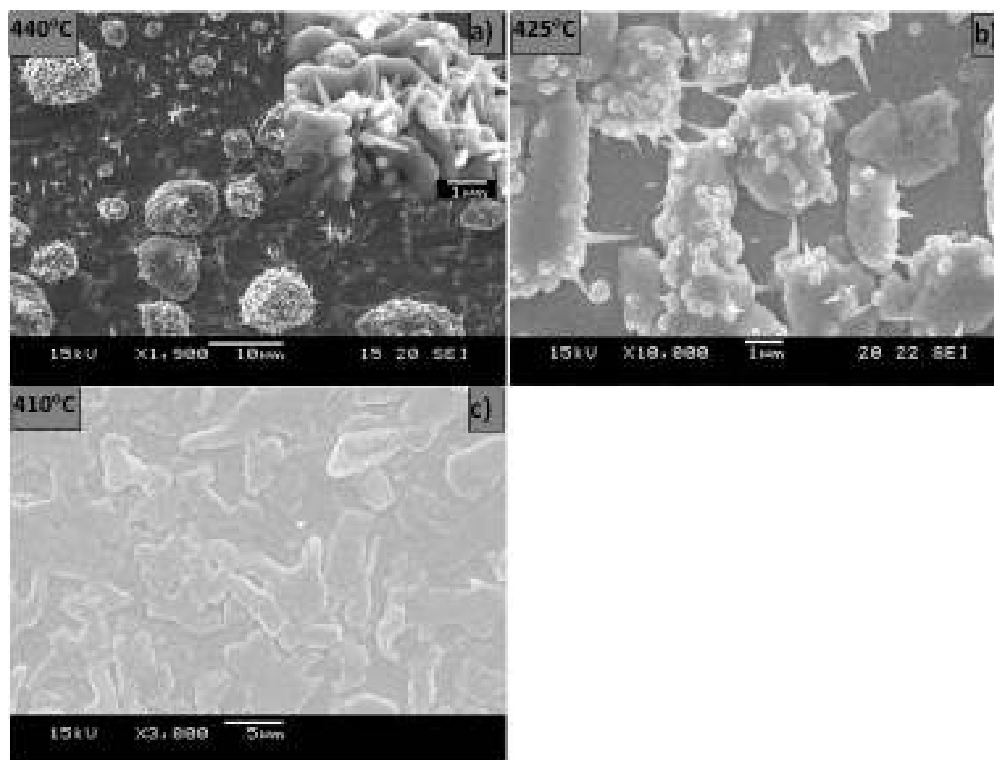

Figure 5.16 Top view SEM photograph of InSb nanowires synthesized at different temperatures.

30 mins. As a result, a group of samples prepared at different temperatures were made by MOCVD. It can be seen that InSb nanowires in tapered profile could be observed in Figure 5.16 (a) and (b), for growth temperature at 440 ^{o}C, 425 ^{o}C, respectively. Further decreasing growth temperature to 410 ^{o}C (Figure 5.16 c)) resulted in no detectable nanowire growth, suggesting that there is a mid-range temperature nanowire epitaxy.

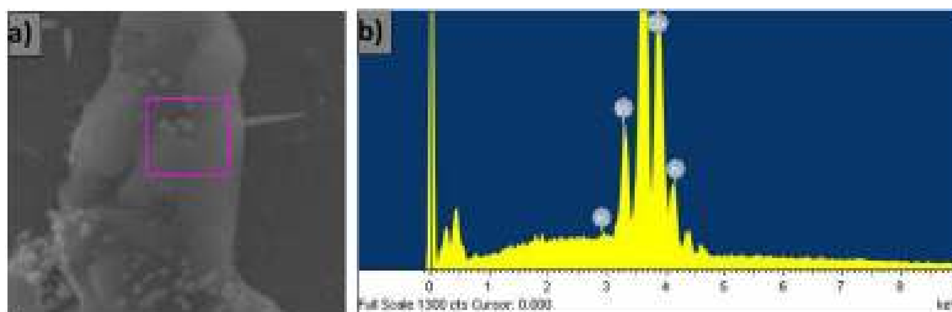

Figure 5.17 (a) SEM photograph of selected area EDX measurement on the sample grown at 425 ^{o}C. (b) The corresponding EDX spectrum.

According to the images, the tapered InSb nanowires are grown based on an agglomeration of material resulting from the decomposition and accumulation of organic source. To investigate the content, selected area EDX measurement on the chunk was performed, and the spectrum is as shown in Figure 5.17 (a) and (b). The result indicates that the content of the bulk material is mainly composed of antimony and small amount of indium. The atomic percent of Sb and In are 84.5% and 15.5%, respectively. There was no gold detected in the spectrum, perhaps being encompassed by external materials.

It is apparently that the underlying mechanism here is distinct from previous growth. To analyze the composition variation, the line mapping of EDX measurement has been done along the nanowire. The scanning direction is from the tip to the root of a single wire as shown in Figure 5.18 (a) and the curve of the content of elements changing along the nanowire is given in Figure 5.18 (b). At the root of the nanowire,

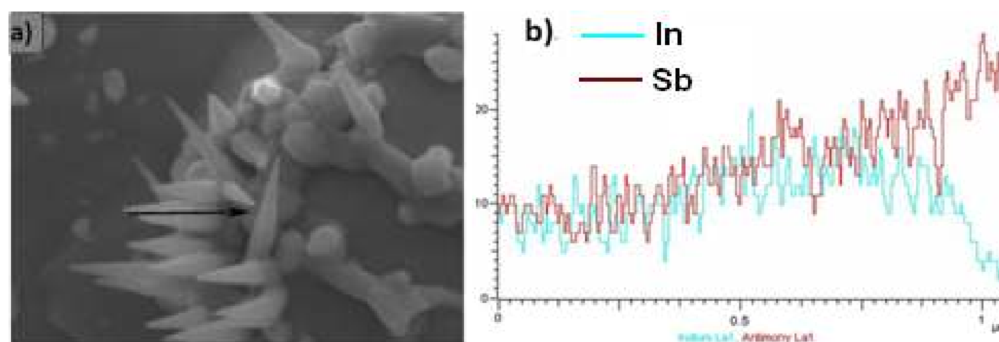

Figure 5.18 (a) SEM photograph of the EDX line scan of a single InSb nanowire, and (b) the curve of antimony and indium content along the nanowire.

element Sb is dominant, aslo with very small amount of In. With the growth going on, the incorporation of In increases dramatically, which makes the Sb/In ratio move to the stoichiometric point quickly.

The line scan tells that with the assistance of Au particles, the InSb nanowires obtained here is likely based on self-nucleation of Sb. Intentionally introducing TMSb source into reactor in advance will lead to substantial deposition of Sb, and consequently a Sb rich surface. Due to the existence of Au particles dispersed early, Sb will combine with Au particles by forming Sb-Au alloy. At 500 ^{o}C, it will form a Sb-Au alloy with about 75% Sb, as indicated by the Au-Sb binary phase diagram in Figure 5.19. With the reactor temperature dropping down to growth point, certain amount of Sb may precipitate from the alloy along the line of liquid phase. Indium source was then introduced into the chamber, and some indium atoms would be absorbed by the Sb-Au alloy. As shown in Figure 5.15, the In-Sb phase diagram indicates a 21 at% eutectic solubility of indium in antimony in the antimony-rich region. With indium source involved in, spontaneous nucleation may happen in the

Sb alloy, leading to the formation of InSb nanowires. The presence of excessive antimony at the root is a clear evidence of bulk self-nucleation growth of InSb nanowires here. The growth temperatures we set for this series of samples are 440 ^{o}C, 425 ^{o}C and 410 ^{o}C, respectively. From the SEM images in Figure 5.16, InSb nanowire could not be obtained at temperature of 410 ^{o}C. It is because such a temperature is much lower than the eutectic point shown in In-Sb phase diagram at Sb rich side, which may lead to failure of self-nucleation and the growth of InSb nanowires.

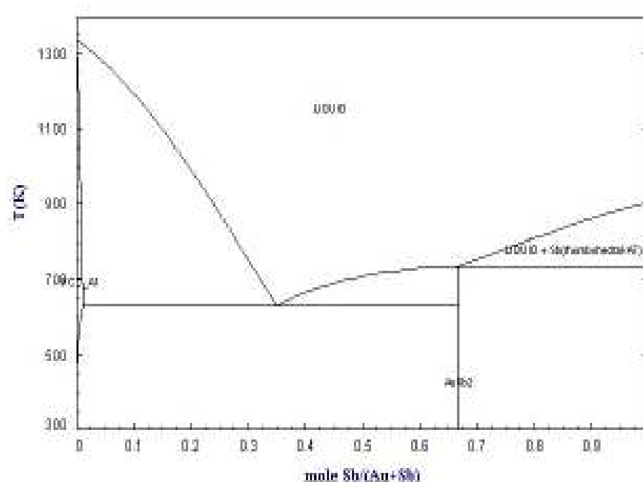

Figure 5.19 The binary phase diagram of the Au-Sb system.

5.4 Summary

In this chapter, InSb nanorods were first acquired on InSb (100) substrate. After that, free-standing InSb nanowires were realized on InSb (111) B substrate.

Clear dependence of morphologies on temperature could be observed from a series of samples. The growth rate of InSb nanowires increases first and then goes down with decreasing V/III ratio. Moreover, the diameter of the nanowires increases with the

increasing group III sources, which means that the lateral growth of InSb naowires should be favored at high indium molar fraction. Based on the analysis, the InSb nanorods and nanowires synthesized here were precipitated from supersaturated solid $AuIn_2$ particles, and the underlying mechanism of the production matches the VSS situation. In addition, Self-nucleation of InSb nanowires based on both indium and antimony droplets have been demonstrated.

CHAPTER 6. GROWTH OF INSB NANOWIRES ON GAAS AND SI SUBSTRATES

Up to now, most of the fabrication of InSb nanowire was performed epitaxially on InSb substrate. Except several papers about InSb-containing heterostructure nanowires, there is little report on single InSb nanowires directly hetero-epitaxially grown on other III-V substrates. One of the primary reasons is the large lattice mismatch of InSb to materials like GaAs (12.6%) and Si (19.3%). However, the properties like high conductivity, fragility and high cost suggest that it is significant for InSb being integrated successfully into other material systems. Much endeavor has already been made on the realization of high quality bulk InSb hetero-epitaxially on GaAs or Si substrates, and relative success could be achieved by introducing a buffer layer [24-25]. But the hetero-epitaxial growth of InSb nanowires is a totally brand new challenge for researchers.

In this project, we tried to realize InSb nanowires hetero-epitaxially on GaAs and Si substrates by MOCVD. The dependence of InSb nanowire growth on V/III ratio, and temperature was studied carefully. The underlying growth mechanisms of InSb nanowire on different substrates were also discussed in detail.

6.1 InSb nanowires on GaAs (111) B

6.1.1 Growth and characterization

Before inserting to the reactor, all substrates were cleaned carefully in ethanol to remove organic residues and in hydrofluoric acid to eliminate oxides on the surface. After rinsing, the substrates were coated with Au aerosol particles as growth

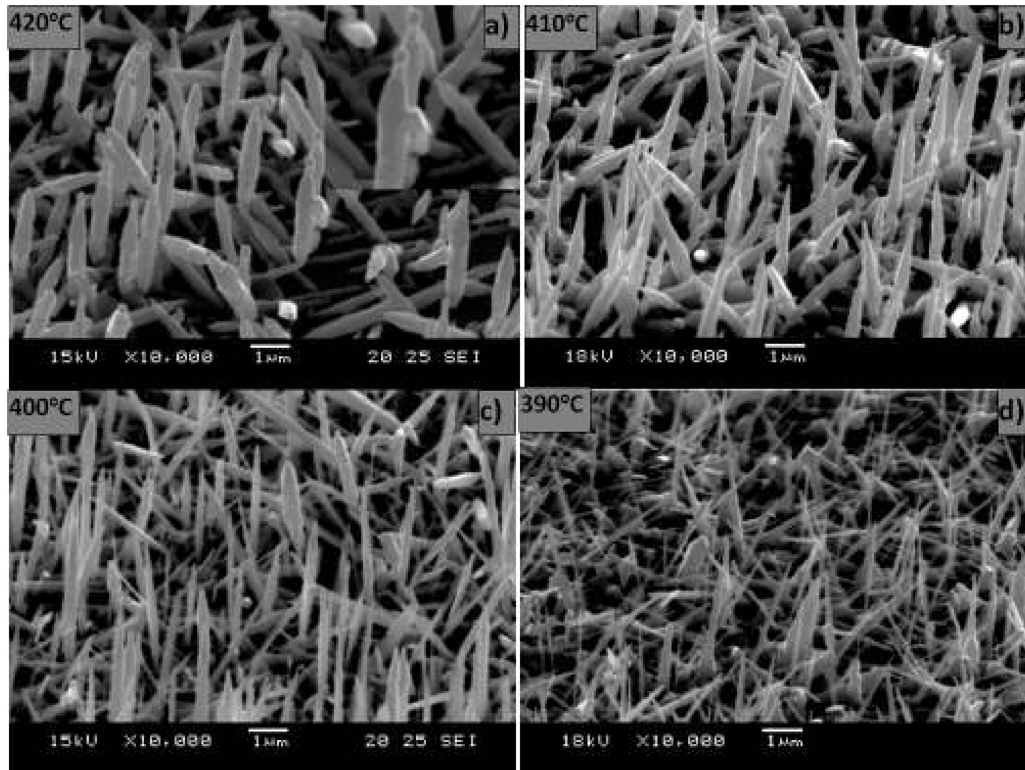

Figure 6.1 45° angle view SEM images of InSb nanowire dependent on growth temperature from 390 ^oC to 420 ^oC with a fixed V/III ratio of 45.

seeds with the size around 40 nm. After all the treatments, the samples were then immediately placed to the chamber to avoid exposure to the air. Before the growth, the samples were normally annealed at 500 ^oC in H_2 atmosphere for 8 mins. A range of V/III ratio from 30 to 60 was adjusted to see the influence on the growth. The influence of growth temperatures ranging from 390 to 420 ^oC was also evaluated. The growth time was typically set at 30 mins.

The SEM images of InSb nanowires grown on GaAs (111) B substrates at different temperatures with a V/III ratio of 45 are shown in Figure 6-1 (a) to (d). It is seen that vertical InSb nanowires have been hetero-epitaxially obtained on GaAs substrate. High resolution X-ray diffraction (HRXRD) has been performed to see the quality of wires obtained. We chose the sample prepared at 410 ^{o}C as an example and GaAs substrate was also measured as a reference. The results were given in Figure 6.2. In comparison to GaAs substrate, peaks referring to InSb (111), (444) were observed on the grown sample, indicating that the InSb nanowires were growing along (111) direction. No diffraction peaks to other directions were detected, which demonstrates quite good quality of wires acquired here.

As indicated by the inset image in Figure 6-1 (a), an alloy tip could be observed at the head of nanowires, suggesting a mode of tip-leading growth. The average diameter increases with the increasing temperature, as shown in Figure 6.3, which suggests that lateral growth is favored at higher temperature. With increasing the temperature, the growth rate increases first and then decreases, indicating an optimum growth window of temperature parameter.

As shown by SEM pictures, the morphologies of InSb nanowires obtained here show the tapering shape. The lower section exhibits larger diameter than the upper section, which is distinct from the tip-leading wires on InSb substrate. The degree of tapering has a dependence on growth temperature. It decreases when lowering the temperature. This observation matches the reported results of InAs nanowires [223-224]. The morphology of tapering demonstrates that in addition to the vertical growth determined by catalyst, the nucleation on the lateral facets also takes place at high

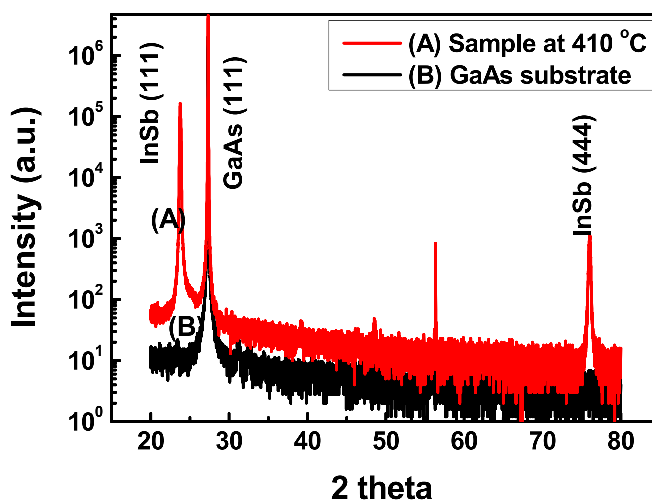

Figure 6.2 XRD spectra of InSb nanowires grown at 410 °C. GaAs substrate was also measured for reference.

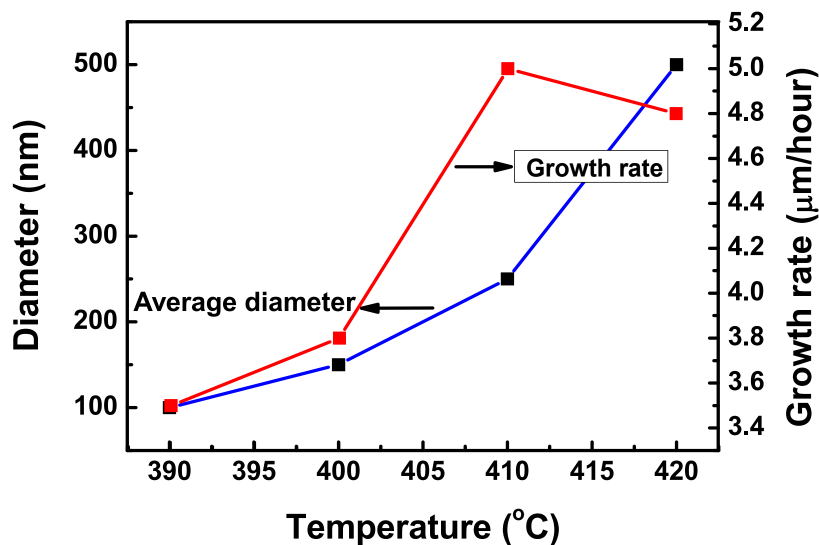

Figure 6.3 InSb nanowire diameter and growth rate as a function of temperature from 390 °C to 420 °C.

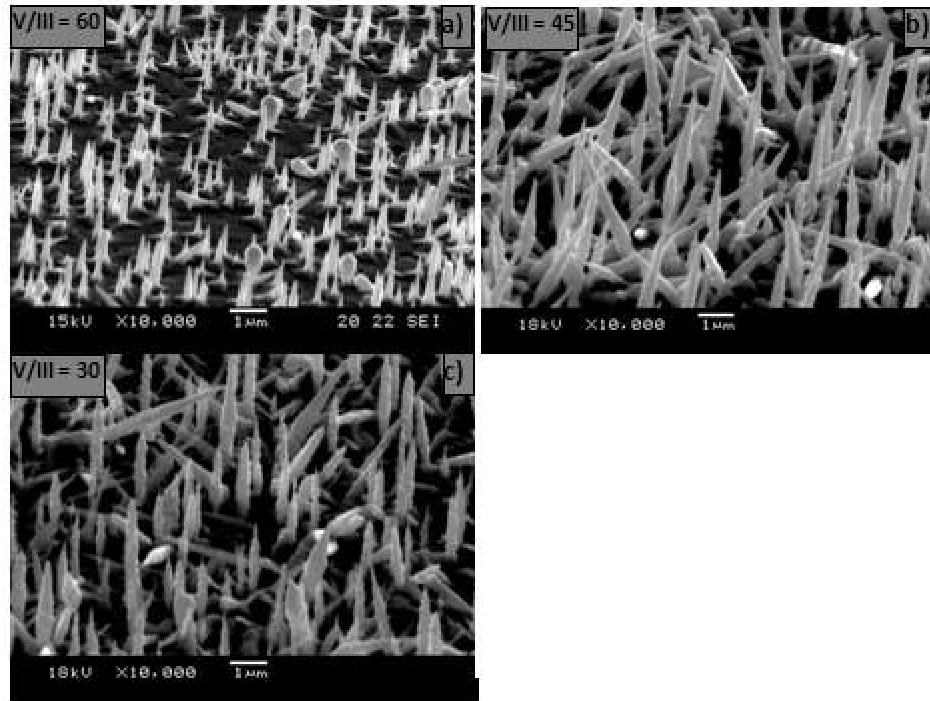

Figure 6.4 SEM images of samples prepared with different V/III input ratios at a fixed temperature of 410 ^{o}C.

temperatures. To reduce the lateral growth, the temperature is supposed to be low. On the other hand, the tapering shape may be related to diffusion of indium on the nanowire facets. It is supposed to happen when the mean diffusion length $<\lambda_{diff}>$ of species on the lateral nanowires facets becomes smaller than the height, which makes indium adatoms no possible to reach the catalyst and thus participate in the growth of nanowire side facets. Figure 6.4 (a) to (c) gives the SEM images of samples prepared with different V/III input ratios at a fixed temperature of 410 ^{o}C. It is seen that the tapering decreases as reducing the V/III ratio.

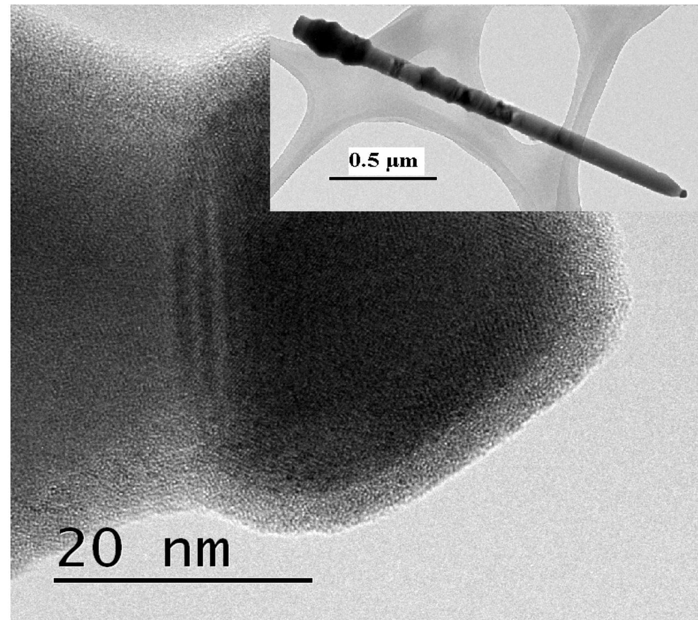

Figure 6.5 High resolution transmission electronic microscopy image of the head tip of a single InSb nanowire.

This demonstrates that the tapering shape can be suppressed by maintaining the TMIn molar fraction. The length of the nanowires also first increases and then decreases with increasing the V/III ratio, suggesting a growth window in term of V/III ratio.

6.1.2 Mechanism and discussion

The observation of tapering InSb nanowires on GaAs substrate implies a different growth process from that on InSb substrate. This suggests that much effect should be

resulted from the lattice mismatch between the nanowire and the substrate. It is noted that the diameter of nanowires are limited by the lattice mismatch. The nanowires will be free of defects below a certain critical diameter, D_o, which is generally shown to be inversely proportional to lattice mismatch. Above the critical diameter, misfit dislocations and defects may appear, which has the effect on reducing the formation energy of the nanowires [225]. The overall formation energy of the nanowire is given as:

$$\mathbf{E_n = E_r + E_d^n,} \qquad (6.1)$$

Where E_l is residual lattice strain energy and E_d^n is the dislocation energy, both of them are lattice mismatch dependent.

A model has been developed to determine the D_o allowable for a given mismatch by Ertekin et al. It suggests that the D_o is in the range of 20-50 nm for InAs-InP heterostructural nanowires. Figure 6.5 gives the high resolution transmission electronic microscopy (HRTEM) image of a single InSb nanowire. The size of the head alloy is around 40 nm, which is close to the original size of the Au nanoparticle adopted for the growth. Misfit dislocation could be observed at the interface between the alloy and the wire side. This suggests that the D_o of InSb nanowire on GaAs substrate is likely to be below 40 nm. In addition, indicated by the inset image, rectangular blocks of twin structures along can be observed along the axis of the wire, which is suggested to be due to the small energetic differences for hexagonal or cubic stacking sequences in the (111) directions.

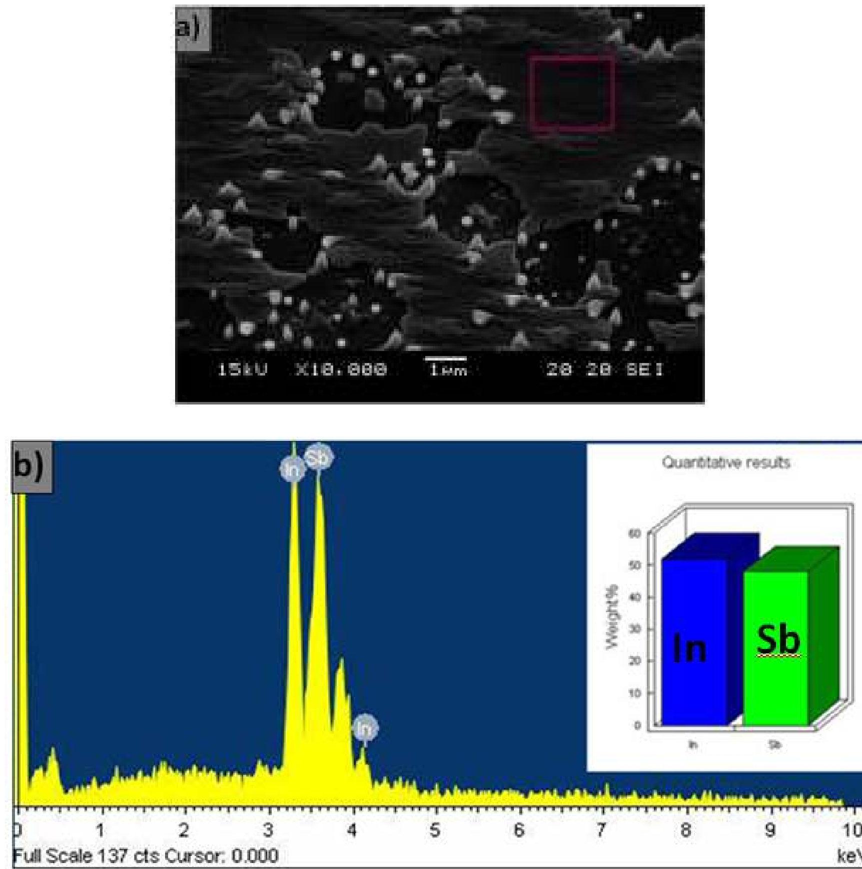

Figure 6.6 (a) SEM photograph of selected area EDX measurement on the sample grown for 3 mins, at 410 ^{o}C, and with a V/III ratio of 40. (b) EDX spectrum of the sample.

However, the growth of epitaxial heterostructures does not depend solely on accommodation of mismatch. It is reasonable that physical surface processes must be considered in order to understand the growth. Figure 6.6 gives a SEM image of a sample grown for 3 mins at 410 ^{o}C, and with a V/III ratio of 40. It is seen that accompanying the InSb nanowires at initial stage, a very thin layer of InSb is also formed, demonstrating the competition between the growth of nanowire and bulk material. During the growth of nanowires, axial and lateral growth may be always treated as ‘‘competing’’ processes. With the assistance of Au particle as a sink, once

the growth material is dissolved into the Au particle, it cannot diffuse away and will contribute to axial growth. Any material which cannot diffuse far enough to reach the particle will lead to lateral growth.

6.2 InSb nanowires on Si

6.2.1 Growth and characterization

The integration of III-V semiconductors with Si technology is a long sought goal for the semiconductor industry. This is not only of great significance to the application of III-V semiconductors like light-emitting diodes and optoelectronics, but also to overcome the limitations of the unideal Si material like the low efficiency in light generation, the lack of a versatile heterostructure technology, etc. Till now, there has been much effort made about epitaxial growth of InSb on Si [24, 25, 226-228]. However, work on pursuing InSb nanowires on Si substrate, is quite rare. In this part, we show that InSb nanowires can be grown hetero-epitaxially on Si substrate. The process of experiment is just similar to above elaboration. The substrate used is Si (100).

Figure 6.7 presents the SEM images of three types of InSb nanowire designated a, b, and c, which are synthesized at 400 ^{o}C, 410 ^{o}C and 420 ^{o}C, respectively. The samples are made at a fixed V/III ratio of 45. It is seen that the InSb nanowires have successfully obtained on Si substrate. However, except the sample at 410 ^{o}C, the yield

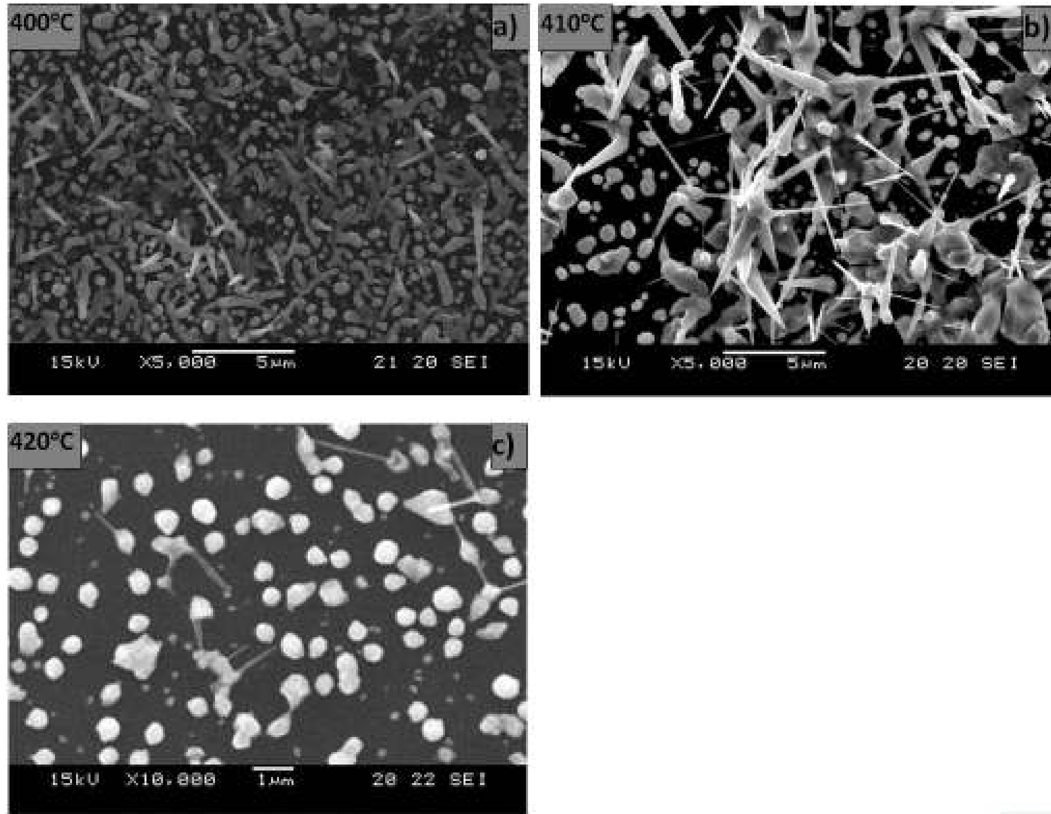

Figure 6.7 SEM images of the dependence of samples grown at 400 ^{o}C, 410 ^{o}C and 420 ^{o}C on Si substrate.

of InSb nanowire is low. This suggests that InSb nanowire on Si has a very narrow growth window in view of temperature. At higher or lower temperatures, most of the products are in the form of spherical balls, and only a few number of tiny InSb nanowires could be observed by precipitating from the balls.

6.2.2 Mechanism

To the best of our knowledge, there is no report for the InSb nanowires grown on Si substrates. For the phenomenon observed above, the model developed for Si

nanowhiskers by E .I. Givargizov is helpful [229]. In kinetic studies, the crystallized rate is usually evaluated as a function of driving force, e.g. of supersaturation. Based on a combination of the Gibbs-Thomson equation and some kinetic law of growth, a method was suggested for the determination of the supersaturation and of the kinetic coefficients of crystallization. According to the Gibbs-Thomson effect, the decrease of supersaturation as a function of whisker diameter do can be given as:

$$\Delta\mu = \Delta\mu_o - 4\alpha\Omega/d_o, \qquad (6.2)$$

Where $\Delta\mu$ is the effective difference between the chemical potentials of Si, InSb in the vapor phase and in the whisker, $\Delta\mu_o$ is the same difference at a plane boundary ($d_o \rightarrow \infty$), α is the specific free energy of the whisker surface, and Ω is the atomic volume of primitive cell of the material. Obviously, there is a critical diameter at which $\Delta\mu = 0$ and the whisker growth stops completely. Those whiskers with diameters smaller than the critical diameter will stop growing. As indicated by the Figure 6.7 (a), the mean diameter of the InSb nanowires is around 50 nm, which means the growth rate of the product with diameter below 50 nm is likely to be zero, or it could be said that InSb nanowires below 50 nm can not precipitate from the In-Au-Sb alloys,

At the thermodynamic equilibrium state, the stability of a liquid droplet depends on the degree of supersaturation. For a liquid droplet in its own vapor, the stability can be described by $d_{min} = (4a\Omega)/(kT \ln S)$. Here, S is the degree of supersaturation (the chemical potential $\Delta\mu = kT \ln S$). The d_{min} is inversely proportional to the temperature, which implies that InSb nanowires with larger diameter could be

obtained at lower temperature. This matches the observation as indicated in Figure 6.7 (a) to (c).

The InSb nanowires shown in Figure 6.7 (b) are in spiky, polycrystalline structure, which is supposed to be due to the inability of the larger diameter nanowires to accommodate the strain between the InSb and silicon without forming misfit dislocations. Figure 6.8 gives a SEM picture of InSb nanowires at higher magnification factor, from which we could find InSb nanowires with an interesting structure that the diameter of the nanowire is not uniform along its length. These are diameter-modulated (DM) nanowires, which are not observed in the growth on InSb and GaAs substrates, or InSb nanowires already reported in other groups.

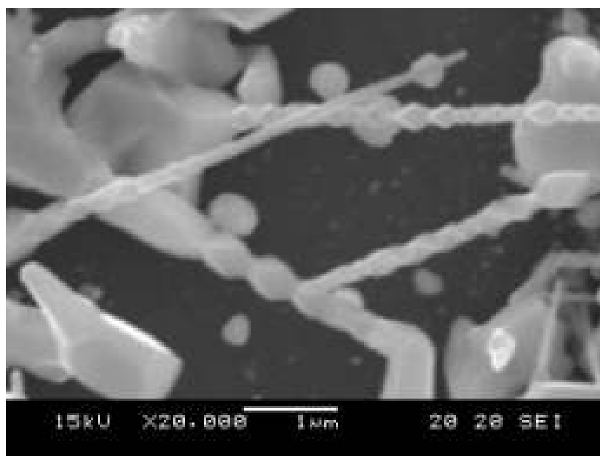

Figure 6.8 Top view SEM picture of InSb nanowires at a higher magnification

This observation may imply a different underlying growth process of InSb nanowires on Si substrate. In previous studies, Jie et al. have reported work about Zn_2SnO_4 nanowires with DM structure [230]. They attributed the diameter modulated feature to the disturbance of the vapor concentration (Zn, Sn, O), which consequently

changes the diameter of the catalyst alloy droplets and the growth velocity of nanowires, and thus the variation of diameter along the nanowires. In our work, the formation mechanism of the DM InSb nanowires here is similar to the work reported by Jie et al. As mentioned in previous discussion, for the In-Au-Sb system, stable pseudobinary systems like AuIn-InSb, $AuIn_2$-InSb would form droplets, under suitable conditions. As shown in Figure 6.9, a gold nanoparticle absorbs In and Sb atoms from the vapor and forms an alloy droplet. After more In and Sb adtoms were dissolved in the droplets, the pseudobinary In-Au-Sb phase would reach the supersaturated state and solid InSb subsequently precipitates from the droplets to form nanowires. When vapor disturbance induces change in the In and (or) Sb concentration near the alloy droplet, the size of the droplet shrinks and the nanowire diameter decreases.

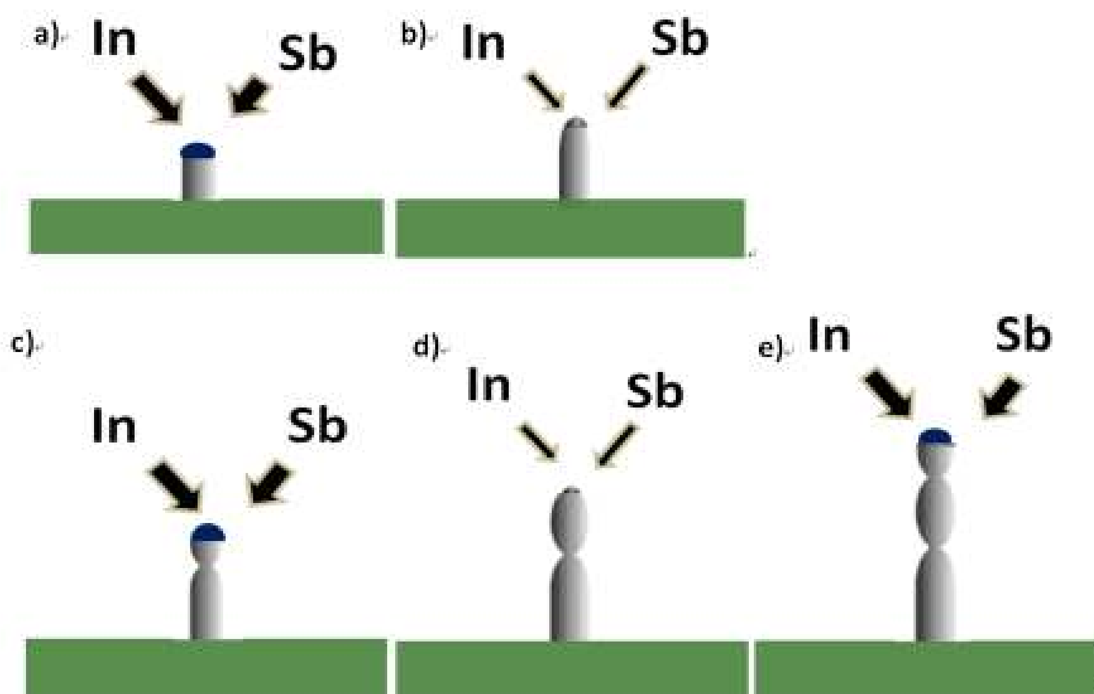

Figure 6.9 Schematic illustration of the growth process of a DM InSb nanowire on Si substrate. (a) Au nanoparticle absorbs In and Sb atoms from the vapor and forms an alloy droplet, then the reaction between In and Sb initiates the growth of InSb nanowire, (b) Disturbance induced decrease of In and Sb concentration near the alloy droplet reduces the size of the droplet and results in a decrease of the nanowire diameter; (c) Small size alloy droplet absorbs fewer atoms from the vapor, which induces the increase of the In and Sb concentration near the alloy droplet and finally results in the increase of the droplet size and nanowire diameter; (d) The size-resumed alloy droplet draws more atoms from the vapor, which reduces the In and Sb concentration and the nanowire diameter again; and (e) Continuation of the steps depicted in steps c and d forms a InSb DM nanowire.

A small size alloy droplet absorbs less atoms from the vapor, which induces an increase of the indium and antimony concentration near the alloy droplet and finally causes the increase of the droplet size and nanowire diameter. The size resumed alloy droplet draws more atoms from the vapor, which reduces indium and antimony concentration and the nanowire diameter again. This mechanism suggests that a disturbance of the vapor concentration triggers a vapor density oscillation near the alloy droplet and finally forms an InSb DM nanowire.

However, this fluctuation model is hard to explain why no nanowire with the same morphology was obtained on other substrates like InSb, or GaAs. There is need to find why the vapor density oscillation near the alloy droplet affects growth on Si substrate rather than, InSb and GaAs substrates. It is noted that the diameter fluctuation is attributed to change in the seed particle volume, wetting angle or a

combination of both. Most importantly, greater diameter fluctuation is possible for materials grown over a large rage of supersaturation, which requests significant change in wetting angle. The change in wetting angle is induced by variation of surface energy, which can be altered by seed particle composition. As a result, the realization of diameter fluctuation needs the seed material with larger change in wetting angle.

Wetting angle quantifies the wetting ability of a solid surface, which is a function of the surface energies of the solid-liquid interface (σ_{SL}), the solid-gas interface (σ_{SV}), and the liquid-gas interface (σ_{VL}), which are as indicated in Figure 6. 10. From the SEM images in Figure 6.7, it is seen that the product would like to form sphere particles, which indicates a weak wetting ability of the alloys on Si substrate, and

Figure 6.10 Illustration of force balances at the triple-phase boundary.

consequently a large wetting angle. The applied forces would reach balance at a steady state and the equation is expressed as follows [231]:

$$\sigma_{SL} = \sigma_{SV}\cos(\alpha) - \sigma_{VL}\cos(\beta) \qquad (6.3)$$

where α is the inclination angle between the vapor/solid and liquid/solid interfaces. At steady-state, $\alpha = 90$, the equation 6.3 could be reduced to:

$$\sigma_{SL} = -\sigma_{VL}\cos(\beta) \qquad (6.4)$$

This equation indicates that a lower ratio of σ_{VL}/σ_{SL} would lead to a larger wetting, which makes the nanowire diameter more sensitive to the change in surface energy. Therefore, selecting seed materials with larger surface energy (σ_{SL}) would facilitate greater changes in nanowire diameter. It is known that the σ_{SL} is dependent on many factors like crystal structure, temperature, etc [232], and it should have larger value in heterogenous case (on Si substrate) than homogeous case (on InSb substrate). Based on above discussion, due to the large wetting angle, the seed particle of InSb nanowires on Si substrate may have a wide range of supersaturation, and consequently leading to the fluctuation in nanowire diameter.

6.3 Summary

In this chapter, much endeavor has been paid on the synthesis of InSb nanowires on GaAs (111) substrate. The alloy tip at the head of nanowires suggests a mode of tip-leading growth. The dependence of diameter and growth rate on temperature also has similar trend to the growth on InSb substrates. However, the tapering InSb nanowires on GaAs substrate implies a different growth process from that on InSb substrate, which suggests that the lattice mismatch between the nanowire and the substrate has significant effect on the wire formation and growth.

Moreover, InSb nanowires have been first successfully made hetero-epitaxially on Si substrate. The outcomes indicate that InSb nanowires on Si have a very narrow growth window in term of temperature. The morphologies of the production in spiky and polycrystalline structure are probably owing to the inability of the larger diameter nanowires to accommodate the strain between the InSb and Si. SEM image with high magnification indicates that the InSb nanowires obtained on Si have an interesting DM structure, which is not observed from the nanowires on InSb or GaAs substrates. We attributed this phenomenon to the disturbance of the vapor concentration (In, Sb), which may change the diameter of the catalyst alloy droplets and thus the growth rate of nanowires.

CHAPTER. 7 CONCLUSIONS

7. 1 Conclusions

In conclusion, MOCVD growth of InSbN alloys, and InSb nanowire has been investigated in this project. We have grown and characterized InSbN alloys on different substrates, and the extension of InSb band gap to longer wavelength has been realized. We have realized vertical InSb nanowires on four kinds of substrates, and underlying mechanisms are studied based on variety of characterizations. The major conclusions are listed as following:

(i) High quality InSb epilayers were grown epitaxially on InSb (100) by MOCVD. Low temperature photoluminescence spectra of the samples revealed that in addition to the main band-to-band emission around 5.4 μm, an emission peak around 5.87 μm was also observed. Our results indicated that the low energy emission peak was originated from the antisite Sb_{In} defects which can be removed by reducing the V/III ratio.

(ii) For the $InSb_{1-x}N_x$ alloys on InSb (001), an obvious red shift of the PL peak has been observed in InSbN alloy according to the result of PL measurements. The distinction between the two observations is due to the band-gap narrowing effect (BGN) from the high carrier concentration. X-ray photoelectron spectroscopy shows that in addition to except substutional N_{Sb}, and other N forms like N_{In}, interstitial N and molecular N_2 also exist in the as grown films.

(iii) InSbN alloys on GaAs (100) substrate were made by MOCVD. Post growth annealing treatments with different periods of time and temperatures were carried out to improve the alloy quality and study the effect on the alloy properties. PL results indicated that a broad peak around 7.2 μm related to near band edge emission could be observed at 10 K, indicating that the cut-off wavelength was prolonged to a longer value due to the N incorporation. For the InSbN alloys on GaSb substrate, PL measurement indicated that the band gap wavelength of the alloys was prolonged to 6.3 μm by the incorporation. Besides, another peak around 8.3 μm was also detected, and the peak intensity is comparable to the main band emission, which is a new phenomenon and may bring novel applications, such as long waveleng photodetection.

(iv) By using gold as catalyst, we have synthesized lateral InSb nanorods and vertical InSb nanowires on InSb substrate via a vapor-solid-solid (VSS) growth mechanism. There is a strong dependence of InSb nanowire growth rate and diameter on growth parameters like temperature, V/III ratio. With the characterizations and discussion, the InSb nanorods and nanowires synthesized here should be grown from a supersaturated solid $AuIn_2$ particle. Furthermore, InSb nanowires based on both indium and antimony droplets have been demonstrated, respectively.

(v) InSb nanowires also have been achieved hetero-epitaxially on GaAs (111) B substrate. The influence of parameters on the morphology has been studied carefully. The tapering shape of the InSb nanowires on GaAs

substrate implies a different growth process from that on InSb substrate, probably because of the lattice mismatch between the production and the substrate.

(vi) Despite the differences such as quite large lattice mismatch, thermal expansion coefficients and anti-phase domain formation, InSb nanowires have been successfully made hetero-epitaxially on Si substrate for the first time. Distinct from the nanowires on InSb or GaAs substrates, the InSb nanowires obtained on Si have an interesting DM structure, likely due to the disturbance of the vapor concentration (In, Sb).

7. 2 Recommendations

The recommendations for future research are proposed as the following:

(i) Additional growth by changing growing conditions such as V/III ratio, and pressure will be needed to further investigate the defects and their effect on the optical and electrical properties of InSb on InSb substrate. $InSb_{1-x}N_x$ alloys have been successfully prepared on InSb substrate, however, the N concentration in the alloy is still not large enough to extend the cut-off wavelength to the long wavelength region. More work needs to be done in order to incorporate more N into InSb and get longer cut-off wavelength in the end.

(ii) Quite high N incorporation has been achieved for $InSb_{1-x}N_x$ alloys on both GaAs and GaSb substrates. However, there is still much room for the improvement on the film quality. Besides, XPS spectra indicate that the N-Sb bonding occupies the most part of the total N in the

alloys. Therefore, the percentage of the substitutional N_{Sb} should be enhanced in order to get longer cut-off wavelength of $InSb_{1-x}N_x$ alloys.

(iii) The growth and mechanism of InSb nanowires on different substrates like InSb, GaAs, Si have been studied carefully in this project. However, much work is still required to better understand the underlying mechanism for the formation of InSb nanowire. Besides, growth for InSb nanowire in shape, diameter, length, etc, needs to be controllable, which is not only significant for understanding the properties of InSb nanowire, but also for future actual application in nanoelectronic devices.

(iv) Finally, elements like Ga, As, N, etc, are recommended to add into InSb, aiming to adjust the band gap of InSb nanowire. This may expand the versatility of application of InSb nanowire in future nanoelectronics.

AUTHOR'S PUBLICATIONS

1. **Jin, Y. J.**, Zhang, D. H., Chen, X. Z., Tang, X. H., "Sb antisite defects in InSb epilayers preparedby metalorganic chemical vapor deposition", Journal of Crystal Growth, vol. 318, p. 356-359 (2011).
2. **Jin, Y. J.**, Zhang, D. H., Tang, X. H., Teng, J. H., "Growth and properties of $InSb_{1-x}N_x$ alloy on GaSb substrate by MOCVD", accepted by Applied Physics A.
3. Y. Wang, D. H. Zhang, **Y. J. Jin**, "Bonding and diffusion of nitrogen in the InSbN alloys formed by two-step ion implantation", Applied physics letter, Vol. 101, p. 021905 (2012).
4. **Jin, Y. J**, Wang, Y., Zhang, D. H., Tang, X. H., Zhang, B. L., "Epitaxial growth of high quality $InSb_{1-x}N_x$ by MOCVD", Source: 2008 IEEE Photonics Global @Singapore (IPGC) (2008).
5. , **Jin, Y. J**., Tang, X. H., Chen, X. Z., Zhang, D. H., "Properties of InSb (N) epilayers grown by metalorganic chemical vapor deposition Photonics Global Conference", Photonics Global Conference, PGC (2010).
6. Chen, X. Z., Zhang, D. H., **Jin, Y. J**., Zhang, S., "Electrical & optical properties of Mg-doped narrow band-gap InSbN P-N junction", 2010 Photonics Global Conference (2010).
7. Zhang, D. H., Yan, C. C., Chen, X.Z., **Jin, Y. J.**, Li, D. D., "Nanostructured materials for sensing and imaging", Proceedings 2010 OSA-IEEE-COS Advances in Optoelectronics and Micro/Nano-Optics (2010).

8. **Jin, Y. J.**, Tang, X.H., Teng Jinhua, Zhang, D. H., "InSbN alloys Grown by Metal-organic chemical vapor deposition for long wavelength detection", to be submitted.
9. **Jin, Y. J.**, Zhang, D. H., Tang, X. H., Chen, X. Z., Teng, J. H., Properties of InSbN alloys on GaAs substrate prepared by MOCVD for long wavelength applications", to be submitted.
10. **Jin, Y.J.**, Zhang, D.H., Tang, X. H., Teng J. H., "Growth and characterization of InSb nanorods on InSb (100) substrate by MOCVD", to be submitted.
11. **Jin, Y. J.**, Zhang, D. H., Tang, X. H., Teng J. H., "The growth mechanism of vertically InSb nanowires on InSb (111) substrate by MOCVD", to be submitted.
12. **Jin, Y. J**., Zhang, D. H., Tang, X. H., Teng J. H., "The growth of hetero-eptitaxially InSb nanowires on GaAs (100), (111) substrates by MOCVD", to be submitted.

BIBLIOGRAPHY

1. T. D. Veal, I. Mahboob, and C. F. McConville, Phys. Rev. Lett., Vol. 92, p.136801 (2004).
2. K. T. Huang, C. T. Chiu, FL M. Cohen, and G. B. Stringfellow, J. Appl. Phys., Vol. 75, p. 2857, (1994).
3. H. Y. Deng and N. Dai, Phys. Rev. B., Vol. 73, p. 113102 (2006).
4. B. Joukoff, A.M. Jean Louis, J. Cryst. Growth, Vol. 12, p. 169-172 (1972).
5. J. J. Lee, J. D. Kim, and M. Razeghi, Appl. Phys. Lett., Vol. 70, p. 3266 (1997).
6. J. J. Lee, J. D. Kim, and M. Razeghi, Appl. Phys. Lett., Vol. 73, p. 602 (1998).
7. B. N. Murdin and A. R. Adams, Appl. Phys. Lett., Vol. 81, p. 256 (2002).
8. T. Ashley, B.N. Murdin, C.R. Pidgeon, Solid-State Electronics, Vol. 47, p. 387-394 (2003).
9. T. D. Veal, I. Mahboob, C. F. McConville, and T. Ashley, Appl. Phys. Lett., Vol. 83, p. 1776 (2003).
10. H. T. Pham and S. F. Yoon, K. H. Tan, Appl. Phys. Lett., Vol. p. 092115 (2007).
11. K P Lim, S F Yoon, and H T Pham, J. Phys. D: Appl. Phys., Vol. 42, p. 135419 (2009).
12. I. Mahboob, T. D. Veal, and C. F. McConvillea, J. Appl. Phys., Vol. 96, p. 4935 (2004).

13. D. H. Zhang, W. Liu, Y. Wang, X. Z. Chen, J. H. Li, Appl. Phys. Lett., Vol. 93, p. 131107 (2008).
14. S. M. Kim, F. Hatami, H. Yuen, A. Chin, P.Kung and J. S. Harris, IEEE (2008).
15. Lim, K. P., Pham, H. T., Yoon, S. F., Tan, K. H., THIN SOLID FILMS, Vol. 520, p. 2269-2271 (2012).
16. Chen, X. Z., Zhang, D. H., Liu, W., Wang, Y., Li, J. H., Electronics Lett., Vol. 46, p. 787 (2010).
17. L. Bhusal, A. Freundlich, Applied surface science, Vol. 255, p. 703-705 (2008).
18. J. T. Wimmers, D. S. Smith, Proc. SPIE, vol. 364, p. 123 (1983).
19. J. T. Wimmers, R. M. Davis, D. S. Smith, Proc. SPIE, vol. 930, p. 125 (1988).
20. P. R. Norton, Opt. Eng. (Bellingham), vol. 30, p. 1649 (1991).
21. M. Razeghi, Opto-Electron. Rev., vol. 6, p. 155 (1998).
22. L. K. Li, Y. Hsu, W. L. Wang, J. Vac. Sci. Technol. B, Vol. 11, p. 872 (1993).
23. S. V. Ivanov, A. A. Boudza, R. N. Kutt, N. N. Ledentsov, S. V. Shaposhnikov, P.S. Kop'ev, J. Cryst. Growth, Vol. 156, p. 191-205 (1995).
24. J. I. Chyi, D. Biswas, S. V. Iyer, N. S. Kumar, and H. Morkoc, Appl. Phys. Lett., Vol. 54, p. 1016 (1989).
25. B. V. Rao, D. Gruznev, T. Tambo, C. Tatsuyama, J. Cryst. Growth, Vol. 224, p. 316-322 (2001).

26. Thomas Mårtensson, C. Patrik T. Svensson, Brent A. Wacaser, Magnus W. Larsson, L. Reine Wallenberg, and Lars Samuelson, Nano Lett., Vol. 4, p. 1987 (2004).
27. Yung S. Liu, "III-V Compound Semiconductor Industry and Technology Development in Taiwan", International Conference on Compound Semiconductor Mfg (2003).
28. Herbert S. Bennett, Julio Costa, and Charles E. Weitzel, "The Compound Semiconductor Technology Roadmap Embedded in the 2003 ITRS: Implications for the MANTECH Community".
29. M. Passlack**,** R. Droopad**,** A. Asenov**,** Solid State Technology, Vol. 51, p. 28-30 (2008).
30. S. Sakr, E. Giraud, A. Dussaigne, M. Tchernycheva, N. Grandjean, F. H. Julien, Appl. Phys. Lett., Vol. 100, p. 181103 (2012).
31. Onaran Efe, Onbasli M. Cengiz, Yesilyurt Alper, Optics Express, Vol. 20 , p. 7608-7615 (2012).
32. Yang Hung-Pin D., Chen I-Liang, Lee Chen-Hong, Japanese Journal of Applied Physics, Part 2-Letters & Express Letters, Vol. 46, p. L509-L511 (2007).
33. Q. Cao, S. F. Yoon, C. Y. Liu, Nanoscale Research letters, Vol. 2, p. 303-307 (2007).
34. Deshmukh MP, Nagaraju J, Solar Energy Materials and Solar cells, Vol. 89, p. 403-408 (2005).
35. H. S. Lee, M. Yamaguchi, N. J. Ekins-Daukes, J. Appl. Phys., Vol. 98, p. 093701 (2005).
36. A. Rogalski, Opt. Eng.(Bellingham) 33, 1392 (1994).

37. Landolt-Bornstein, “Physics of group IV elements and III–V compounds”, Vol. 17a. Springer-Verlag (1982).
38. Litwin-Staszewska, E., W. Szymanska, P. Piotrzkowski, Phys. Status Solidi (b) Vol. 106, p. 551-559 (1981).
39. Sparks, P. W. and C. A. Swenson, Phys. Rev., Vol. 163, p. 779-790 (1967).
40. Adachi, S., J. AppL. Phys. Vol. 66, p. 6030-6040 (1989).
41. Slutsky, L. J. and C. W. Garland, Phys. Rev., Vol. 113, p. 167-169 (1959).
42. EVAN O. KANE, J.Phys. Chem. Solids., Pergamon Press., Vol. 1, pp. 249-261 (1957).
43. S Ben Radhia, N Fraj, I Saidi and K Boujdaria, Semicond. Sci. Technol., Vol. 22, p. 427–434 (2007).
44. Gregorio H. Cocoletzi, Noboru Takeuchi, Phys. Rev. B, Vol. 61, p. 15581 (2001).
45. S. H. Rhim, Miyoung Kim, and A. J. Freeman, Phys. Rev. B, Vol. 71, p. 045202 (2005).
46. Zhen Gang Zhu, Tony Low, and G Samudra, Semicond. Sci. Technol., Vol. 23, p. 025009 (2008).
47. Rezek Mohammad, Musa El-Hasan, J Mater Sci., Vol. 43, p. 2935–2946 (2008).
48. I. Vurgaftman and J. R. Meyer, J. Appl. Phys., Vol. 89, p. 5815 (2001).
49. Jost, S. R, Meikleham, V. F, Myers, T.H, Materials for Infrared Detectors and Sources Symposium, p. 429-435 (1987).
50. Antoni Rogalski, Progress in Quantum Electronics, Vol. 27, p. 59–210 (2003).

51. Tiphene, D., Lacombe, F., Rouan, D., Proceedings of the SPIE - The International Society for Optical Engineering, Vol. 865, p. 122-8 (1988).
52. Chen Boliang, Lu Wei, Wang Hui, Journal of Infrared and Millimeter Waves, Vol. 19, p. 89-92 (2000).
53. Blackwell, J., Botts, S., Arnold, H., Proceedings of the SPIE - The International Society for Optical Engineering, Vol. 1157, p. 243-9 (1989).
54. Heynessens, J., Fowler, A., Proceedings of the SPIE - The International Society for Optical Engineering, Vol. 1946, p. 49-54 (1993).
55. Fowler, A. M., Gatley, I., Hoffman, A., Proceedings of the SPIE - The International Society for Optical Engineering, Vol. 2816, p. 150-60 (1996).
56. Hoffan, A.W., Corrales, E., Merrill, M., McMurtry, C., Proceedings of the SPIE - The International Society for Optical Engineering, Vol. 5499, p. 59-67 (2004).
57. K. Mohammed, F. Capasso, R.A. Logan, A.L. Hutchinson, Electr. lett, Vol. 22, p.215-216 (1986).
58. XiuYing Gong, Masashi Kumagawa, Jpn. J. Appl. Phys., Vol. 36, p. 2614-2616 (1997).
59. Xiaofei Liu , Mingde Zhang, International Journal of Infrared and Millimeter Waves, Vol. 21, p. 1697-701 (2000).
60. W. D. Lawson, S. Nielson, A. S. Young, Journal of Physics and Chemistry of Solids, Vol. 9, p. 325–329 (1959).
61. P.W. Kruse, M.D. Blue, J.H. Garfunkel, W.D. Saur, Infrared Physics, Vol. 2, p. 253–60 (1962).
62. Kruer. M., Esterowitz. L., Bartoli. F., Allen. R., Infrared Physics, Vol. 18, p. 315-25 (1978).

63. Kaneda. T, Sei. H, Ueda. T, Japanese Journal of Applied Physics, Vol. 10, p. 1475-6 (1971).

64. Mainzer. A. K., Hong. J, Stapebroek, M. G., Yong. E, Proceedings of the SPIE - The International Society for Optical Engineering, Vol. 5881, p. 58810Y-1-8 (2005).

65. J. Melngailis, T. C. Harman., Semiconductors and Semimetals, Vol. 5, p. 111-174 (1970).

66. Wang. C. C., Lorenzo. J. S., Infrared Physics, Vol. 17, p. 83-8 (1977).

67. Wu. C.S., Wen. C.P., Sato. R. N., Nayer. P.S., IEEE Transactions on Electron Devices, Vol. 39, p. 234-41(1992).

68. Sheregii E. M., Cebulski J., Marcelli A., Phys. Rev. Lett., Vol. 102, p. 045504 (2009).

69. Murthy Oruganty V. S. N., Venkataraman V., Sharma R. K., J. Appl. Phys., Vol. 106, p. 113708 (2009).

70. Manchanda Rachna, Pal R., Malik A., J. Appl. Phys., Vol. 106, p. 056103 (2009).

71. Y. H. Choi, C. Besikci, FL Sudharsanan, and M. Razeghi, Appl. Phys. Lett., Vol. 63, p. 361 (1993).

72. Mark van Schilfgaarde and Arden Sher, Appl. Phys. Lett., Vol. 62, p. 1857 (1993).

73. Y. H. Choi, P. T. Staveteig, E. Bigan, and M. Razeghi, J. Appl. Phys., Vol. 75, p. 3196 (1994).

74. J. J. lee, J. D. Kim, M. Razeghi, Opto-electronics Review, Vol. 7(1), p. 19-28 (1999).

75. J. J. Lee and M. Razeghi, Appl. Phys. Lett., Vol. 76, p. 297 (2000).

76. A. M. Jean-Louis and C. Hamon, Phys. Status Solid, Vol. 34, p. 329 (1969).

77. A. J. Noreika, W. J. Takei, M. H. Francombe, C. E. C. Wood, J. Appl. Phys., Vol. 53, p. 4932 (1982).

78. J. L. Zilko, J. E. Green, J. Appl. Phys., Vol. 51, p. 1549 (1980).

79. J.L. Zilko, J.E. Greene, J. Appl. Phys., Vol. 51, p. 1560 (1980).

80. V. K. Dixit, B.V. Rodrigues, H. L. Bhat, Journal of Crystal Growth, Vol. 217, p. 40-46 (2000).

81. K. T. Huang, C. T. Chiu, and G. B. Stringfellow, J. Appl. Phys., Vol. 75, p. 2857 (1994).

82. J. D. Kim, S. Kim, J. Piotrowski, E. Bigan, and M. Razeghi, Appl. Phys. Lett., Vol. 67, p. 2645 (1995).

83. J. D. Kim, D. Wu, J. Wojkowski, J. Xu, and M. Razeghi, Appl. Phys. Lett., Vol. 68, p. 99 (1996).

84. Changtao Peng, NuoFu Chen, Chenlong Chen, Yude Yu, Appl. Phys. Lett., Vol. 88, p. 242108 (2006).

85. Fubao Gao, NuoFu Chen, Yu Wang, Jinliang Wu, J. Appl. Phys., Vol. 104, p. 073712 (2008).

86. Rezek Mohammad, Senay Katırcıo˘glu, Journal of Alloys and Compounds, Vol. 469, p. 504-511 (2009).

87. G. A. Sai-Halasz, R. Tsu, and L. Esaki, Appl. Phys. Lett., Vol. 30, p. 651 (1977).

88. D. L. Smith and C. Mailhiot, J. Appl. Phys., Vol. 62, p. 2545 (1987).

89. C. Mailhiot, D.L. Smith, J. Vac. Sci. Technol. A7 (1989) 445.

90. D.H. Chow, R.H. Miles, A.T. Hunter, J. Vac. Sci. Technol. B., Vol. 10, p. 888 (1992).

91. C.H. Grein, P.M. Young, H. Ehrenreich, Appl. Phys. Lett., Vol. 61, p. 2905 (1992).

92. R.H. Miles, J.N. Schulman, D.H. Chow, T.C. McGill, Semicond. Sci. Technol., Vol. 8, p. S102 (1993).

93. J. Katz, Y. Zhang, W.I. Wang, Appl. Phys. Lett., Vol. 62, p. 609 (1993).

94. Manijeh Razegh, Binh-Minh Nguyen , Physics Procedia, Vol. 3, p. 1207 (2010).

95. Yanhua Zhang, Wenquan Ma, and Xiaolu Guo, Appl. Phys. Lett., Vol. 100, p. 173511 (2012).

96. H. S. Kim, O. O. Cellek, Xin-Hao Zhao, and Y.-H. Zhang, Appl. Phys. Lett., Vol. 101, p. 161114 (2012).

97. W. Shan, W. Walukiewicz, J. M. Olson, and S. R. Kurtz, Phys. Rev. Lett., Vol. 82, p. 1221 (1999).

98. J. Wu, W.Shan, and W. Walukiewicz, Semicond. Sci. Technol., Vol. 17, p. 860 (2002).

99. J. N. Baillargeon, K. Y. Cheng, and K. C. Hsieh, Appl. Phys. Lett., Vol. 60, p. 2540 (1992).

100. X. Liu, S. G. Bishop, J. N. Baillargeon, and K. Y. Cheng, Appl. Phys. Lett., Vol. 63, p. 208 (1993).

101. M. Weyers, M. Sato, and H. Ando, Jpn. J. Appl. Phys., Part .2 Vol. 31, p. L853 (1992).

102. M. Weyers and M. Sato, Appl. Phys. Lett., Vol. 62, p. 1396 (1993).

103. N. Tit and M. W. C. Dharma-wardana, Appl. Phys. Lett., Vol. 76, p. 3576 (2000).

104. T. D. Veal, L. F. J. Piper, and C. F. McConville, Appl. Phys. Lett., Vol. 87, p. 182114 (2005).

105. Mondal. A., Das. T. D., Kumar. J., Journal of Crystal Growth, Vol. 297, p. 4-6 (2006).

106. Belabbes. A., Ferhat. M., Zaoui. A., Appl. Phys. Lett., Vol. 88, p. 152109 (2006).

107. B. N. Murdin, M. Kamal-Saadi, and A. R. Adams, Appl. Phys. Lett., Vol. 78, p. 1568 (2001).

108. W. Shan, W. Walukiewicz, J. M. Olson, and S. R. Kurtz, Phys. Rev. Lett., Vol. 82, p. 1221 (1999).

109. A. Lindsay and E. P. O'Reilly, Solid State Commun., Vol. 112, p. 443 (1999).

110. I. Vurgaftman, R. Meyer and L. R. Ram-Mohan, J. Appl. Phys., Vol., Vol. 89, p. 5815 (2001).

111. Y. Li, F. Qian, J. Xiang, C.M. Lieber, Mater. Today, Vol. 9, p. 18 (2006).

112. C. Weisbuch, B. Vinter, Quantum Semiconductor Structures: Fundamentals and Applications, Academic Press, Boston (1991).

113. Burchhart T., Lugstein A., Hyun Y. J., Nano Lett., Vol. 9, p. 3739-3742 (2009).

114. Chang H. -Y., Tsybeskov L., Sharma S., Appl. Phys. Lett., Vol. 95, p. 133120 (2009).

115. Wei Yaguang, Wu Wenzhuo, Guo Rui, Nano Lett., Vol. 10, p. 3414-3419 (2010).

116. Yuan G. D., Zhang W. J.; Jie J. S., Lee, S. T., Nano Lett, Vol. 8, p. 2591-2597 (2008).

117. Liang Yao, Liang Hui, Xiao Xudong, Journal of Materials Chemistry, Vol. 22, p. 1199-1205 (2012).

118. Min Wang, Guang Tao Fei, Yu Gang Zhang, Ming Guang Kong, and Li De Zhang, Adv. Mater., Vol. 19, p. 4491-4494 (2007).

119. Cheng Chung-Liang, Chen Yang-Fang, Materials Chemistry and Physics, Vol. 115, p. 158-160 (2009).

120. Fan Xia, Meng Xiang Min, Zhang Xiao Hong, J. Phys. Chem. C., Vol. 113, p. 834-838 (2009).

121. L. Samuelson, Mater. Today, Vol. 6, p. 22 (2003).

122. Lugstein A., Steinmair M., Hyun Y. J., Appl. Phys. Lett., Vol. 90, p. 023109 (2009).

123. Tchernycheva M., Harmand J. C., Patriarche G., Nanotechnology, Vol. 17, p. 4025-4030 (2006).

124. Zhang Chenxi, Chen Ping, Liu Jian, Chemical Communication, Vol. 28, p. 3290-3292 (2008).

125. Li Qiming, Wang George T, Appl. Phys. Lett. Vol. 93, p. 043119 (2008).

126. Tian Xi-ke, Zhao Xiao-yu; Zhang Li-de, Nanotechnology, Vol. 19, p. 215711 (2008).

127. Wagner. R. S., Ellis. W. C., Appl. Phys. Lett., Vol. 4, p. 89 (1964).

128. K. W. Chang, J. J. Wu, J. Phys. Chem. B., Vol. 106, p. 7796-7799 (2002).

129. Heun Stefan, Radha Boya, Ercolani Daniele, Small, Vol. 6, p. 1935-1941 (2010).

130. Zhang Zhang, Shimizu Tomohiro, Chen Lijun, Advanced Materials, Vol. 21, p. 4710 (2009).

131. Mousavi S. H., Haratizadeh H., Minaee H., Thin Solid Film, Vol. 520, p. 4642-4645 (2012).

132. Jin-Shyong Lin, Chien-Chon Chenb, Eric Wei-Guang Diau, Tzeng-Feng Liu, Journal of materials processing technology, Vol. 206, p. 425-430 (2008).

133. Wang X., Liu W., Yang H., Acta Materialia, Vol. 59, p. 1291-1299 (2011).

134. Yan Youguo, Zhang Ye, Zeng Haibo, Zhang Lide, Nanotechnology, Vol. 18, p. 175601 (2007).

135. Liu Chun, Hu Zheng, Wu Qiang, Journal of Nanoelectronics and Optoelectronics, Vol. 1, p. 114-118 (2006).

136. Gai Ligang, Jiang Haihui, Ma Wanyong, J. Phys. Chem. C., Vol. 111, p. 2386-2390 (2007).

137. Wang Fudong, Dong Angang, Sun Jianwei, Vol. 45, Inorganic Chemistry, p. 7511-7521 (2006).

138. T. J. Trentler, K. M. Hickman, S. C. Goel, A.M. Viano, P.C. Gibbons, W.E. Buhro, Science, Vol. 270, p. 1791 (1995).

139. K. A. Dick, K. Deppert, L. Samuelson, W. Seifert, J. Cryst. Growth, Vol. 297, p. 326 (2006).

140. L. E. Fröberg, W. Seifert, J. Johansson, Phys. Rev. B., Vol. 76, p. 153401 (2007).

141. V. G. Dubrovskii, N. V. Sibirev, G. E. Cirlin, V. M. Ustinov, J. C. Harmand, Semiconductors, Vol. 41, p. 1240 (2007).

142. Mojica D. Camacho, Niquet Yann-Michel, Phys. Rev. B., Vol. 81, P. 195313 (2010).

143. Hou Wen Chi, Hong Franklin Chau-Nan, Nanotechnology, Vol. 20, p. 055606 (2009).

144. Joyce Hannah J.; Gao Qiang; Tan H. Hoe, Nano lett., Vol. 7, p. 921-926 (2007).

145. Ikejiri Keitaro, Noborisaka Jinichiro, Hara Shinjiroh, J. Cryst. Growth, Vol. 298, p. 616-619 (2007).

146. Suyatin Dmitry B, Sun Jie, Fuhrer Andreas, Nano Lett., Vol. 8, p. 1100-1104 (2008).

147. Sorensen B. S., Aagesen M., Sorensen C. B., Appl. Phys. Lett., Vol. 92, p. 012119 (2008).

148. Hillerich Karla, Dick Kimberly A, Messing Maria E, Nano Research, Vol. 5, p. 297-306 (2012).

149. Tchernycheva Maria, Cirlin George E, Patriarche Gilles, Nano Lett., Vol. 7, p. 1500-1504 (2007).

150. Xiao M. X, Zhao M, Jiang Q, Journal of Applied Physics, Vol. 110, p. 054308 (2011).

151. Chang Yi-Lu, Mi Zetian, Li Feng, Advanced Functional Materials, Vol. 20, p. 4146-4154 (2010).

152. Hyun D. Park, S.M. Prokes, M.E. Twigg, Yong Ding, Zhong Lin Wang, J. Cryst. Growth.,Vol. 304, p. 399-401 (2007).

153. Rajat Kanti Paul, Miroslav Penchev, Jiebin Zhong, Mihrimah Ozkan, Cengiz S. Ozkan, Materials Chemistry and Physics, Vol. 121, p. 397-401 (2010).

154. Xunyu Yang, Gongming Wang, Peter Slattery, Jin Z. Zhang, and Yat Li, Crystal Growth & Design, Vol. 10, p. 2479 (2010).

155. Alexander T Vogel, Johannes de Boor, Michael Becker, Joerg V Wittemann, Samuel L Mensah, PeterWerner and Volker Schmidt, Nanotechnology, Vol. 22, p. 015605 (2011).

156. L. Lugani, D Ercolani, L. Sorba, N. V. Sibirev, M. A. Timofeeva and V. G. Dubrovskii, Nanotechnology, Vol. 23, p. 095602 (2012).

157. Xueru Zhang, Yufeng Hao, Guowen Meng, and Lide Zhang, Journal of The Electrochemical Society, Vol. 152, p. C664, (2005).

158. M. Ibrahim Khan, XuWang, Krassimir N. Bozhilov, and Cengiz S. Ozkan, Journal of Nanomaterials, Vol. 2008, Article ID. 698759 (2008).

159. Philippe Caroff, Maria E Messing, B Mattias Borg, Kimberly A Dick, Knut Deppert and Lars-ErikWernersson, Nanotechnology, Vol. 20, p. 495606 (2009).

160. Philippe Caroff, Jakob B. Wagner, Kimberly A. Dick, Henrik A. Nilsson, Mattias Jeppsson, Knut Deppert, Lars Samuelson, L. Reine Wallenberg, and Lars-Erik Wernersson, Small, Vol. 4, p. 878-882 (2008).

161. B. M. Borg, M. E. Messing, P. Caroff, K. A. Dick, K. Deppert and L-E. Wernersson, IEEE, p. 245 (2009).

162. Hongzhi Chen, Xuhui Sun, King W. C. Lai, M. Meyyappan, and Ning Xi, IEEE Nanotechnology Materials and Devices Conference, p. 212-216 (2009).

163. O. N. Uryupin, M. V. Vedernikov, A. A. Shabaldin, Y. V. Ivanov, Y. A. Kumzerov, and A. V. Forkin, Journal of Electronic Material, Vol. 38, p. 990 (2009).
164. S. V. Zaitsev-Zotov, Y. A. Kumzerov, Y. A. Firsov and P. Monceau, J. Phys.: Condens. Matter., Vol. 12, p. L303-L309 (2000).
165. Björk. M. T., Fuhrer. A., Hansen. A. E., Larsson. M. W., Fröberg. L. E., Samuelson. L., Phys. Rev. B., Vol. 72, p. 201307 (2005).
166. Roddaro. S., Fuhrer. A., Brusheim. P., Fasth. C., Xu. H. Q., Samuelson. L., Xiang. J., Lieber. C. M., Phys. Rev. Lett., Vol. 101, p. 186802 (2008).
167. Davidovic. D., Tinkham. M., Phys. Rev. Lett., Vol. 83, p. 1644 (1999).
168. Henrik A. Nilsson, Philippe Caroff, Claes Thelander, Marcus Larsson, Lars Samuelson, and H. Q. Xu, Nano Lett*.,* Vol. 9, p. 3151 (2009).
169. S. D. Ganichev, V. V. Bel'kov, L. E. Golub, E. L. Ivchenko, Petra Schneider, S. Giglberger, J. Eroms, J. De Boeck, G. Borghs, W. Wegscheider, D. Weiss, and W. Prettl, Phys. Rev. Lett., Vol. 92, p. 256601 (2004).
170. X. W. Zhang and J. B. Xia, Phys. Rev. B., Vol. 74, p. 075304 (2006).
171. T. ishiguro, y. Kobori, Y. Nagawa, Y. Yamaguchi, Materials Research Society, Vol. 799, p. 45 (2003).
172. G. B. Stringfellow, Organometaliic Vapor-Phase Epitaxy: Teory and Practice, Academic Press, San Siego, CA (1999).
173. R. M. Biefeld, J. Crystal Growth, Vol. 77, p. 392 (1986).
174. K. F. Longenbach and W. I. Wang, Appl. Phys. Lett., Vol. 59, p. 2427 (1991).

175. Brian R. Bennett, R. Magno, and B. V. Shanabrook, Appl. Phys. Lett., Vol. 68, p. 505 (1996).

176. A Krier, X L Huang and A. Hammiche, J. Phys. D: Appl. Phys., Vol. 34, p. 874-878 (2001).

177. A. Aardvark, N. J. Mason, P. J. Walker, Prog. Crystal Growth Character. Mater., Vol. 35, p. 207 (1997).

178. R. M. Biefeld and G. A. Hebner, Appl. Phys. Lett., Vol. 57, p. 1563 (1990).

179. D. K. Gaskill, G. T. Stauf, N. Botka, Appl. Phys. Lett., Vol. 58, p. 1905 (1991).

180. Y. P. Varshini, Physica, Vol. 34, p. 149-154 (1967).

181. C. Benoitä la Guillaume, P. Lavallard, in: Proceedings of the International Conference on the Physics of Semiconductors, p. 875 （1962）.

182. J. C. Pehek, H. Levinstein, Phys. Rev. Vol. 140, p. A576 (1965).

183. R. N. Hall, J. H. Racette, J. Appl. Phys., Vol. 32, p. 2078 (1961).

184. N. L. Rowell, Infrared Phys., Vol. 28, p. 37-42 (1988).

185. Aram Mooradian, H.Y. Fan, Phys. Rev., Vol. 148, p. 148 (1966).

186. V. I. Ivanov-Omskii, I. A. Petroff, V. A. Smirnov, R. A. Stranding, Semicond. Sci. Technol., Vol. 8, p. 276 (1993).

187. Rui Chen, S. Phann, A.M.R. Godenir, A. Krier, Appl. Phys. Lett., Vol. 95, p. 261905 (2009).

188. K. D. Chauduri, Anita Luthra, S.k. Agarwal, and P.C. Mathur, Phys. Rev. B., Vol. 22, p. 6319 (1980).

189. D. L. Dexter and F. Seitz, Phys. Rev., Vol. 96, p. 964 (1952).

190. A. Höglund, C. W. M. Castleton, B. Johansson, and S. Mirbt, Phys. Rev. B., Vol. 74, P. 075332 (2006).

191. J.-D. Hecht, F. Frost, D. Hirsch and A. Schindler, J. Appl. Phys., Vol. 90, p. 6066 (2001).

192. N. Chen, Y. Wang, H. He, and L. Lin, Phys. Rev. B., Vol. 54, p. 8516 (1996).

193. R. M. Biefeld and G. A. Hebner, Appl. Phys. Lett., Vol. 57, p. 1563 (1990).

194. J. L. Davis and P. E. Thompson, Appl. Phys. Lett., Vol. 54, p. 2235-2237 (1989).

195. J. E. Oh, P.K. Bhattacharya, Y. C. Chen and S. Tsukamoto, J. Appl. Phys., Vol. 66, p. 3618 (1989).

196. J. B. Webb and C. Halpin, Appl. Phys. Lett., Vol. 47, p. 831 (1985).

197. S.V. Ivanov, A.A. Boudza, R.N. Kutt, N.N. Ledentsov, B.Ya. Meltser, P.S. Kop'ev, J. Crystal Growth, Vol. 156, p. 191-205 (1995).

198. L. K. Li, Y. Hsu, and W. I. Wang, J. Vac. Sci. Technol. B, Vol. 11, p. 872 (1993).

199. T. R. Yang, Y. Cheng, Z. C. Feng, Thin Solid Films, Vol. 498, p. 158-162 (2006).

200. P. E. Thompson, J. L. Davis, D. K. Gaskill, and R. Stahlbush, J. Appl. Phys., Vol. 69, p. 7166 (1991).

201. P. H. Jefferson, T. D. Veal, and C. F. McConville, phys. stat. sol., Vol. 1 p. 104-106 (2007).

202. Nimai C. Patra,Sudhakar Bharatan,and Shanthi Iyer, J. Appl. Phys., Vol. 111, p. 083104 (2012).

203. Nimai C. Patra,Sudhakar Bharatan,and Shanthi Iyer, J. Appl. Phys., Vol. 112, p. 083107 (2012).
204. Youwen Yang, Liang Li, Xiaohu Huang, Guanghai Li, Lide Zhang, J. Mater. Sci., Vol. 42, p. 2753-2757 (2007).
205. Hyun D. Park, S .M . Prokes, M.E. Twigg, Yong Ding, Zhong Lin Wang, J. Cryst. Growth, Vol 304, p. 399-401 (2007).
206. A. T. Vogel, J. V. Wittemann, E. Pippel, and V. Schmidt, Selected Results, p. 36-37 (2012).
207. Feng Zhou, Arden L Moore, Michael T Pettes, Lew Rabenberg and Li Shi, J. Phys. D: Appl. Phys., Vol. 43m p. 025406 (2010).
208. Chandrashekhar Pendyala, Sreeram Vaddiraju, Jeong H Kim, Zhiqiang Chen and Mahendra K Sunkara, Semicond. Sci. Technol., Vol. 25, p. 024014 (2010).
209. Alexander T. Vogel, Johannes de Boorand, Volker Schmidt, Crystal Growth & Design, Vol. 11, p. 1896 (2011).
210. Cheng-Hsiang Kuo, Jyh-Ming Wu and Su-Jien Lin, Nanoscale Research letter, Vol. 8, p. 69 (2013).
211. Seth A. Fortuna, Jianguo Wen, Ik Su Chun, and Xiuling L, Nano Lett., Vol. 12, p. 4421-7 (2008).
212. Anders Mikkelsen, Niklas Sk¨old, Lassana Ouattara and Edvin Lundgren, Nanotechnology, Vol. 17, p. S362–S368 (2006).
213. X. Jing, M. Penchev, J Zhong, R. Paul, M. Ozkan, and C. Ozkan, Proc. of SPIE, Vol. 7402, p. 74020I-1 (2009).
214. Rajat Kanti Paul, Sushmee Badhulika, and Ashok Mulchandani, Appl. Phys. Lett., Vol. 99, p. 033103 (2011).

215. Yennai Wang, Junhong Chi, Karan Banerjee, Detlev Grützmacher, Thomas Schäpers and Jia G. Lu, J. Mater. Chem., Vol. 21, p. 2459 (2011).

216. Wagner R. S. and Ellis W. C., Appl. Phys. Lett., Vol. p. 89–90 (1964).

217. C. Thomas Tsai and R. Stanley Williams, J. Mater. Res., Vol. 1, p. 352 (1986).

218. H. S. Liu, C. L. Liu, C.WANG, Z. P. Jin, and K. Ishida, J. Elec. Mater., Vol. 32, p. 81 (2003).

219. Tatsumi, Y., Hirata, M., Shigi, M., Japan. J. Appl. Phys., Vol. 18, p. 2199 (1979).

220. Vaddiraju S, Sunkara M K, Chin A H, Ning C Z, Dholakia G R, and Meyyappan M, *J. Phys. Chem.* C., Vol. 111, p. 7339 (2007).

221. M. Borgström, K. Deppert, L. Samuelson, W. Seifert, J. Cryst. Growth, Vol. 260, p. 18 (2004).

222. Sharma S, Li H, Chandrasekaran H, Mani R C and Sunkara M K, Encyclopedia Nanosci. Nanotechnol., Vol. 10, p. 327 (2004).

223. Shadi A. Dayeh, Edward T. Yu, and Deli Wang, Nano Lett., Vol. 7, p. 2486-2487 (2007).

224. Dick, K. A., Deppert, K., Martensson, T., Mandl, B., Samuelson, L., Seifert, W., Nano Lett., Vol.5, p. 761 (2005).

225. E. Ertekin, P. A. Greaney, D. C. Chrzan, and T. D. Sands, J. Appl. Phys., Vol. 97, p. 114325 (2005).

226. W. K. Liu, J. Winesett, Weiluan Ma, Xuemei Zhang, and M. B. Santos, J. Appl. Phys., Vol. 81, p. 1708 (1997).

227. Nakayama Koji, Nakatani Kimihiko, Khamseh Sara, Japan. J. Appl. Phys., Vol. 50, p. 01BF01 (2011).

228. Li Dengyue, Li Hongtao, Sun Hehui, Nanoscale Research Letters, Vol. 6, p. 1-4 (2011).

229. E. I. Givargizov, J. Cryst. Growth, Vol. 31, p. 20-30 (1975).

230. Jiansheng Jie, Guanzhong Wang, Xinhai Han, Jieping Fang, Qingxuan Yu, Yuan Liao, Bo Xu, Qingtao Wang, and J. G. Hou, J. Phys. Chem. B., Vol. 108, p. 8249-8253 (2004).

231. Sam Crawford, Sung Keun Lim, and Silvija Gradečak, Nano Lett., (2012).

232. K. Mondal, Ajay Kumar, G. Gupta, B.S. Murty, Acta Materialia, Vol. 57, p. 3422–3430 (2009).